

**A MULTI-SENSOR INTELLIGENT  
ASSISTANCE SYSTEM FOR DRIVER STATUS  
MONITORING AND INTENTION PREDICTION**

**Ein multisensorisches intelligentes Assistenzsystem  
für die Überwachung des Fahrerzustands und die  
Vorhersage der Fahrerhandlungsabsicht**

vom

Fachbereich Elektrotechnik und Informationstechnik  
der Technischen Universität Kaiserslautern  
zur Verleihung des akademischen Grades

**Doktor der Ingenieurwissenschaften (Dr.-Ing.)**

genehmigte Dissertation

von

Li Li

geb. in Hubei, China

D386

Eingereicht am: 06.06.2016  
Tag der mündlichen Prüfung am: 28.09.2016  
Dekan des Fachbereichs: Prof. Dr.-Ing. Hans D. Schotten

Promotionskommission

Vorsitzender: Jun.-Prof. Dr.-Ing. Daniel Görges  
1. Berichterstatter: Prof. Dr.-Ing. Andreas König  
2. Berichterstatter: Prof. Dr.-Ing. Mario Köppen

---

©Copyright by Li Li, 2016  
All Rights Reserved

## Abstract

Advanced sensing systems, sophisticated algorithms, and increasing computational resources continuously enhance the advanced driver assistance systems (ADAS). To date, despite that some vehicle based approaches to driver fatigue/drowsiness detection have been realized and deployed, objectively and reliably detecting the fatigue/drowsiness state of driver without compromising driving experience still remains challenging. In general, the choice of input sensorial information is limited in the state-of-the-art work. On the other hand, smart and safe driving, as representative future trends in the automotive industry worldwide, increasingly demands the new dimensional human-vehicle interactions, as well as the associated behavioral and bioinformatical data perception of driver. Thus, the goal of this research work is to investigate the employment of general and custom 3D-CMOS sensing concepts for the driver status monitoring, and to explore the improvement by merging/fusing this information with other salient customized information sources for gaining robustness/reliability. This thesis presents an effective multi-sensor approach with novel features to driver status monitoring and intention prediction aimed at drowsiness detection based on a multi-sensor intelligent assistance system – DeCaDrive, which is implemented on an integrated soft-computing system with multi-sensing interfaces in a simulated driving environment. Utilizing active illumination, the IR depth camera of the realized system can provide rich facial and body features in 3D in a non-intrusive manner. In addition, steering angle sensor, pulse rate sensor, and embedded impedance spectroscopy sensor are incorporated to aid in the detection/prediction of driver's state and intention. A holistic design methodology for ADAS encompassing both driver- and vehicle-based approaches to driver assistance is discussed in the thesis as well. Multi-sensor data fusion and hierarchical SVM techniques are used in

DeCaDrive to facilitate the classification of driver drowsiness levels based on which a warning can be issued in order to prevent possible traffic accidents. The realized DeCaDrive system achieves up to 99.66% classification accuracy on the defined drowsiness levels, and exhibits promising features such as head/eye tracking, blink detection, gaze estimation that can be utilized in human-vehicle interactions. However, the driver's state of "microsleep" can hardly be reflected in the sensor features of the implemented system. General improvements on the sensitivity of sensory components and on the system computation power are required to address this issue. Possible new features and development considerations for DeCaDrive are discussed as well in the thesis aiming to gain market acceptance in the future.



## Kurzfassung

Fahrsicherheit ist eine der essentiellsten Anforderungen an Systeme zur menschlichen Mobilität. Die Erreichung aktiver Sicherheit durch Fahrerassistenzsysteme hat den Weg zu den heutigen 'Mainstream' Automobilanwendungen bereitet.

Obwohl einige fahrzeuggestützte Lösungen zur Fahrermüdigkeitserkennung realisiert und kommerziell eingesetzt worden sind, bleibt bis zum heutigem Stand eine objektive und zuverlässige Müdigkeitserkennung des Fahrers ohne Kompromisse hinsichtlich des Fahrerlebnisses nach wie vor eine Herausforderung. Im Stand der Technik wird im Allgemeinen die Wahl der sensorischen Eingangsdaten solcher Systeme beschränkt. Andererseits verlangt 'smarter' und sicheres Fahren, als Vertreter des Zukunftstrends in der weltweiten Automobilindustrie, zunehmend die neue dimensionale Mensch-Fahrzeug-Interaktion, sowie die damit verbundene Verhaltens- und bioinformatische Datenerfassung des Fahrers. Daher ist das Ziel dieser Forschungsarbeit die Anwendung von generischen und kundenspezifischen 3D-CMOS-Sensorkonzepten für die Fahrerzustandsüberwachung zu untersuchen und mögliche Verbesserung zu explorieren, insbesondere durch die Fusion dieser Informationen mit anderen geeigneten maßgeschneiderten Informationsquellen zur Erhöhung der Robustheit und Zuverlässigkeit der Erkennung.

In der vorliegenden Arbeit wird DeCaDrive, eine effektive multisensorische Systemlösung mit neuartigen Eigenschaften für die Müdigkeitserkennung des Fahrers auf Basis von spezieller IR-basierter Tiefenmessung und eingebetteter Impedanzspektroskopie, sowie Multisensordatenfusion und Soft-Computing Algorithmen, vorgestellt. Vielversprechende Validierungsergebnisse von bis zu 99,66% Klassifikationsgenauigkeit konnten für die Müdigkeitserkennung mit eigens akquirierten on-line Daten im Demonstrator erreicht

werden. Allerdings spiegelt sich der Fahrerzustand 'Sekundenschlaf' bislang unzureichend in den Sensormerkmalen und der Entscheidungsfähigkeit des implementierten Systems wider. Allgemeine Verbesserungen der Empfindlichkeit der sensorischen Komponenten und der System-Rechenleistung werden benötigt, um dieses Problem zu beheben.

Eine der offenen Fragen in der DeCaDrive Systemmodellierung ist die Definition des sogenannten 'Ground-Truth' für die tatsächlichen Wachheit oder Schläfrigkeit der Probanden, die in dieser Arbeit noch heuristisch ermittelt wurde. In Zukunft können EEG-basierten Methoden, die in der Schlaf-forschung weit verbreitet verwendet werden, mit entsprechendem Aufwand angepasst und genutzt werden, um eine bessere, objektive Bestimmung des tatsächlichen Zustands ('Ground-Truth') zu gewinnen. Ein weiteres Problem ist eine potenzielle Personabhängigkeit in dem Klassifizierungssystem aufgrund der begrenzten Anzahl und Phänotypen der Probanden, die durch die Erweiterung Probandenzahl und der Datenbank dieser Arbeit folgend in den nächsten Schritten überwunden werden kann. Die Robustheit von DeCaDrive müsste vom jetzigen Forschungsprototyp ausgehend mit umfangreicheren statistischen Analysen und mit Daten aus realen Fahrscenarien untersucht und in Richtung eines Produkts verbessert werden.

Ein wesentlicher Beitrag der Arbeit ist die detaillierte Untersuchung und Nutzung von 3D-Embedded-Vision Technologien, insbesondere Tiefenkameras, im Bereich der Mensch-Fahrzeug-Interaktionen. Basierend auf neuartigen IR-Tiefenmesssystemen und anderen vielversprechenden Sensortechniken, sowie Sensordatenfusion wurde ein multisensorisches intelligentes Assistenzsystem für Fahrer- Zustandsüberwachung und Absichtserkennung entworfen, als Prototyp implementiert und auf erste Datensätze angewendet. Die Fusion heterogener sensorischen Quellen mit dem Ziel der robusten Müdigkeitserkennung wurde dabei untersucht und umgesetzt. Leistungsstarke Methoden der Computational Intelligence, d.h., hierarchische SVMs für die Entscheidungsfindung und Funktionalität des automatischen Systementwurfs intelligenter Systeme wurden für eine optimale Parametersuche sowie Sensor-Funktion Bestimmung eingesetzt. Weiterhin wurde das

System auf eine neue Open-Access Multi-Plattform Umgebung gebracht, die u.a. eine Cross-Plattform-Funktionalität ermöglichen soll.

Das vorgeschlagene Systemkonzept und -architektur ist nicht nur für Pkw, sondern insbesondere für Nutzfahrzeuge, sowie die Überwachung der Führer von schweren, gefährlichen und/oder teureren Anlagen in Landwirtschaft, Industrie, der Luft- und Raumfahrt usw. von Nutzen.

Trotz des Trends der Automobilelektronik und der immer noch langsamen Fortschritte in Richtung vollständig autonomes Fahren gehören Systeme wie DeCaDrive zu den grundlegenden Komponenten der Mensch-Fahrzeug-Interaktionen in der aktiven Sicherheit und werden noch auf längere Sicht einen Beitrag zur Mensch zentrierten sicheren Mobilität leisten.

Ergänzend zur Müdigkeitserkennung kann die Erfassungsfähigkeit von DeCaDrive durch den modularen Ansatz in Richtung umfassender Fahrerzustandserkennung in komplexen Fahrscenarien erweitert werden. Die Korrelationsstudie der bioelektrischen Impedanz und des menschlichen emotionalen Zustand kann folgend durchgeführt werden. Eine neue Generation von Mensch-Fahrzeug-Schnittstellen kann auf DeCaDrive aufgebaut werden, beispielsweise mit neuen Freiheitsgraden zur 3D-bildbasierten Gestensteuerung, Bioinformatik-basierten Interaktionen usw.

Mit steigender Nachfrage bzgl. Automotive Safety Integrity Level (ASIL) von E/E-Systeme in der Automobilindustrie, und durch eine Fallstudie des Airbag-Systems inspiriert, kann das präsentierte DeCaDrive System erweitert werden, um den Fahrer-/die Insassensicherheit in Bezug auf die Fahrzeuginnenraumüberwachung erhöhen. In der Umgebung von Airbags- und Sicherheitssteuergeräte, ist die Kenntnis der Position des Insassenkopfes zum Zeitpunkt des Aufpralls von besonderem Interesse, sowie die Verfolgung der Orientierung und Position der Extremitäten und des Torso der Insassen. Basierend auf diesen Informationen können intelligentere Entscheidungen getroffen werden, die Auswirkungen oder die Schwere der Verletzungen der Insassen zu minimieren. Eine auf DeCaDrive basierende Plattform mit Fahrer- bzw. Insassenzustandsüberwachung könnte künftig

somit dem Fahrzeugsicherheitssystem ermöglichen, komplexere Algorithmen auszuführen, intelligentere Entscheidungen zu treffen, und die Sicherheitsmaßnahmen in einer effektiveren Art und Weise durchzuführen.

## Acknowledgements

First of all I would like to express my sincere gratitude to my supervisor Prof. Dr.-Ing. Andreas König for suggestion of the topic and his guidance, encouragement, useful hints and discussions throughout the work.

I want to sincerely thank my colleague Kittikhun Thongpull for his support and contribution to the demonstrator on IAA Nutzfahrzeuge 2014 with on-line drowsiness detection to further validate the outcome of my research. I would like to thank my colleagues Benjamin Lutgen, Abhaya Chandra Kammara and Robert Freier for their kind support with test environment, test subjects, etc. in the research work.

I would like to express deep gratitude to my supervised students Yanhao Xu, Klaudius Werber and Thomas Bölke for their support and contributions to my research with respect to depth camera investigation, eye region detection and evaluation, as well as embedded skin impedance measurement aimed at driver drowsiness detection.

It is gratefully acknowledged that the joint work on development and application of DriMix Micro-3D-Camera has been supported by iC-Haus GmbH.

Finally, I would like to sincerely and gratefully thank my family, especially my wife, Qian Gao, for all the support she gave to me down this road in pursuit of happiness.

## **Declaration**

I herewith declare that I have produced this thesis without the prohibited assistance of third parties and without making use of aids other than those specified; notions taken over directly or indirectly from other sources have been identified as such.

This thesis has not previously been presented in identical or similar form to any other German or foreign examination board.

The thesis work was conducted under the supervision of Prof. Dr.-Ing. Andreas König at Institute of Integrated Sensor System, Department of Electrical and Computer Engineering, TU Kaiserslautern.

Li Li, Düsseldorf, 04.06.2016

# Contents

<b>1</b>	<b>Introduction</b>	<b>1</b>
1.1	Motivation . . . . .	1
1.2	The Goal of the Thesis . . . . .	4
1.3	Thesis Structure . . . . .	5
<b>2</b>	<b>Advanced Driver Assistance System</b>	<b>7</b>
2.1	State-of-the-Art ADAS . . . . .	7
2.2	ADAS in Joint Cognitive System . . . . .	9
2.2.1	Hierarchical Control Model . . . . .	9
2.2.2	Driver Status Monitoring and Intention Prediction . . . . .	12
2.3	Discussion: Future Trend . . . . .	14
<b>3</b>	<b>Advanced Embedded Vision Systems for ADAS</b>	<b>17</b>
3.1	Technology Review for 3D Embedded Vision . . . . .	17
3.1.1	Passive Triangulation: Stereo Vision . . . . .	18
3.1.2	Active Triangulation . . . . .	22
3.1.2.1	Lightsheet . . . . .	22
3.1.2.2	Structured Light . . . . .	23
3.1.3	Light-Field Imaging . . . . .	24
3.1.4	Time-of-Flight . . . . .	25
3.1.4.1	3D Laser Scan and LIDAR . . . . .	26
3.1.4.2	ToF Depth Camera . . . . .	28
3.2	Investigated Depth Cameras in the Project . . . . .	31
3.2.1	DriMix Micro-3D-Camera . . . . .	31
3.2.1.1	DriMix Sensor Specification . . . . .	35

## CONTENTS

---

3.2.1.2	DriMix Camera System Evaluation . . . . .	46
3.2.2	Microsoft Kinect: Commodity IR Depth Camera . . . . .	53
3.3	Algorithms and Methods for 3D Embedded Vision . . . . .	56
3.3.1	Single-/Multi-Person Eye Localization . . . . .	56
3.3.2	Kinect based Object Tracking . . . . .	60
3.4	Summary and Discussion . . . . .	62
<b>4</b>	<b>Further Sensory Building Blocks for ADAS</b>	<b>67</b>
4.1	Vehicle Dynamics Measurement . . . . .	67
4.1.1	Measurement and Sensory Principles . . . . .	67
4.1.2	Data Analysis for Vehicle Sensors . . . . .	70
4.2	Body Measurement: Impedance Spectroscopy . . . . .	73
4.2.1	Measurement and Sensory Principles . . . . .	73
4.2.2	Data Analysis for Skin Impedance Measurement . . . . .	74
4.3	Electroencephalography . . . . .	78
4.3.1	Measurement and Sensory Principle . . . . .	78
4.3.2	EEG Data Analysis . . . . .	81
4.4	Heart/Pulse Rate Measurement: ECG and PPG . . . . .	83
4.4.1	Measurement and Sensory Principle . . . . .	83
4.4.2	ECG/PPG Data Analysis . . . . .	84
4.5	Electronic Nose . . . . .	85
4.5.1	Measurement and Sensory Principle . . . . .	85
4.5.2	Data Analysis for Electronic Noses . . . . .	86
4.6	Summary and Discussion . . . . .	86
<b>5</b>	<b>ADAS System Modeling Concept</b>	<b>89</b>
5.1	System Concept and Design Methodology . . . . .	89
5.2	Sensor Fusion Algorithms . . . . .	95
5.3	Multiclass Classification Methods . . . . .	97
5.3.1	Artificial Neural Networks (ANNs) . . . . .	97
5.3.2	Support Vector Machines (SVMs) . . . . .	98
5.4	Summary and Discussion . . . . .	100



---

<b>6 DeCaDrive: System Architecture and Implementation</b>	<b>101</b>
6.1 DeCaDrive System Architecture . . . . .	101
6.2 DeCaDrive Development History . . . . .	103
6.3 Hardware Components . . . . .	106
6.3.1 Analog and Digital Front-End . . . . .	109
6.3.2 Scalable Adaptive Multi-Sensor Interface . . . . .	111
6.4 Software Components . . . . .	112
6.4.1 Sensor Feature Computation . . . . .	113
6.4.2 Learning and Classification . . . . .	117
6.5 Summary and Discussion . . . . .	120
<b>7 Experimental Work</b>	<b>123</b>
7.1 Design of Experiments . . . . .	123
7.2 Simulated Driving Environment . . . . .	124
7.3 Ground Truth Definition . . . . .	126
7.4 Data Evaluation and System Validation . . . . .	129
7.5 Summary and Discussion . . . . .	135
<b>8 Conclusion and Future Work</b>	<b>137</b>
8.1 Conclusion . . . . .	137
8.2 Contributions of the Thesis . . . . .	138
8.3 Future Work . . . . .	138
<b>Bibliography</b>	<b>141</b>
<b>List of Figures</b>	<b>155</b>
<b>List of Tables</b>	<b>159</b>
<b>List of Symbols and Abbreviations</b>	<b>161</b>
<b>Appendix</b>	<b>167</b>

## CONTENTS

---

# Chapter 1

## Introduction

This chapter gives an introduction to the research work being proposed in this thesis, where the motivation of the thesis is highlighted along with the underlined goal of the research work. Afterwards, the thesis structure is described in detail.

### 1.1 Motivation

Nowadays the major trends of automotive applications such as electric vehicles, connectivity in particular vehicle-to-vehicle, vehicle-to-infrastructure communications (hereinafter referred to as V2X), semi-autonomous/autonomous driving, etc. will lead to the future of automotive world with human-centered safe and sustainable mobility through renewable energy and smart driving. Despite completely autonomous automated land vehicles are technically possible (e.g., Google driverless car [Google]) human's active role will not diminish but refocus on cooperative interactions by means of re-defined/re-invented human-vehicle interfaces. To realize this vision, advanced driver assistance systems (ADAS) have paved the way to the mass market automotive applications such as parking assistance, 3D surround view, lane departure warning, traffic sign and pedestrian recognition, etc. to assist the driver, enhance safety, improve convenience and economy.

Drowsy driving is a serious problem that impacts road safety and can cause huge damage to life and property. As conservatively estimated by National Highway Traffic Safety Administration (NHTSA), 1,550 deaths, 71,000 injuries, and \$12.5 billion monetary losses are the result of 100,000 police-reported crashes which are directly caused

## 1. INTRODUCTION

---

by drowsy driving each year in the United States [Drowsy14]. A study by the Federal Highway Research Institute (BAST) in Germany presented that drowsy driving was the second most frequent cause of serious truck accidents on German highways [EA05]. Due to severe damage caused by drowsy truck or bus drivers it is urgent to extend active safety to cope with driver drowsiness in commercial vehicles.

In recent years, ADAS systems with the feature of driver drowsiness/vigilance detection have been introduced by major automakers as active safety measures. *Driver Alert* from Ford Motor Company [Ford] and *Driver Alert Control and Lane Departure Warning* from Volvo [Volvo] are camera based lane tracking system which can detect abnormal car movement associated with potential drowsy driving. *Attention Assist* from Daimler [Daimler] is capable of monitoring steering behavior with the aid of high resolution steering sensor and issue visual or audible alarm if required. *Fatigue Detection System* from Volkswagen [VW] and *Driver Monitoring System* from Toyota [Toyota] are directly focusing on driver state in terms of head movement, facial features and ocular measures. The technical details of above mentioned ADAS systems are summarized in Table 1.1.

**Table 1.1:** Summary of ADAS systems featuring driver drowsiness detection

Vendor	System Name	Integrated Sensor	Technology and Algorithm
Ford	Driver Alert	Front and side mounted cameras	Camera based lane detection and tracking
Daimler	Attention Assist	Steering sensor	High resolution steering sensor based driving behavior monitoring
Volkswagen	Fatigue Detection System	Video camera	Driver monitoring based on head movement and facial features
Toyota	Driver Monitoring System	CCD camera with infrared LED	Driver monitoring based on ocular measures
Volvo	Driver Alert Control and Lane Departure Warning	CMOS Cameras	Car movement monitoring and lane tracking

The driver drowsiness measures being used in such ADAS systems are either derived from the human (driver-based approach) or from the vehicle (vehicle-based approach) [BSH12]. For driver-based approach, e.g., ocular measures are computed from images captured by machine vision sensors (mono-focal/stereo, grayscale/chromatic) [EHFK09]. The quality of such measures is significantly impacted by ambient illumination, head movement, facial expression, eyewear, etc. For vehicle-based approach, e.g.,

vehicle lateral position appears to be a key indicator of driver drowsiness, which can be estimated by detecting lane markings through vision sensors or cameras. A detailed survey on video-based lane detection techniques can be found in [MCT06], where the novel video-based lane estimation and tracking (VioLET) system was presented, which provides greater robustness to complex shadowing and lighting changes. However, mis-detection of lane marking edges or detected lane markings with low contrast due to varying lighting conditions, shadows, and complex scenarios on roadways make the robust lane position estimation often a challenge. Reliable solutions for driver drowsiness detection based on multi-measure approach and associated extensive sensor fusion are still sparse [BSH12].

Depth registration and exploitation in computer vision has been of significant and constantly increasing interest and importance. For instance, in automotive and robot vision systems, depth perception has predominantly been achieved by stereo vision systems and computationally intensive algorithms for disparity computation, e.g., block matching. The stereo camera system with its intrinsic demands on judicious placement and calibration of stereoscopic camera modules, however, was not in favor of cost-sensitive and mobile applications, such as mass market gaming electronics, human-computer interfaces, or robotic applications. Vibrations in mobile systems are another obstacle in the use of such systems.

In recent times, it is exciting to see that IR depth cameras, impedance spectroscopy (IS), electroencephalogram (EEG), and other advanced sensor electronics gain more and more attention in automobile industry worldwide. They bring new opportunity to meet the challenge in driver drowsiness detection, or say, in general driver status detection and intention prediction, by achieving better detection accuracy, better robustness against sensor failures, and better driving experience in human-vehicle interactions.

Seeing increasing demand on Automotive Safety Integrity Level (ASIL) <sup>1</sup> for electrical and electronic (E/E) systems in automobile, ADAS with ASIL-compliant diversified redundancy can contribute to the overall improved road safety for all the users of road. The performance and robustness of such systems are, however, as described above, limited by sensing capability and application environment. Reinforcement and expansion in system level with regard to extensive sensory input and computational intelligence

---

<sup>1</sup>Automotive Safety Integrity Level (ASIL) is a risk classification scheme defined by the ISO 26262 - Functional Safety for Road Vehicles standard [ISO26262].

## 1. INTRODUCTION

---

are therefore desirable. On the other hand, the automotive segment, including utility vehicles, continuously demands cheap and low-power system solutions for high volume applications in safety related driver assistance. To gain industrial acceptance affordable system solutions spanning from sensor components to application software are to be developed to the best possible extent.

### 1.2 The Goal of the Thesis

Driven by advanced sensing systems, sophisticated algorithms and growing computational resources, increasing leverage can be seen in the design of intelligent systems. In particular, human-machine-interface and its related monitoring and assistance systems, e.g., for multimedia (eye-tracking, gesture recognition, human-activity/behavior-recognition), ambient assisted living or active safety technologies for vehicles, can considerably benefit from the technological advances.

Aiming to underline the potential of IR depth cameras in such application fields a comprehensive study on advances of sensor electronics in 3D embedded vision, that can be adopted in automotive applications, in particular for safety related driver assistance purposes, is conducted in the thesis.

Furthermore, one major goal of the thesis is to investigate the extensive fusion of heterogeneous sensory sources for more robust driver drowsiness detection without compromising driving experience.

In addition, a low-cost/affordable system solution with small footprint and low-power energy profile is in the focus of this research work. On detection of drowsy driving, such a system can issue audible, visual, or tactile (vibration) signal to alert the driver, and to take necessary remedies to mitigate dangerous situations.

Finally, it is aimed to propose an emerging framework of multi-sensor intelligent assistance system towards generalized approach to driver status monitoring and as long-range goal, driver intention prediction for passenger and commercial vehicles, potentially also for aircrafts. Hence, in the thesis a multi-sensor approach based on color and depth vision, vehicle driving data, and biomedical driver data with efficient sensor fusion and machine learning system architecture has been pursued towards automotive mass market.

### 1.3 Thesis Structure

The content of the thesis is organized as follows. After the introduction in Chapter 1 an overview of the state-of-the-art ADAS systems is briefly given in Chapter 2 with simultaneous consideration of the role of such systems in a hierarchical control model. Technical trends and gaps in the field of automotive active safety with respect to driver drowsiness detection and the demands on the new generation of human-vehicle interfaces are discussed in this chapter. Chapter 3 highlights the advances of sensor electronics for ADAS with the focus on 3D embedded vision, such as novel IR depth cameras which are investigated in the context of automotive applications. Besides, when and where such diversified vision sensor technologies can be applied are discussed in the chapter as well. The building blocks for ADAS system modeling aimed at driver drowsiness detection, or say, general driver status monitoring, are discussed in Chapter 4 with regard to the state-of-the-art measurement and sensory principles, feature extraction from smart sensors, as well as the consideration of interconnection among building blocks. Based on previously discussed advanced sensor electronics and building blocks, Chapter 5 subsequently introduces advanced ADAS architectures that feature scalability and self-x-concepts. In addition, the problem definition, sensory data processing pipeline, and the associated classification techniques are addressed in this chapter. Afterwards, the proposed system architecture and its actual implementation for driver status detection and intention prediction are described in Chapter 6. The system implementation with respect to its hardware framework (e.g., system components and setup, multi-sensor interface), software framework (e.g., sensor data processing and fusion algorithm), as well as the associated human-vehicle interfaces are addressed in this chapter. The system validation through the experimental work in a simulated driving environment is described in Chapter 7. Finally, the thesis is summarized and concluded in Chapter 8.

## 1. INTRODUCTION

---



## Chapter 2

# Advanced Driver Assistance System

This chapter provides an overview of the state-of-the-art driving assistance system. The urgency of market penetration of ADAS in commercial vehicle systems to meet active safety demands is underlined here.

### 2.1 State-of-the-Art ADAS

As key components of smart driving Advanced Driver Assistance Systems (ADAS), in general, have been on the agenda of automotive and related industry for nearly two decades now. Inspired by the previous research projects, e.g., the Electronic Eye [See97] research program of the German Federal Ministry of Education and Research (BMBF) back to the mid nineties, Sleep-Eye-Detectors or Overtake-Monitors (OTM) [SKSK99] that focused both on CMOS sensing with high dynamic range and high speed as well as dedicated massively parallel digital computation platforms, an extension to ADAS has been pursued in the presented work towards smart driving that brings optimized human-vehicle interface and safety features.

Advanced driver assistance systems are intended for automated, adapted, or enhanced vehicle systems with better safety and adaptive features. Those features are designed to alert the driver to potential risks on the road, or to avoid collisions by using safeguards and taking over control of the vehicle if required. From adaptive cruise control, lane departure warning, traffic sign recognition, and pedestrian protection, to

## 2. ADVANCED DRIVER ASSISTANCE SYSTEM

---

adaptive lighting, night vision, to automatic parking, automatic braking and collision avoidance, to driver drowsiness detection, and finally to autonomous driving, modern ADAS systems have evolved rapidly with rich features towards future smart driving.

Adaptive Cruise Control (ACC) also called autonomous or radar cruise control, is an optional cruise control system for road vehicles that automatically adjusts the vehicle speed to maintain a safe distance from vehicles ahead. Lane Departure Warning (LDW) is a mechanism designed to warn a driver when the vehicle starts to move out of its lane (unless a turn signal is on in that direction) on motorways and arterial roads. Traffic sign recognition enables vehicle to recognize traffic signs on the road automatically, e.g., "speed limit" or "stop" or "turn left ahead", so as to remind/warn the driver to adjust his driving activity accordingly. Adaptive headlights can redirect the beams according to the moving direction and current position of the vehicle to increase the visibility around curves and over hills. As an active safety feature adaptive headlights are particularly helpful for driving at night or under poor light conditions.

The following systems are designed to minimize accidents and improve road safety by addressing the main causes of collisions: driver error, distractions and drowsiness. Automatic parking is an autonomous car-maneuvering system that moves a vehicle from a traffic lane into a parking spot to perform parallel, perpendicular or angle parking. The parking maneuver is achieved by means of coordinated control of the steering angle and speed which takes into account the actual situation in the environment to ensure collision-free motion within the available space. Collision avoidance also known as pre-crash system, forward collision warning system or collision mitigating system, uses radar (all-weather compliant) and sometimes laser and camera (both sensor types are ineffective against bad weather) to detect an imminent crash. Once the detection is done, these systems either provide a warning to the driver in case of an imminent collision, or take action autonomously without any driver input (by braking or steering or both). Driver drowsiness detection is able to awaken the drowsy driver via acoustic or optical pre-warning signals and assist him to get the vehicle back to the safe state.

Modern ADAS functions can be realized based upon vision/camera systems, radar sensor technology, as well as other advanced sensor electronics along with sophisticated hardware and software components. Many ADAS features can be found in cars as standard build-in functions, while some features are provided as add-on packages. In addition, there are various aftermarket ADAS solutions for late model cars.

## 2.2 ADAS in Joint Cognitive System

### 2.2.1 Hierarchical Control Model

Driving behavior can be regarded as control activity on controlled systems, here vehicles, to achieve predefined goals, for instance, reaching destination within acceptable time frame. Based on Neisser's cognitive cycle concept [Nei76], the Contextual Control Model (COCOM) is introduced to cope with human control of process by Hollnagel and Woods [HW05]. In this model the controller and controlled systems are viewed as an integral *Joint Cognitive System (JCS)*. As depicted in Fig. 2.1 the cyclical model describes the performance of JCS as a mixture of feedback and feedforward control activities.

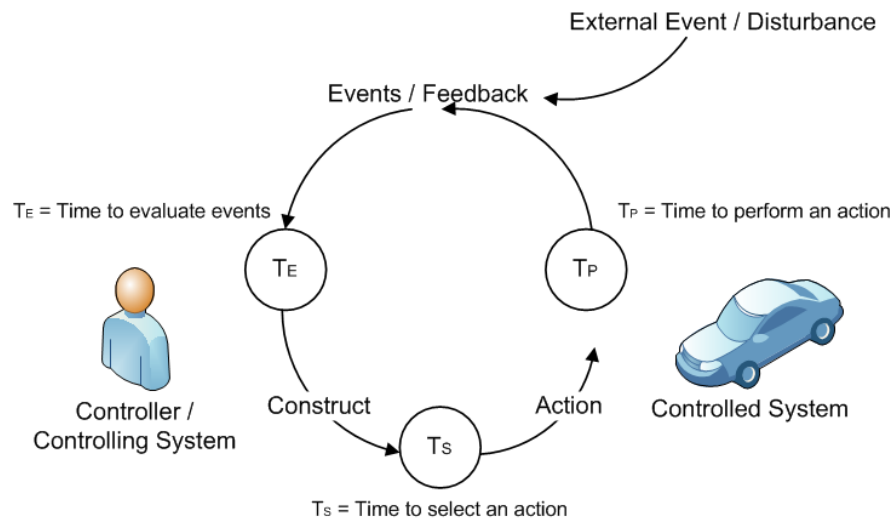


**Figure 2.1:** COCOM - The Contextual Control Model [EH98, HW05].

The model shows how action is carried out in a proactive way depending on the controller/controlling system (construct) and the expectations for future, which in turn is reactive to the events/feedback received by the system. The described cyclical model can be elaborated with temporal constraints of dynamic actions and be extended from individual to co-operative actions [Hol98].

A control process in pursuit of a single goal can be sufficiently described in COCOM. However, the driving behavior in general is a set of control processes pursuing several (sub-)goals within different time frames. In a top-down hierarchy four control layers are postulated to address the driving behavior: targeting, monitoring, regulating and

## 2. ADVANCED DRIVER ASSISTANCE SYSTEM

---

tracking. The targeting level sets the general goal(s) of the driving task, e.g., destination and direction, which determines the objectives for the underlying monitoring layer. It should be noted that other goals may be pursued simultaneously that are irrelevant to the driving task, e.g., talking to a passenger, listening to the radio. At the monitoring level it is focused on the control of the state of JCS, here the joint driver-vehicle system. It involves monitoring the location and state of the vehicle, as well as different conditions of the traffic environment, e.g., speed limits, congestion, weather. Control processes in the scope of regulating layer are intended to avoid collision with other traffic items. To achieve this sub-goal, it requires tracking control in the underlying layer to maintain the safe state of JCS. In general, tracking control involves the corrective actions against disturbances on the vehicle, e.g., sliding, jerking.

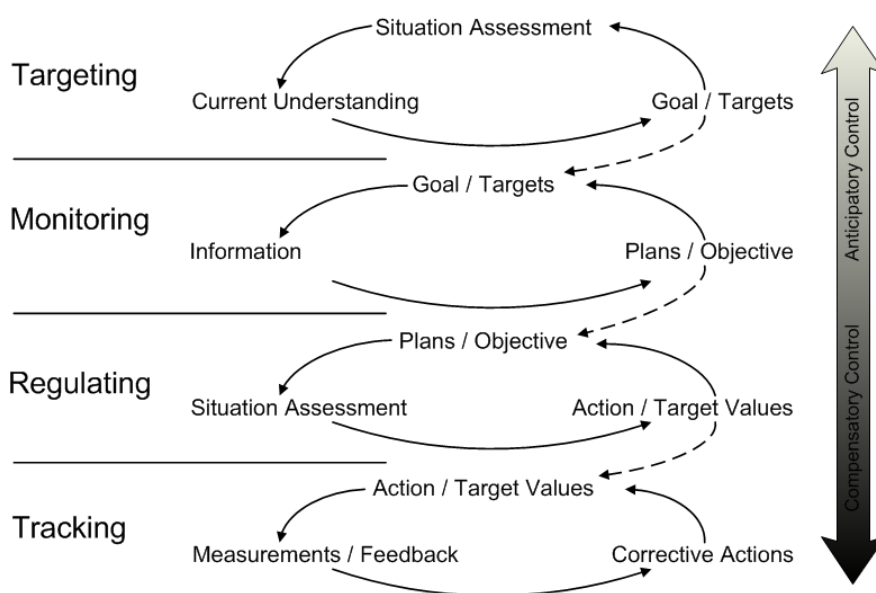


**Figure 2.2:** ECOM - The Extended Control Model [HNL03, HW05].

As discussed above, the practical driving task can be interpreted as a set of simultaneous, interrelated and layered control processes by extending the COCOM model to the extended control model - ECOM as shown in Fig. 2.2. A key property of ECOM is that the goals or target values for the control process of a given layer are determined by the control process in the upper layer [OPTE05].

Various ADAS functions can be mapped in the introduced hierarchical control model as illustrated in Fig. 2.3. In-Vehicle Infotainment System (IVIS) functions, e.g., radio

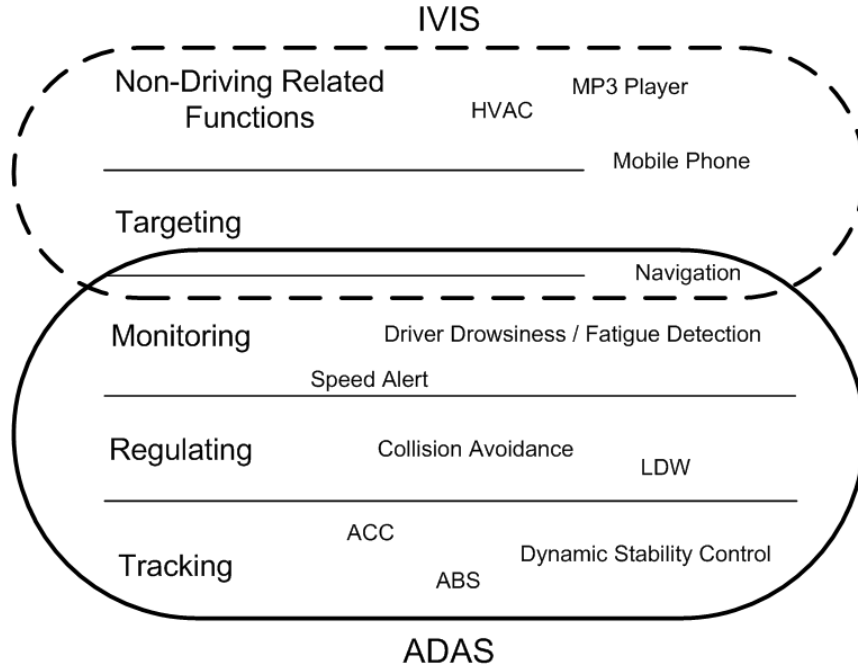


**Figure 2.3: ADAS in ECOM** - The proposed mapping of the ADAS/IVIS categories and some example functions onto the ECOM layers [OPTE05].

are referred here as well along with ADAS, though IVIS functions are usually not or less relevant to the driving control processes. ADAS functions can serve concurrent activities to achieve the target values at different control layers. For instance, the functions like ACC and ABS that contribute to the control of vehicle dynamics, belong to the tracking layer. The features like LDW, speed alert, as well as collision avoidance, which intentionally assist the driver to perform compensatory control on the vehicle to keep the safety margins to other items in road traffic while maintaining the travel direction and proper speed in an anticipatory manner, reside in the regulating and monitoring layers. Setting the destination and planning the route, which, e.g., can be assisted by the car navigation system, is regarded as targeting control process.

In particular, the scope of monitoring layer can be extended to cover the controller in JCS, here the driver, so as to address the overall safe state monitoring of the joint driver-vehicle system. Thus, driver drowsiness/fatigue detection serves the control process in monitoring layer along with, e.g., the speed alert function, which is focused on the vehicle state itself. Navigation or infotainment functions can support driving tasks on

## 2. ADVANCED DRIVER ASSISTANCE SYSTEM

---

targeting level by providing, e.g., route, traffic, weather information. Hence, it is often considered as an intersection of ADAS and IVIS. Non-driving related functions, such as HVAC, MP3 player, mobile phone, are categorized in IVIS mainly residing outside of ECOM.

### 2.2.2 Driver Status Monitoring and Intention Prediction

The ECOM model gives an overview on how control processes at different levels are in relation to each other, and how top level goal(s) can be broken down and propagate across interlayers to corrective vehicle control actions. For example, adjusting the route to destination after getting traffic information from the navigation system (targeting), as well as the car speed from dashboard (monitoring) may consequently trigger the control processes in reducing the car speed (regulating) and changing the lane (regulating/tracking).

The functional characteristics of the different control types of ECOM are summarized in Table 2.1. The control processes in targeting and monitoring are generally feed-forward, or say, anticipatory control, while the regulating control is usually a mixture of feedback and feed-forward control. The lower layer tracking control is a typically feedback referring to momentary corrections on the actual vehicle state according to a desired state.

**Table 2.1:** Summary of functional characteristics of different control types [HW05]

	Tracking	Regulating	Monitoring	Targeting
Type of control	Compensatory (feedback)	Anticipatory (feedforward + feedback)	Condition monitoring (feedback)	Goal setting (feedforward)
Demands to attention	None (pre-attentive)	High (unfamiliar actions) Low (familiar actions)	Low (intermittent)	High (concentrated)
Frequency of occurrence	Continuous	Medium to high (context dependent)	Intermittent, but regular	Low (preparations, re-targeting)
Information needs	Present	Present + Future	Past + Present	Past + (Present) + Future

Driver status monitoring and intention prediction proposed in the thesis is intended to serve/assist overall driving activity that can be interpreted as four control layers in ECOM (see Fig. 2.2). Although driver status along with vehicle dynamics represent the state of JCS in the "present" and "past", which can affect all the control layers,

such information of driver is viewed, however, less relevant to driving control processes, thus, remains as an open topic when designing a conventional transportation system. Similarly, looking into the information needed for regulating and targeting layers, driver intention implies future expectation and intended state of the JCS, therefore, can be utilized to improve the efficiency of the JCS and the overall driving experience in a proactive manner. For example, assuming the inattentive control of a drowsy driver is monitored and detected by the driver assistance system; warning is given subsequently, attempting to make the driver fully concentrate again on tracking and regulating tasks; the driver may want to slow down the vehicle and find a parking lot, in order to take a break; if the driver's intention can be predicted by the system, it may give route information to driver and/or issue control assistance, which help accomplish tasks in targeting and monitoring layers. Thus, general driver status monitoring and intention prediction can be employed in the JCS across different control layers of ECOM model to enhance driver-vehicle interaction.

Driver drowsiness/fatigue or vigilance/alertness detection is in the scope of general driver status monitoring. As mentioned previously in Chapter 1.1, there are driver-based approach and vehicle-based approach to driver drowsiness detection. The driver-based approach utilizes various direct measures including steering angle, pressure on throttle, brake, and clutch pedals, as well as indirect measures with respect to biomedical information of driver from ECG, heart beat rate (HBR), PERCLOS, to impedance spectroscopy and EEG. Direct measures can reflect the interaction between driver (controller) and vehicle (controlled system). For example, the relation between the steering wheel angle of driver's steering motion and the resulted lane position of vehicle has been studied in [SP96], and driver drowsiness is further estimated based on such information [TF05, DH06]. For indirect measures on the other hand, a vision-based drowsiness detector, using driver's ocular measures, has been proposed and implemented by Bergasa *et al.* based on a realistic driving simulator [BNS06], and afterwards it has been enhanced through IR stereo camera in a real-time driver monitoring system [GGB10]. In [Yu09] biosensors have been embedded in steering wheel to nonintrusively measure heart beat pulse signals for driver drowsiness detection. Furthermore, it should be noted that an ECG and EEG based non-intrusive driver assistance system for vital signal monitoring has been proposed by Ye Sun *et al.* in [SY14]. Finally, an imple-

## 2. ADVANCED DRIVER ASSISTANCE SYSTEM

---

mentation approach combining both direct and indirect measures, i.e., driver's steering motion and eye status, is proposed and validated in [FZC09].

For vehicle-based approach, lane position and its associated vehicle dynamics such as speed, heading angle are intensively investigated using video cameras and/or radar/laser sensors, and based on that various lane departure warning (LDW) systems are proposed in [MCT06, HYHF09, CBH09, ABTT10].

The approaches to determination of drivers' mind state are categorized in [DHUM11] in five different types of measures: (1) subjective report measures; (2) driver biological measures; (3) driver physical measures; (4) driving performance measures; and (5) hybrid measures. Hybrid multi-measure approach is preliminarily investigated in [BSH12], where sensor data fusion for two drowsiness metrics, i.e., PERCLOS (driver biological measures) and lane position (driving performance measures), is required to make an enhanced drowsiness estimate. In addition, the hybrid measures (the combination of above mentioned (3) and (4)) are believed to give more reliable solutions compared with single driver physical measures or driving performance measures, because the hybrid measures can minimize the number of false alarms and maintain a high recognition rate.

### 2.3 Discussion: Future Trend

Advanced driver assistance systems are one of the fastest-growing segments in automotive electronics worldwide. ADAS technology can be based upon vision/camera systems, sensor technology, car data networks, V2X systems. Next-generation ADAS will increasingly leverage wireless network connectivity to offer more added value by using car-to-car and car-to-infrastructure data. With an average of more than 100 Electronic Control Units (ECUs) on board, modern vehicles are already computer networks on wheels. Furthermore, ADAS systems enhance such vehicles to make them safer and easier to drive, thus more enjoyable. ADAS systems are being mastered to create autonomous driverless, self-driving cars in recent years.

Some interesting forms of ADAS are, e.g., special rear-view cameras required by NHTSA starting in May 2018 [NHTSA], face imaging knows when the driver is nodding off, warnings of local severe weather or disasters; smartview mirror, lane departure



warning systems and more. Another point here is the prevailing ISO 26262 "Road vehicles - Functional safety" [ISO26262]. The system design and development for automotive E/E systems, especially for safety related applications, e.g., electric power assisted steering (EPS), shall be carried out in accordance with ISO 26262. The system concept being proposed in the thesis, using multi-sensor architecture, realizes on the one hand the driver state monitoring with enhanced features, and on the other hand such design concept with diversified redundancy improves the system dependability, thus is in line with the mind-set of ISO 26262 standard.

Speaking of driver drowsiness detection, an interesting example of commercial products is StopSleep [StopSleep], a discrete add-on product to address drowsy driving, which had the first press release in July 2013. Before this many studies have been conducted including the previous study about drowsy driving in relation to driver's skin impedance [LBK13] in the frame of this research work. The anti-sleep alarm StopSleep recognizes the loss of concentration and prevents microsleeps<sup>1</sup> during driving by measuring and evaluating the skin conductance of driver (electrodermal activity - EDA). As a driver-based approach to drowsiness detection (see Section 2.2.2), such low-cost add-on product, applicable for almost all drivers, car brands and models, provides another option to tackle drowsy driving problem, although drivers may feel less comfortable when wearing this gadget during driving. It is expected to see more technologies and solutions thriving in such ADAS domain, that have novel sensory principles, non-intrusive user interfaces, decent detection rate (against drowsy driving), and affordable prices. They can cooperate with other on board systems in vehicle, so as to contribute to the integral system solution for drowsiness detection, driver warning, as well as vehicle control assistance if required.

Despite plenty of researches, there is still a lack of multi-sensing integral system solutions with non-intrusive user interfaces that are able to cope with multi-modality of driver status. A generalized approach to driver status monitoring and intention prediction is demanded.

In general, the direct and indirect measures in driver-based approach give clues to driver (controller) state, while the measures being evaluated in vehicle-based approach reflect the vehicle (controlled system) state. The matrices derived from both approaches

---

<sup>1</sup>A microsleep is an episode of sleep lasting up to 30 seconds during which external stimuli are not perceived. Microsleeps are associated with excessive sleepiness and automatic behavior [ESST01].

## **2. ADVANCED DRIVER ASSISTANCE SYSTEM**

---

can be used to define the state of JCS jointly, so as to improve the confidence of decision making and the performance of driver assistance. Thus, solutions that utilize both approaches will be demanded in the future smart driving.

## Chapter 3

# Advanced Embedded Vision Systems for ADAS

This chapter gives a survey on advanced embedded vision systems and sensor electronics with great potential for the use in ADAS (and/or IVIS), e.g., instrument cluster (dash board), head-up display (HUD), car navigation/infotainment system, as well as the emerging autonomous driving technology. 3D embedded vision systems are of particular interest here, thus, will be addressed in the focus of Section 3.1. Afterwards, two typical variants of such systems, i.e., one time-of-flight based and another structured light based IR depth cameras being investigated in the research work are discussed in Section 3.2. The relevant algorithms and methods for 3D embedded vision and signal processing in ADAS are addressed in Section 3.3. Finally, the comparison among the state-of-the-art depth cameras and the selection of 3D embedded vision sensors for the presented project are discussed in Section 3.4. Other building blocks with novel sensory principles and measurement techniques for ADAS will be addressed in Chapter 4.

### 3.1 Technology Review for 3D Embedded Vision

Depth information for automotive and robotic tasks was mostly obtained by stereo camera setups. The advent of CMOS depth sensors, based on time-of-flight-principles, opened new possibilities and application fields from automotive, robotics, to HMI tasks. The Institute of Integrated Sensor System's (ISE) research bases on such activities back to the end nineties, related to CMOS sensor system design and intelligent system

### 3. ADVANCED EMBEDDED VISION SYSTEMS FOR ADAS

---

design for, e.g., Overtake-Monitors (OTM) [SKSK99] or eye-tracking for 3D display applications [LXK12].

Modern depth cameras for 3D embedded vision can be characterized by different means, e.g.,

- Configuration: mono or stereo vision system, multi-camera system
- Light source: active or passive illumination
- Technology: triangulation, time-of-flight (ToF), light-field, etc.
- Sensor type: line sensor, array sensor, or a combination thereof
- Perception mechanism: scan or flash based profilometry

As representative technologies being adopted in 3D embedded vision: stereo vision, laser scan triangulation, structured light and triangulation, light-field as well as time-of-flight imaging are addressed in the following subsections.

#### 3.1.1 Passive Triangulation: Stereo Vision

Stereo vision systems, which use passive triangulation to calculate distance, have been commercially available for more than a decade and become a prevailing system component in many application fields such as robotics.

By emulating human eyes' stereo imaging capability, such system perceives images using two aligned and calibrated cameras, and finds the correspondences between points seen by one camera and the same ones seen by the other camera. Afterwards, 3D location of the points can be calculated with the correspondences and a known baseline separation between cameras. Stereo vision does not explicitly require a built-in light source in the system, hence its fundamental technology of 3D perception is called passive triangulation. The principle of triangulation being used in stereo vision system is illustrated in Fig. 3.1.

Assuming perfectly undistorted, aligned stereo imagers and known correspondence, the depth  $Z$ , as depicted in Fig. 3.1, can be found by similar triangles; the principal rays of the imagers begin at the centers of projection  $O_l$  and  $O_r$  and extend through the principal points of the two image planes at  $C_l$  and  $C_r$ . The depth to the point  $P$  in the scene is inversely proportional to the disparity between stereo views, where the

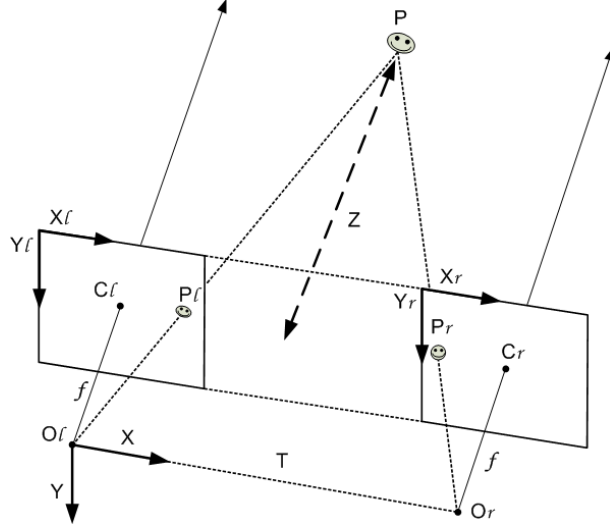


**Figure 3.1: Stereo triangulation** - Epipolar geometry of stereo coordinate system for undistorted rectified cameras: the point  $P$  in the scene is viewed as  $P_l$  and  $P_r$  in the image planes; the depth of  $P$  is denoted as  $Z$ ; two principle points are denoted as  $C_l$  and  $C_r$  respectively, where principal rays intersect the image planes; the camera coordinates are relative to the left camera's center of projection  $O_l$ ; the cameras of the same focal length  $f$  are row-aligned and displaced from one another by  $T$  [BK08].

disparity is defined by  $d = x_l - x_r$ . With a known baseline separation between cameras, here  $T$ , the depth  $Z$  can be derived as follows:

$$\frac{Z}{T} = \frac{f}{d} = \frac{f}{(x_l - x_r)} \Rightarrow Z = \frac{T \cdot f}{(x_l - x_r)}. \quad (3.1)$$

Furthermore, if the geometric arrangement of the stereo vision system is known, 3D location of the points can be computed accordingly.

Stereo vision in practice, however, involves the following steps as illustrated in Fig. 3.2: (a) capture the raw images from stereo cameras; (b) undistortion of raw images; (c) rectify and (d) crop of the intermediate imagery data from the previous process step, and subsequently the correspondence matching and disparity calculation are carried out.

A typical block diagram of ADAS stereo front view system is shown in Fig. 3.3, where the key components and their interconnections are illustrated. Compared to mono view system, stereoscopic system is able to detect objects more reliably due to additional depth information provided by dense stereo imaging, thus makes the stereo

### 3. ADVANCED EMBEDDED VISION SYSTEMS FOR ADAS

---

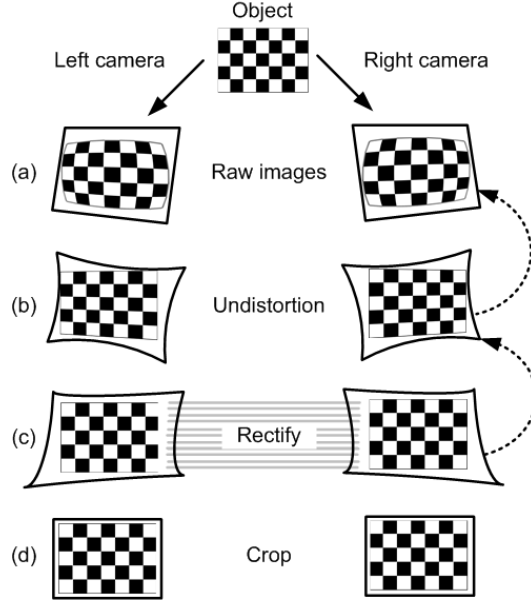


**Figure 3.2: Stereo rectification** - For the left and right camera, the raw image (a) is undistorted (b) and rectified (c) and finally cropped (d) to focus on overlapping areas between the two cameras; the rectification computation actually works backward from (c) to (a) (see dashed arrow in figure) [BK08].

front view camera system more accurate and robust, however, at higher cost with additional imaging sensor and increased hardware and software complexity [Nik14].

Even though the search space for correspondences can be narrowed down by using prior knowledge of the geometry of the system, and/or utilizing the known information of the specific application field, such operation is in general computationally very expensive, therefore improving the search algorithm for correspondences like in [PN12] becomes crucial for real-time automotive applications such as ADAS. Recently, on the strength of continuously increased embedded computation power, advanced studies on stereo vision and the associated emerging applications, such as DSP platform based obstacles detection [ZWB12] or x86 machine based pedestrians detection along with distance measurement [BBS11] in real time, are observed in the automotive industry.

There are available commercial products such as PointGrey Bumblebee2 (see Table 3.2) and Tobii Pro eye tracking products (remote eye tracking systems) [tobiipro].

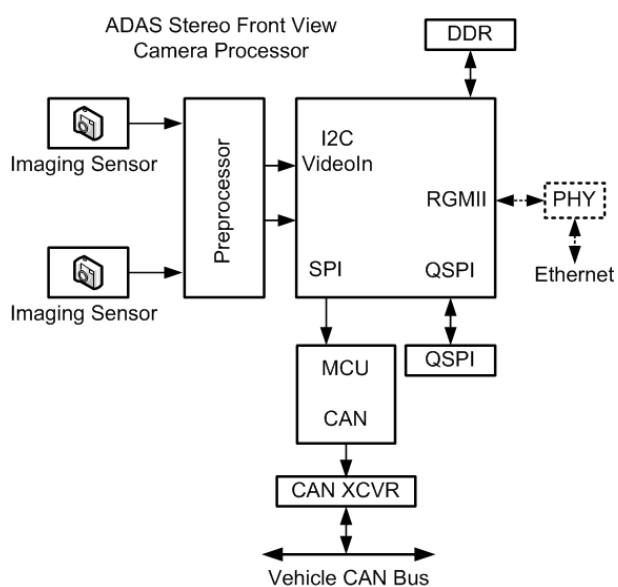


**Figure 3.3: ADAS stereo front view system** - Key components such as imaging sensors, preprocessing block, central processing unit (CPU), memory block (DDR), and various communication interfaces, i.e., CAN, SPI, QSPI (Quad Serial Peripheral Interface), I2C, Ethernet (RGMII interface support), are visualized in the diagram. Preprocessing stages such as image rectification and disparity computation in stereo camera system, are typically carried out in an FPGA or ASIC. The stereo front view camera system is connected to the vehicle via CAN bus [Nik14].

#### 3.1.2 Active Triangulation

Active triangulation differs from passive triangulation in that a light source is explicitly required in the system to illuminate the scene. On the other hand, similar to the passive triangulation, the reflectance of the objects in the scene is perceived and further analyzed, so as to reconstruct the 3D object information.

##### 3.1.2.1 Lightsheet

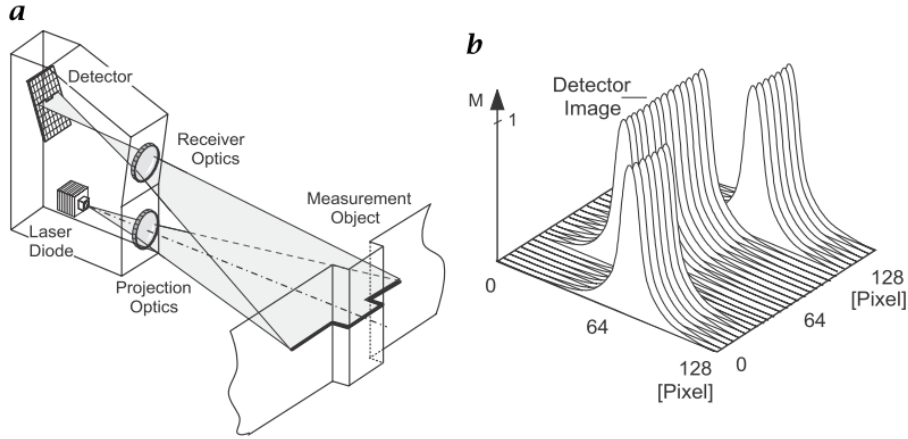


**Figure 3.4: Lightsheet triangulation** - (a) instrument; (b) detector image [SHM00].

In [SHM00] Schwarte *et al.* provided a comprehensive overview of the techniques used for 3D geometry measurements and object surface inspection by utilizing 3D sensors based on the triangulation principle. An example of such techniques, here *lightsheet* triangulation instrument (2D laser triangulation), is schematically shown in Fig. 3.4a, where a laser beam is expanded via cylindrical lenses to a light sheet, and projected on the measurement object. A light line, i.e., a so-called height profile of the measurement object is formed at the cross section of the lightsheet and the object's silhouette. The height profile can be captured by 2D image sensor, here a CCD detector, and result in a generated charge image as shown in Fig. 3.4b. To have the entire measurement object rendered sharply with such triangulation instrument, so as to gain the maximum depth resolution, the image plane, lens plane, and the plane of the object shall have a common axis (through *Scheimpflug Intersection*) to meet the *Scheimpflug condition* [SHM00]. Such a 3D embedded vision system based



on the lightsheet technique generally uses 2D light source, 2D camera and 1D scanner (one-dimensional movement) to gain the 3D information of the object under inspection.

#### 3.1.2.2 Structured Light

As another approach of active triangulation, a structured light system generally employs one camera (viewer) and one structured light emitter (projector) that uses any form of light with known pattern(s). In order to gain as good depth resolution as possible, the light pattern being projected on the measurement object needs to be well recognized from the scene, thus, it demands high power and well focused light source. In addition, the background illumination in the observed scene shall be properly filtered to remove brightness fluctuations.

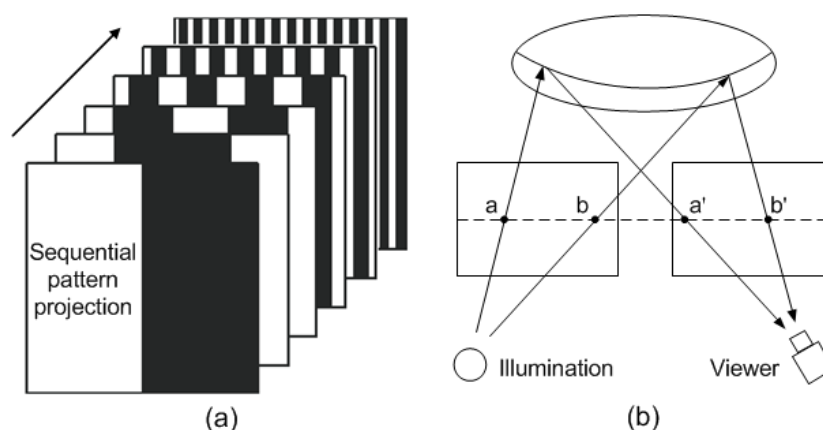


**Figure 3.5: Structured light** - (a) Sequential pattern projection; (b) Side-by-side setup of projector (illumination) and viewer (camera).

As an example of structured light instrument, binary gray code based sequential pattern projection is illustrated in Fig. 3.5.

Kinect uses a static spatially encoded IR pattern projected into the scene that is in form of scattered points (*sparkle* pattern) as depicted in Fig. 3.6a. The pattern is deformed as it falls onto the objects in the scene. A camera inside of Kinect captures an image of the scene and decodes the result. This method calculates a single depth value for a group of projected pixels. It takes multiple spatially encoded pixels to map back to unique camera pixels, which results in a loss of depth resolution. However, the advantage of this technique is that depth information can be retrieved with single one capture. Another camera of Kinect records color/intensity image in parallel to the

### 3. ADVANCED EMBEDDED VISION SYSTEMS FOR ADAS

---

depth registration. Along with the spatial information in 2D image (color or intensity), the calculated depth can be used to define the points in X, Y, and Z coordinates in terms of point cloud, so as to represent the external surfaces of objects in the scene (see Fig. 3.6b).

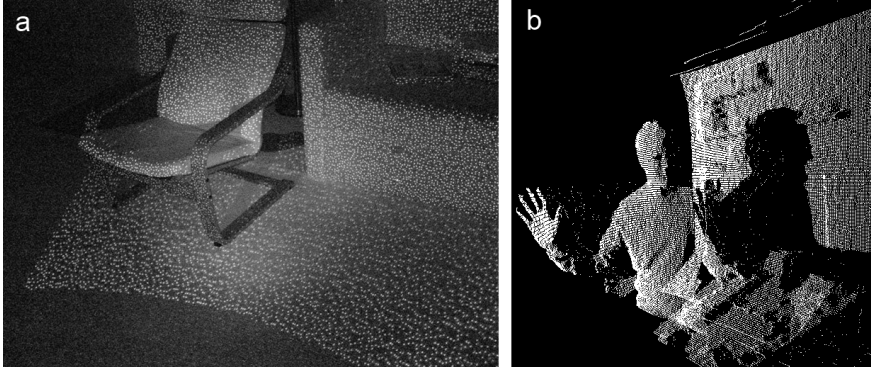


**Figure 3.6: Kinect** - (a) Infrared pattern projection; (b) Calculated results (point cloud) with corrected depth projection.

In general, a trade-off needs to be made between the depth accuracy and the acquisition time in range sensing based on time-multiplexed structured light. An interesting method combining color sensing and structured light has been proposed in [CKS98], where the number and form of the projection patterns are adapted to the characteristics of the scene in the acquisition process, and color is used for light plane labeling. In such a way, the dimension of the pattern space can be increased without raising the number of projection patterns.

The representative commercial products are e.g. Microsoft Kinect Sensor, ASUS Xtion, and structure lighting based on TI Digital Light Processing (DLP), etc.

#### 3.1.3 Light-Field Imaging

A light-field camera, also called a plenoptic camera, is based on CMOS image sensor that uses a microlens array to capture local incident angle and intensity information from the light in the scene. Such light field information can be utilized for range imaging and producing 3D-TV, or to improve the solution of computer graphics and computer vision-related problems, and to make digital plenoptic pictures that can be refocused after they are taken (after-the-fact-refocusing).

### 3.1 Technology Review for 3D Embedded Vision

In 1908, Gabriel Lippmann proposed the first light-field camera using *integral photography* as the fundamental technology. In 1992, Adelson and Wang proposed the design of a plenoptic camera in [AW92] that can be used to significantly reduce the correspondence problem in stereo matching, where an array of microlenses is positioned at the focal plane of the camera main lens, and the image sensor is located slightly behind the microlenses array. In such a way, the displacement of image parts that are not in focus can be analyzed, and the depth information can be extracted. In early 2005, Ng *et al.* published a technical report [NG05] explaining that a standard plenoptic camera can potentially be used to refocus an image after being captured. Based on this work, Lytro – the first consumer light-field digital camera capable of refocusing images after being taken, was introduced in 2011. The block diagram of Lytro camera system is illustrated in Fig. 3.7.

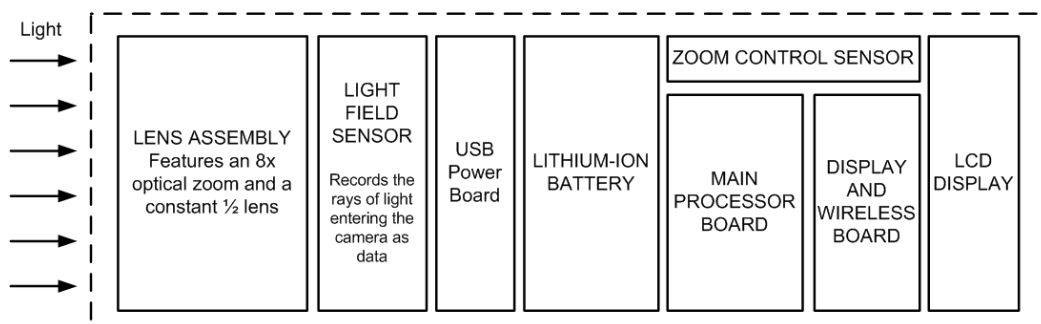


**Figure 3.7: Lytro light-field camera - A deeper look inside [Lytro].**

The recent advances in light-field cameras and light-field displays, as well as their applications in entertainment, consumer devices, industrial applications, and medical imaging, strengthen the vitality of light-field imaging. Despite its usage in automotive applications has not emerged as of today, the technology such as light-field display has potential to be used for augmented reality towards enhanced HUD application in the future.

#### 3.1.4 Time-of-Flight

The distance  $d$  of an object can be determined by the echo (turn-around) time-of-flight (ToF) of an emitted light signal and reflected back from the object to the sensor via  $d = \frac{c \cdot ToF}{2}$ , where  $c$  represents the light velocity ( $c \approx 3 \times 10^8 m/s$ ). This method

### 3. ADVANCED EMBEDDED VISION SYSTEMS FOR ADAS

---

is suitable for measuring distance starting from some centimeters to several hundreds of meters with relative accuracies of 0.1%. The range can even be extended up to thousands of kilometers depending on the power of light source. The time-of-flight technique is well known in various wave length ranges in military as well as civilian applications, attracting the attention of researchers since the late 90s until today.

#### 3.1.4.1 3D Laser Scan and LIDAR

LIDAR, known as Laser Illuminated Detection and Ranging, or referred as acronym of Light Detection And Ranging, sometimes also referred as Laser Detection and Ranging (LADAR) in the literature, in various forms, has become an essential part of autonomous navigation of automobiles and unmanned ground vehicles (UGVs). Utilizing laser illumination and ToF principle, the LIDAR technology enhances such systems in the capability of obstacle detection and avoidance. Furthermore, in many applications besides locating the obstacles, identification and classification of objects through 3D perception is crucial for situational planning, as robots are increasingly required to operate in harsh environments and interact safely and effectively with humans, other vehicles, and their environment. For LIDAR sensors there are a plenty of interesting research studies along with first prototypes in automotive applications.

A scanning LIDAR system with generated sensor features is discussed in [NMEV94] aimed at applications in the automotive field, such as obstacle avoidance, navigation, as well as the potential usage for human-machine-interface, factory floor traffic control, etc. in industry. A low-cost compact MEMS scanning LADAR system for robotic applications is presented in [MYBQ12], where improved system sensitivity, low cost, miniaturization, and low power consumption as the main goals have been pursued. The block diagram of the LADAR System is illustratively described in Fig. 3.8, where a two-axis MEMS mirror is used to establish the angular direction for the scanning procedure.

To investigate near, mid and far infrared laser illuminators, in particular for on-board automotive applications, an experimental study has been conducted in [SRMC00] by assessing the ability to detect painted car body panels and various reflectors with 850, 910, 1560, 5600 and 8100 nm LIDAR transceivers. A  $1.6\mu\text{m}$  LIDAR wavelength

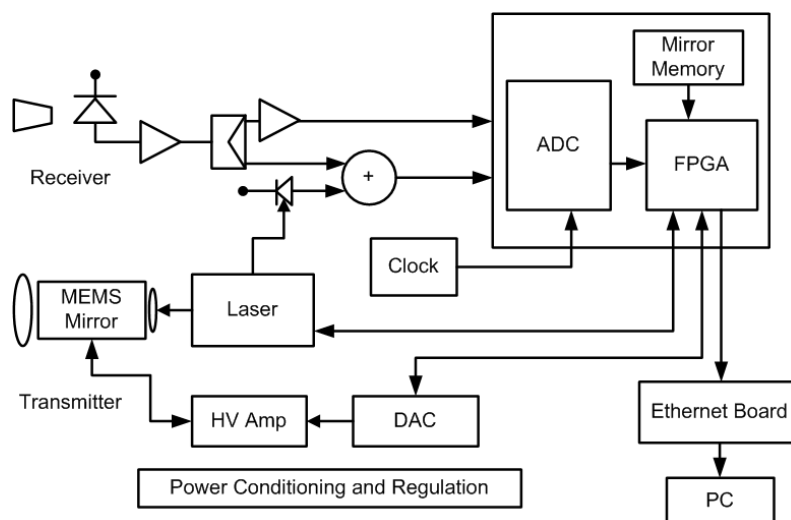


**Figure 3.8: LIDAR imaging system** - The system components such as laser light source equipped with MEMS mirror, power conditioning and regulation, laser detector with signal conditioning, analog-to-digital converter (ADC), and embedded processing unit in terms of FPGA, as well as Ethernet communication interface towards back-end PC are illustrated in the block diagram [MYBQ12].

is suggested as optimum in the study with the consideration of eye-safe laser. Furthermore, an approach to pedestrian detection and tracking using in-vehicle LIDAR has been proposed in [OSST11].

Recently, Google driverless car becomes a prominent project in the field of autonomous driving. The device mounted on top of Google's driverless car is a Velodyne 64-beam LIDAR sensor that can rotate  $360^\circ$  and take up to 1.3 million readings per second (see Fig. 3.9).

As mentioned previously there are available line or array LIDAR sensors with gray-scale, color sensing capabilities or the combination thereof. In many cases, such systems require scanning the light through the scene, which makes it difficult to obtain high frame rates. Instead of scanning a flash LIDAR system based on two-dimensional sensor arrays can provide 3D imaging data with a single capture. But they are cost prohibitive to deploy in robotic and UGV platforms. Low-cost flash LIDAR systems with high frame rate are therefore in high demanded for such applications.

The representative commercial products available on the market are e.g. Velodyne HDL-64E LiDAR sensor [Velodyne] and SICK Laser Scanner [SICK].

### 3. ADVANCED EMBEDDED VISION SYSTEMS FOR ADAS

---



**Figure 3.9: Google self-driving car prototype with Velodyne HDL-64E LIDAR sensor** - Velodyne 64-beam LIDAR sensor is mounted on top of a Google driverless car collecting 3D information of car's surrounding environment [Google, Velodyne].

#### 3.1.4.2 ToF Depth Camera

A time-of-flight based depth camera with active illumination, sometimes also referred as flash LIDAR, is capable of simultaneously perceiving reflectance and distance information of objects in a scene at real-time video frame rates. The obtained intensity image and depth image are registered pixel by pixel accordingly and do not require extra effort for image matching which is crucial in conventional stereo imaging systems.

Depending on the employed modulation techniques ToF cameras can be classified in three categories, i.e., continuous wave (CW) modulation, pulse modulation, and pseudo-random modulation. Some typical ToF depth cameras available on the market since 2010 are depicted in Fig. 3.10.

A typical ToF camera consists of a modulated light source, e.g., laser or LED, a pixel array, capable of detecting the phase of the reflected light, and an ordinary optical system for focusing the light onto the sensor (see Fig. 3.11a). The light is given within a modulation envelope by rapidly turning the light source on and off. Distance measurement can be achieved either by measuring the phase shifting of the transmitted light within the modulation envelope as received at the pixel array, or through direct measurement on the time-of-flight of the emitted light.

### 3.1 Technology Review for 3D Embedded Vision

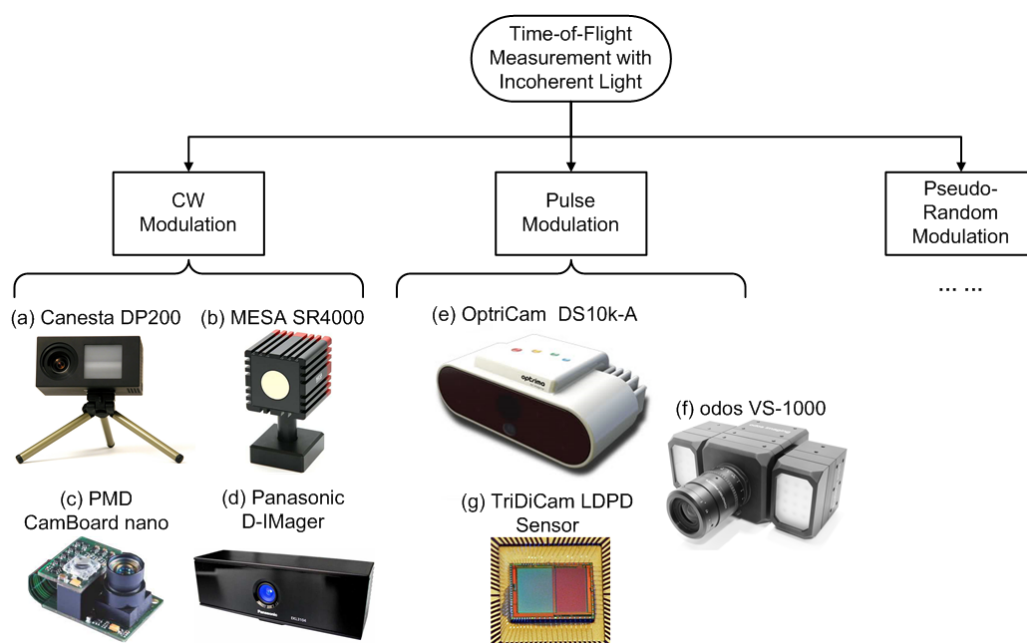


**Figure 3.10: Commercial available ToF cameras and sensors** - (a) Canesta DP200 [Canesta]; (b) MESA SR4000 [MESA]; (c) PMD CamBoard nano [PMDnano15]; (d) Panasonic D-Imager [Panasonic]; (e) OptriCam DS10k-A [Optrima]; (f) odos VS-1000 [odos15]; (g) TriDiCam LDPD sensor [TriDiCam].

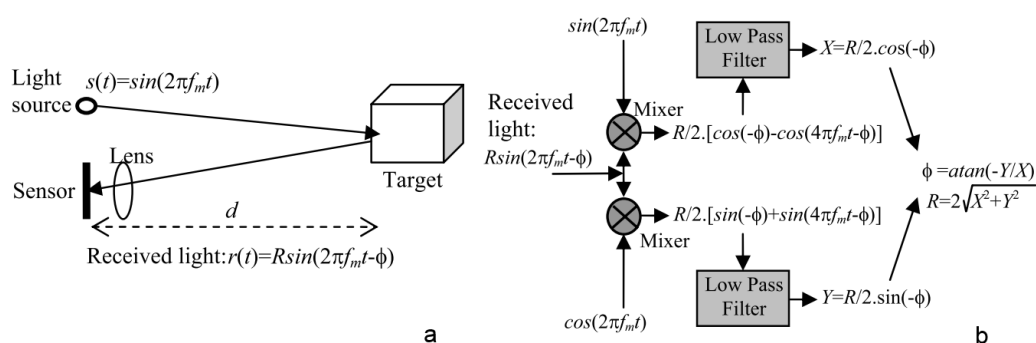


**Figure 3.11: Time-of-Flight: continuous wave modulation** - (a) Time-of-flight measurement based on continuous wave modulation; (b) A method of phase/amplitude calculation [GYB04].

### 3. ADVANCED EMBEDDED VISION SYSTEMS FOR ADAS

---

Let  $s(t) = \sin(2\pi f_m t)$  be the transmitted light where  $f_m$  is the modulation frequency. The light being reflected from the target object, here  $r(t)$  in Eq. (3.2), falls on a sensor pixel with a phase shift  $\phi$ :

$$r(t) = R\sin(2\pi f_m t - \phi) = R\sin(2\pi f_m(t - \frac{2d}{c})), \quad (3.2)$$

where  $R$  is the amplitude of the reflected light,  $d$  is the distance between the sensor and the target, and  $c$  denotes the light velocity ( $\approx 3 \times 10^8$  m/s). From Eq. (3.2) it has

$$\phi = 2\pi f_m \cdot \frac{2d}{c} = \frac{4\pi f_m d}{c}. \quad (3.3)$$

Thus, the distance  $d$  can be calculated from Eq. (3.3) as follows:

$$d = \frac{c\phi}{4\pi f_m}. \quad (3.4)$$

The maximum unambiguous phase delay that can be detected using ToF is a full cycle of the modulation period, which corresponds to an unambiguous range of  $\frac{c}{2f_m}$ . For instance, the maximum unambiguous range for  $f_m = 50$  MHz is 3 m. As an illustrative example of ToF principle with continuous wave modulation, it is explained in [GYB04] that the phase and amplitude of the reflected light can be gained through signal processing techniques, e.g., using mixers and low-pass filters as depicted in Fig. 3.11b. A survey on such ToF depth cameras based on lock-in sensor pixels employing continuous wave modulation can be found in [FAT11]. Despite known issues of lock-in ToF cameras such as low spatial resolution, range ambiguity, ambient light noise, motion artifacts, etc. that can be coped with viable technical solutions, such ToF cameras can offer depth and intensity image registration at real time frame rate, compact design, reduced power consumption, thus prove to be especially suitable for automatic acquisition of 3D models in real time [FAT11].

The representative ToF cameras available on the market are PMDTech CamCube3, PMDTech CamBoard nano, MESA SR4000, Canesta DP208, Fotonic B70, Panasonic D-Imager, which feature continuous wave modulation with lock-in pixels, as well as TriDiCam based on pulse modulation with lateral drift-field Photodetector [Elk05], and odos VS-1000 using pulsed light with fast gating.

Due to the virtue of time-of-flight sensor technology the depth camera is suitable for image post-processing to segment foreground/background very robustly, resolve ambiguities, track objects, as well as to estimate object size and shape, measure volumes,



surveil a target zone, and to count objects or people. The application fields span from logistics/warehouses, factory automation, surveillance and security, robotics, medical and physical therapy to automotive.

### 3.2 Investigated Depth Cameras in the Project

As discussed in Section 3.1, a depth camera system is capable of perceiving reflectance and distance information of objects in a scene (at real-time video frame rates), so as to enable 3D embedded vision. Thus, it is of particular interest to be used for the vehicle interior monitoring, or for the human-machine-interface as part of ADAS system. DriMix and Microsoft Kinect are selected for the investigation in the project.

#### 3.2.1 DriMix Micro-3D-Camera

This research work is involved in the development of a novel time-of-flight based depth camera, i.e., DriMix Micro-3D-Camera, which is aimed at more compact system design and better energy efficiency for 3D embedded vision intended for industrial and automotive applications such as robot control, surveillance, unmanned ground vehicle, driver assistance, as well as its potential use as commodity device in consumer electronics. It is carried out internally as the 3DKM project by the Institute of Integrated Sensor System (ISE) as subcontractor for the Federal Ministry of Education and Research (BMBF) project "Design of a Micro-3D-Camera System for the Rapid Time-Resolved 3D-Shape Acquisition of Objects" coordinated by the company iC-Haus GmbH in Bodenheim, Germany. The scope of the 3DKM project in ISE is specified as follows.

- Modeling of the depth/range measurement of the DriMix sensor.
- Fast prototyping of DriMix Micro-3D-Camera with the focus on the realization of camera control logic and data transmission.
- Calibration, validation and test of the DriMix camera system.

The DriMix Micro-3D-Camera is based on a single sensor coupled with active illumination employing the time-of-flight principle as introduced in Section 3.1.4, in an optical embodiment. The sensor has been realized by iC-Haus with a sub- $\mu\text{m}$ -SOI

### 3. ADVANCED EMBEDDED VISION SYSTEMS FOR ADAS

---

technology with  $80 \times 60$  pixel array in  $50\mu\text{m} \times 50\mu\text{m}$  pixel size. The DriMix features a proprietary sensor technology from iC-Haus based on a patented drift-field-mixing concept [HERZ05] to perceive the reflected light pulses and calculate the time-of-flight of emitted light pulses, which therefore can be categorized into ToF pulse modulation technique (see Fig. 3.10). The basic measurement principle of DriMix is briefly depicted in Fig 3.12. The generated sensory data is a pair of images, i.e. grayscale and depth maps.

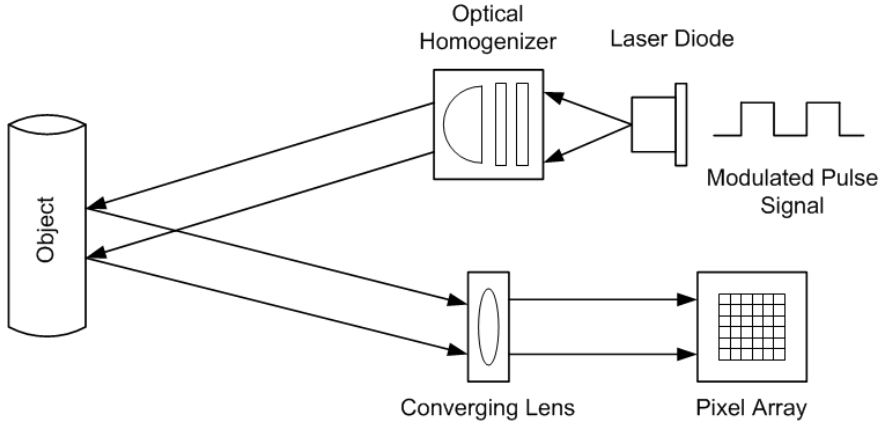


**Figure 3.12: DriMix ToF pulse modulation** - Pulse modulated time-of-flight measurement principle.

As illustrated in Fig. 3.13 the system modeling of DriMix Micro-3D-Camera has been conducted in the 3DKM project. The first prototype of control and communication interfaces based on Altera Cyclone III FPGA and the dedicated circuits for A/D-conversion and sensor interfacing is depicted in Fig. 3.14.

More details of the DriMix sensor components are given in Fig. 3.15, including the laser diode driver (iC-HG1M module), sensor layout (iC-TS006 module), and the control electronics consisting of FPGA prototyping board and AX01 expansion board. The DriMix camera board including optical sensor, IR light source, and the integrated control and communication interfaces is shown in Fig. 3.16. The demonstrator of DriMix Micro-3D-Camera and its exemplary application in robotics, i.e., palletising car tires, are presented in Fig. 3.17(a) and (b) respectively.

### 3.2 Investigated Depth Cameras in the Project

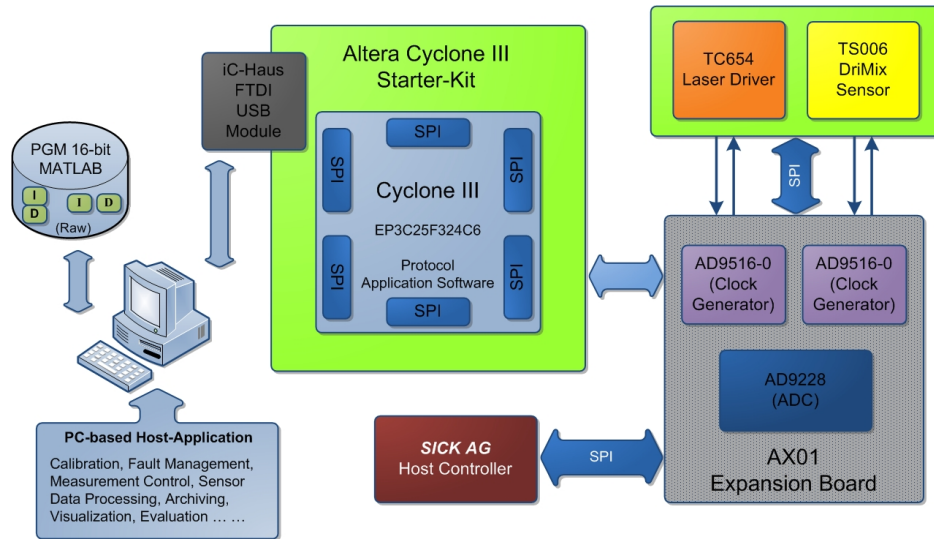


**Figure 3.13: DriMix system diagram** - The block diagram indicates the sensing part at the front-end camera board, the control and communication interfaces on an FPGA, and the processing of sensory data at the back-end PC.

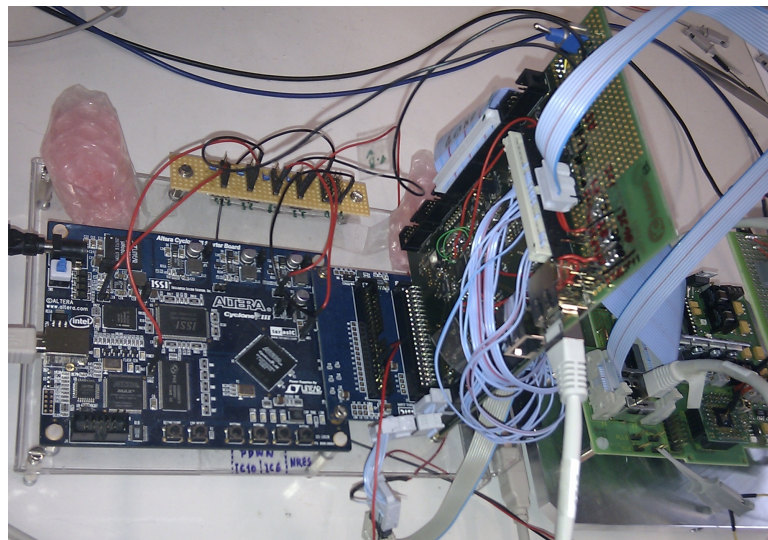


**Figure 3.14: DriMix control board (prototype)** - The FPGA-based prototyping board with control and communication interfaces to the DriMix camera board.

### 3. ADVANCED EMBEDDED VISION SYSTEMS FOR ADAS

---

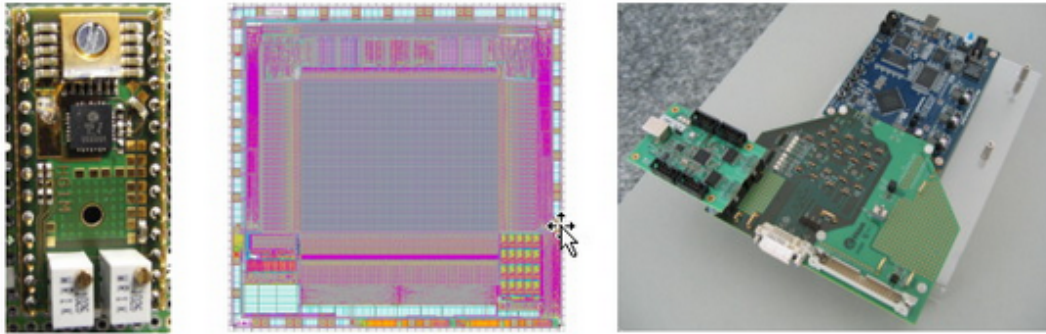


**Figure 3.15: DriMix sensor components** - The sensor components from left to right, emitter, detector, control electronics [ISE3DKM].

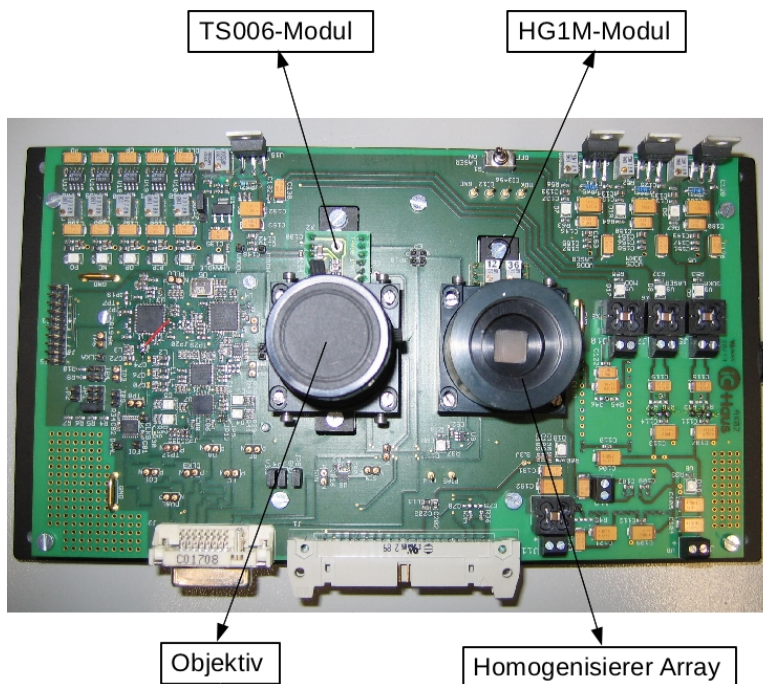


**Figure 3.16: DriMix camera board** - The camera main board with sensor and IR light source (courtesy and copyright iC-Haus) [BMBF3DKM].

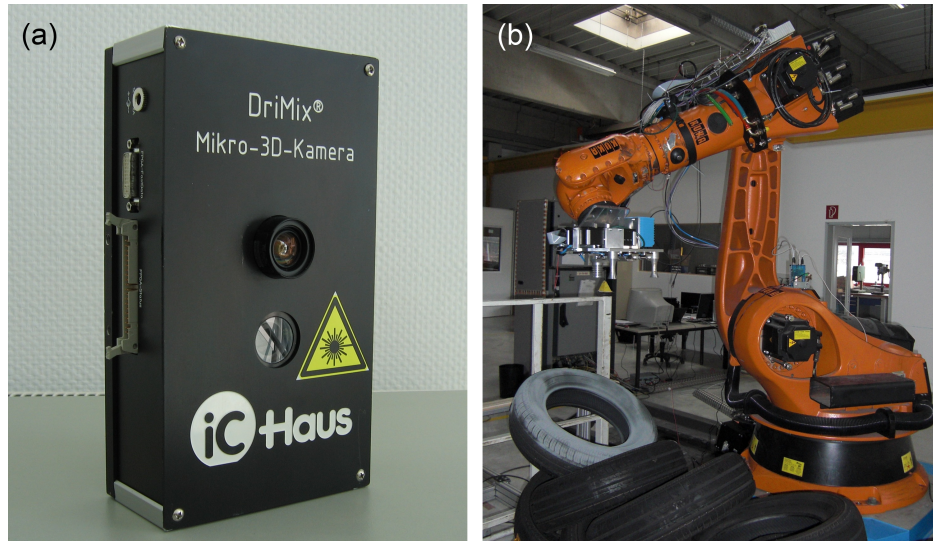


**Figure 3.17: DriMix Micro-3D-Camera and its application** - (a) DriMix camera with metallic housing © iC-Haus; (b) An exemplary application of DriMix camera in industrial robotics at AROTEC Automation und Robotik GmbH [BMBF3DKM].

### 3.2.1.1 DriMix Sensor Specification

The fundamental of DriMix Micro-3D-Camera is an optical sensor equipped with double-integrator pixels with drift-field-mixing concept. When Lambertian surface is assumed here, which means the apparent brightness of object surface to an observer is the same regardless of the observer's angle of view, the double-integrator pixel in the sensor array is capable of perceiving reflectance intensity of the object. Based on that the distance of object can be calculated with ToF principle. A Patent (No. WO2005036647 A1 [HERZ05]) for such type of optical sensor is filed by iC-Haus.

The DriMix sensor array with  $80(\text{column}) \times 60(\text{row})$  pixels is built upon drift-field-mixing concept as shown in Fig. 3.18. Each pixel is equipped with two integrator capacitors being able to perform multiple integration of the photocurrent generated from the sensed pulse-modulated (laser) light beam. The fast integration can reach up to 50 image captures pro second. There is LVDS interface for digital interconnection between optical sensor array and modulated light source. SPI interface is available for on-board communication link for control logic and data transmission.

Determination of the measured distance/depth depends on a set of system parameters. A summary of the DriMix system parameters in the distance calculation model

### 3. ADVANCED EMBEDDED VISION SYSTEMS FOR ADAS

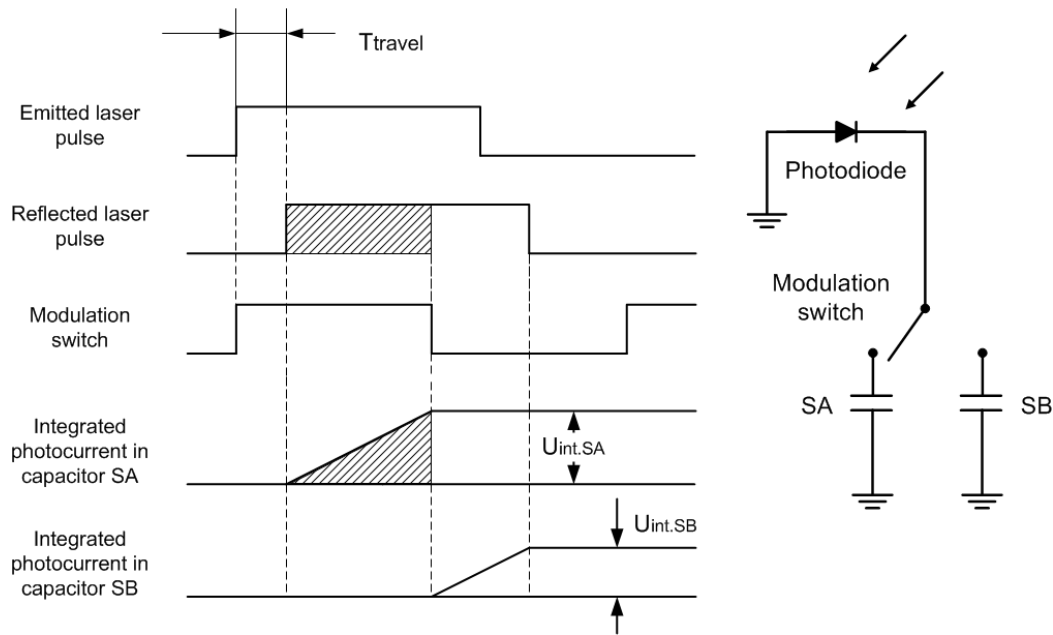


**Figure 3.18: DriMix (drift-field-mixing) concept** - Example of the drift-field-mixing concept with a double-capacitor setup.

is given as follows.

- $T_{WIDTH}$ : Pulse duration of emitted photocurrent (laser)
- $T_{STARTADR}$ : Time shift between emitted photocurrent and drift-voltage ( $V_{MODH}$ )
- $T_{MOD}$ : Period of modulation voltage (drift-voltage)
- $f_{MOD}$ : Frequency of modulation voltage (drift-voltage)
- $T_{travel}$ : Time-of-Flight for the pulsed laser traveling from light source to photo detector
- $T_{distance}$ : Time-of-Flight for the pulsed laser traveling from light source to object
- $T_{int.SA}$ : Integration time of SA capacitor
- $T_{int.SB}$ : Integration time of SB capacitor
- $U_{int.SA}$ : Integrated voltage of SA capacitor
- $U_{int.SB}$ : Integrated voltage of SB capacitor



## 3.2 Investigated Depth Cameras in the Project

---

- $d$ : Distance between photodetector and measuring object
- $c$ : Velocity of light

As per DriMix sensor specification (TS006 Specification A0.6) the dynamic range of configurable system parameters are specified as follows.

- $0 < f_{MOD} \leq 20$  MHz, i.e.,  $T_{MOD} \geq 50$  ns
- $0 \leq T_{WIDTH} < T_{MOD}$  with  $WIDTH = 0, 1, 2, \dots, 63$
- $0 < T_{STARTADR} < T_{MOD}$  with  $STARTADR = 0, 1, 2, \dots, 63$

Depending on the above mentioned parameter settings there are four cases in DriMix depth calculation model being addressed in Fig. 3.19, Fig. 3.21, Fig. 3.22, Fig. 3.23 respectively.

The distance between the DriMix sensor and the measuring object can be calculated as follows

$$d = c \cdot T_{distance} = c \cdot \frac{T_{travel}}{2}. \quad (3.5)$$

When the falling edge of modulation voltage VMODH in square wave form lies in the reflected laser pulse, and the condition  $0 < (T_{STARTADR} + T_{travel}) < \frac{T_{MOD}}{2}$  is fulfilled, then Case 1 (Fig. 3.19) is addressed here. When the rising edge of modulation voltage VMODH in square wave form lies in the reflected laser pulse, and the condition  $\frac{T_{MOD}}{2} < (T_{STARTADR} + T_{travel}) < T_{MOD}$  is fulfilled, Case 2 (Fig. 3.21) is occurring. When the falling edge of modulation voltage VMODH in square wave form lies in the reflected laser pulse, and the condition  $T_{MOD} < (T_{STARTADR} + T_{travel}) < \frac{3}{2}T_{MOD}$  is fulfilled, Case 3 (Fig. 3.22) is observed. When the rising edge of modulation voltage VMODH in square wave form lies in the reflected laser pulse, and the condition  $\frac{3}{2}T_{MOD} < (T_{STARTADR} + T_{travel}) < 2T_{MOD}$  is fulfilled, Case 4 (Fig. 3.23) is discussed.

When  $T_{STARTADR} \in [0, T_{MOD}[$  (as per TS006 Specification A0.6) as depicted in Fig. 3.19 (**Case 1**) it has

$$T_{travel} = \frac{1}{2}T_{MOD} - T_{int.SA} - T_{STARTADR} \quad (3.6)$$

with  $T_{int.SA} \neq 0 \cap T_{int.SB} \neq 0, \quad 0 < (T_{STARTADR} + T_{travel}) < \frac{T_{MOD}}{2}$

and

$$T_{WIDTH} = T_{int.SA} + T_{int.SB}. \quad (3.7)$$

### 3. ADVANCED EMBEDDED VISION SYSTEMS FOR ADAS

---

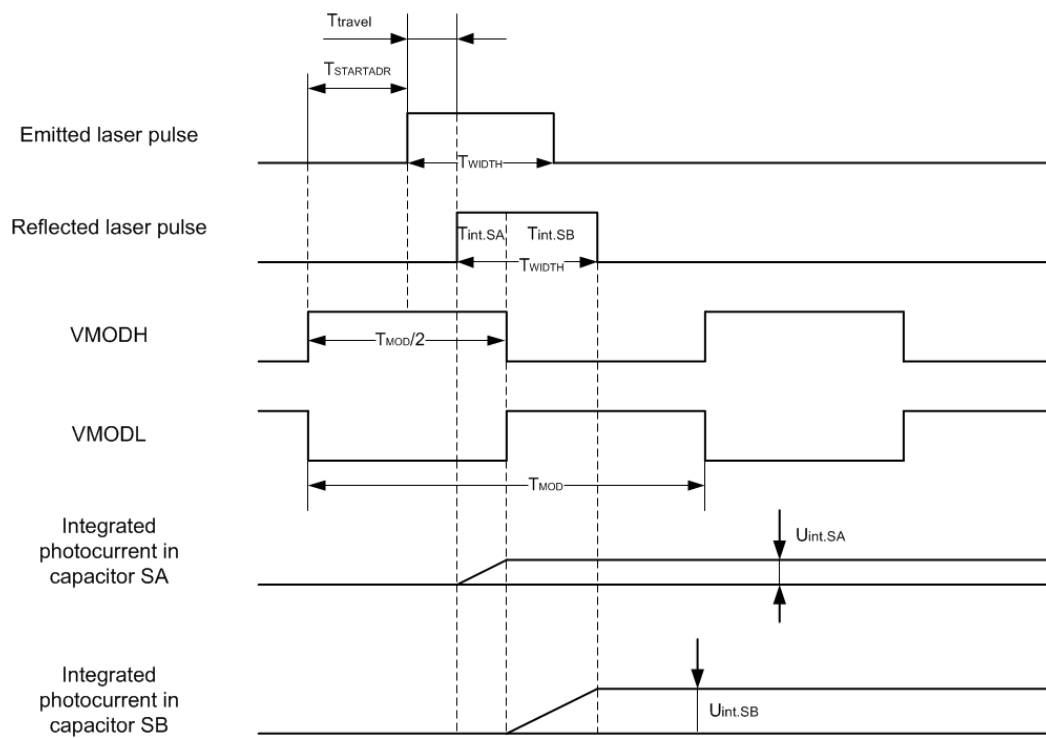


**Figure 3.19: DriMix measurement (Case 1)** - Example of timing diagram for single measurement Case 1.



### 3.2 Investigated Depth Cameras in the Project

---

With the same amount of capacity  $C$  of SA- and SB-capacitors it has

$$\frac{Q_{int.SA}}{Q_{int.SB}} = \frac{C \cdot U_{int.SA}}{C \cdot U_{int.SB}} = \frac{U_{int.SA}}{U_{int.SB}} \quad \text{with } U_{int.SB} \neq 0 \cap C \neq 0. \quad (3.8)$$

For photoelectric charge it has

$$Q = I \cdot T, \quad (3.9)$$

where  $Q$  is the die integrated photoelectric charge,  $I$  is the photocurrent, and  $T$  is the integration time. Because capacitor SA and SB are associated with the same photodiode in DriMix sensor, SA and SB have the same photocurrent  $I$ . From Eq. (3.9) it has

$$\frac{Q_{int.SA}}{Q_{int.SB}} = \frac{I \cdot T_{int.SA}}{I \cdot T_{int.SB}} = \frac{T_{int.SA}}{T_{int.SB}} \quad \text{with } T_{int.SB} \neq 0 \cap I \neq 0. \quad (3.10)$$

Eq. (3.8) and Eq. (3.10) imply

$$\frac{T_{int.SA}}{T_{int.SB}} = \frac{Q_{int.SA}}{Q_{int.SB}} = \frac{U_{int.SA}}{U_{int.SB}} \quad \text{with } U_{int.SB} \neq 0 \cap T_{int.SB} \neq 0. \quad (3.11)$$

From Eq. (3.11) it has

$$\frac{T_{int.SA}}{T_{int.SA} + T_{int.SB}} = \frac{U_{int.SA}}{U_{int.SA} + U_{int.SB}} \quad \text{with } T_{int.SA} \neq 0 \cap T_{int.SB} \neq 0. \quad (3.12)$$

Applying Eq. (3.7) in Eq. (3.12) results

$$\frac{T_{int.SA}}{T_{WIDTH}} = \frac{U_{int.SA}}{U_{int.SA} + U_{int.SB}} \quad \text{with } T_{WIDTH} \neq 0. \quad (3.13)$$

From Eq. (3.13) it has

$$T_{int.SA} = \frac{U_{int.SA}}{U_{int.SA} + U_{int.SB}} \cdot T_{WIDTH}. \quad (3.14)$$

Applying Eq. (3.14) in Eq. (3.6) results

$$\begin{aligned} T_{travel} &= \frac{1}{2} T_{MOD} - \frac{U_{int.SA}}{U_{int.SA} + U_{int.SB}} \cdot T_{WIDTH} - T_{STARTADR} \\ &\text{with } U_{int.SA} \neq 0 \cap U_{int.SB} \neq 0, \\ T_{STARTADR} &\in [0, T_{MOD}], \quad T_{WIDTH} \in [0, T_{MOD}], \\ 0 &< (T_{STARTADR} + T_{travel}) < \frac{T_{MOD}}{2}. \end{aligned} \quad (3.15)$$

The parameter  $T_{WIDTH}$  can be preliminarily configured within  $[0, T_{MOD}[$ . However, this parameter shall be further constrained, otherwise the so-called multiple integration will occur when  $\frac{T_{MOD}}{2} \leq T_{WIDTH} < T_{MOD}$  and Eq. (3.15) is not valid anymore.

### 3. ADVANCED EMBEDDED VISION SYSTEMS FOR ADAS

---

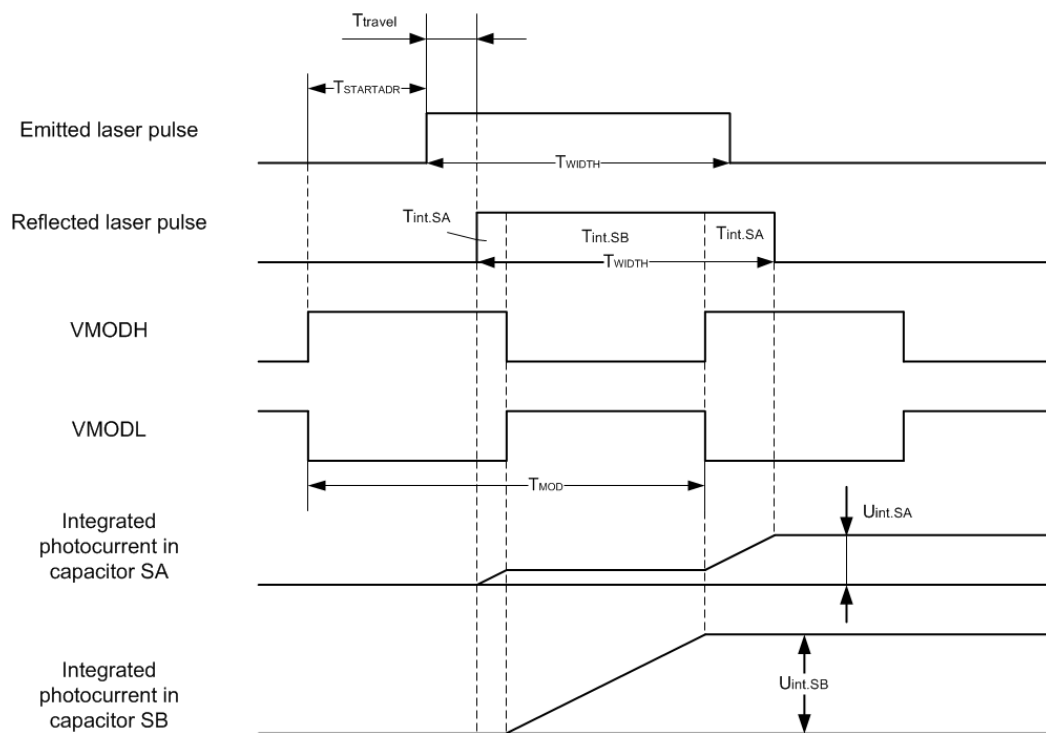


**Figure 3.20: DriMix measurement (multiple integration)** - Example of timing diagram for multiple integration.

### 3.2 Investigated Depth Cameras in the Project

An example for the multiple integration in this case is illustrated in Fig. 3.20. In addition,  $T_{WIDTH} = 0$  implies that there is no laser pulse emitted. In order to determine  $T_{travel}$  in unambiguous way the range of  $T_{WIDTH}$  shall be tuned as  $0 < T_{WIDTH} \leq \frac{T_{MOD}}{2}$ , i.e.,  $T_{WIDTH} \in ]0, \frac{T_{MOD}}{2}]$ . In the end  $T_{travel}$  of Case 1 can be derived as follows

$$\begin{aligned}
 T_{travel}^{Case1} &= \frac{1}{2}T_{MOD} - \frac{U_{int.SA}}{U_{int.SA} + U_{int.SB}} \cdot T_{WIDTH} - T_{STARTADR} \\
 &\text{with } U_{int.SA} \neq 0 \cap U_{int.SB} \neq 0, \\
 T_{STARTADR} &\in [0, T_{MOD}[, \quad T_{WIDTH} \in ]0, \frac{T_{MOD}}{2}], \\
 0 < (T_{STARTADR} + T_{travel}) &< \frac{T_{MOD}}{2}.
 \end{aligned} \tag{3.16}$$

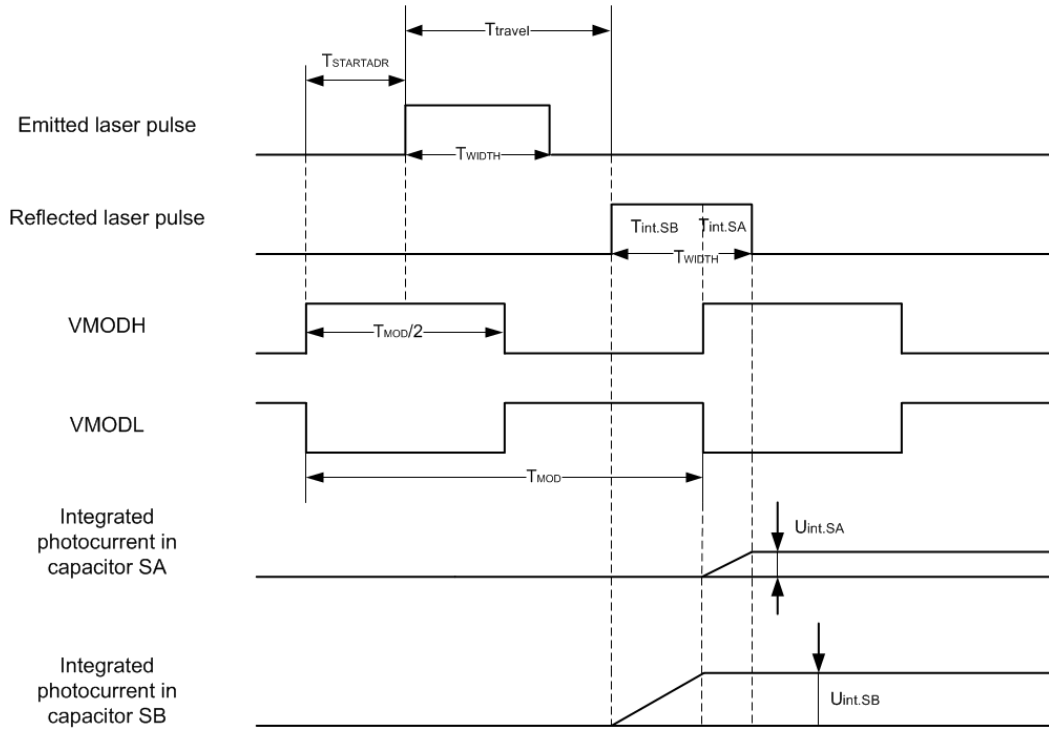


**Figure 3.21: DriMix measurement (Case 2)** - Example of timing diagram for single measurement Case 2.

When  $T_{STARTADR} \in [0, T_{MOD}[$  (as per TS006 Specification A0.6) as depicted in Fig. 3.21 (**Case 2**) it has

$$\begin{aligned}
 T_{travel} &= T_{MOD} - T_{int.SB} - T_{STARTADR} \\
 &\text{with } T_{int.SA} \neq 0 \cap T_{int.SB} \neq 0, \quad \frac{T_{MOD}}{2} < (T_{STARTADR} + T_{travel}) < T_{MOD}.
 \end{aligned} \tag{3.17}$$

### 3. ADVANCED EMBEDDED VISION SYSTEMS FOR ADAS

---

Eq. (3.7) to Eq. (3.10) hold true in Case 2 as well and 3.11 can be transformed to

$$\frac{T_{int.SB}}{T_{int.SA}} = \frac{Q_{int.SB}}{Q_{int.SA}} = \frac{U_{int.SB}}{U_{int.SA}} \quad \text{with} \quad U_{int.SA} \neq 0 \cap T_{int.SA} \neq 0. \quad (3.18)$$

From Eq. (3.11) it has

$$\frac{T_{int.SB}}{T_{int.SA} + T_{int.SB}} = \frac{U_{int.SB}}{U_{int.SA} + U_{int.SB}} \quad \text{with} \quad T_{int.SA} \neq 0 \cap T_{int.SB} \neq 0. \quad (3.19)$$

Applying Eq. (3.7) in Eq. (3.19) results

$$\frac{T_{int.SB}}{T_{WIDTH}} = \frac{U_{int.SB}}{U_{int.SA} + U_{int.SB}} \quad \text{with} \quad T_{WIDTH} \neq 0. \quad (3.20)$$

From Eq. (3.20) it has

$$T_{int.SB} = \frac{U_{int.SB}}{U_{int.SA} + U_{int.SB}} \cdot T_{WIDTH}. \quad (3.21)$$

With  $0 < T_{WIDTH} \leq \frac{T_{MOD}}{2}$  Eq. (3.21) is applied in Eq. (3.17) and results

$$\begin{aligned} T_{travel}^{Case2} &= T_{MOD} - \frac{U_{int.SB}}{U_{int.SA} + U_{int.SB}} \cdot T_{WIDTH} - T_{STARTADR} \\ \text{with} \quad U_{int.SA} &\neq 0 \cap U_{int.SB} \neq 0, \\ T_{STARTADR} &\in [0, T_{MOD}[, \quad T_{WIDTH} \in ]0, \frac{T_{MOD}}{2}], \\ \frac{T_{MOD}}{2} &< (T_{STARTADR} + T_{travel}) < T_{MOD}. \end{aligned} \quad (3.22)$$

Analogous to Case 1 it holds true when  $T_{STARTADR} \in [0, T_{MOD}[$  (as per TS006 Specification A0.6) as depicted in Fig. 3.22 (**Case 3**),

$$\begin{aligned} T_{travel} &= \frac{3}{2}T_{MOD} - T_{int.SA} - T_{STARTADR} \\ \text{with} \quad T_{int.SA} &\neq 0 \cap T_{int.SB} \neq 0, \quad T_{MOD} \leq (T_{STARTADR} + T_{travel}) < \frac{3}{2}T_{MOD}. \end{aligned} \quad (3.23)$$

Eq. (3.7) to Eq. (3.14) hold true in Case 3 as well and applying Eq. (3.14) in Eq. (3.23) results

$$\begin{aligned} T_{travel}^{Case3} &= \frac{3}{2}T_{MOD} - \frac{U_{int.SA}}{U_{int.SA} + U_{int.SB}} \cdot T_{WIDTH} - T_{STARTADR} \\ \text{with} \quad U_{int.SA} &\neq 0 \cap U_{int.SB} \neq 0, \\ T_{STARTADR} &\in [0, T_{MOD}[, \quad T_{WIDTH} \in ]0, \frac{T_{MOD}}{2}], \\ T_{MOD} &< (T_{STARTADR} + T_{travel}) < \frac{3}{2}T_{MOD}. \end{aligned} \quad (3.24)$$

### 3.2 Investigated Depth Cameras in the Project

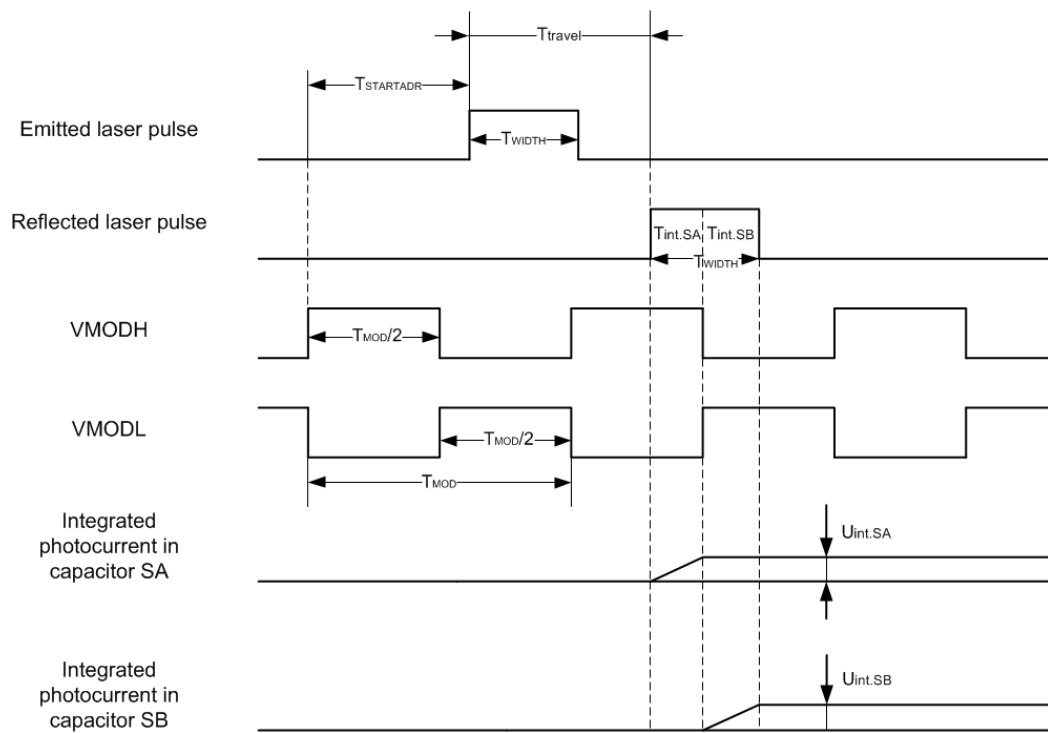


**Figure 3.22: DriMix measurement (Case 3)** - Example of timing diagram for single measurement Case 3.

### 3. ADVANCED EMBEDDED VISION SYSTEMS FOR ADAS

Analogous to Case 2 it holds true when  $T_{STARTADR} \in [0, T_{MOD}[$  (as per TS006 Specification A0.6) as depicted in Fig. 3.23 (**Case 4**),

$$T_{travel} = 2T_{MOD} - T_{int.SB} - T_{STARTADR}$$

$$\text{with } T_{int.SA} \neq 0 \cap T_{int.SB} \neq 0, \quad \frac{3}{2}T_{MOD} \leq (T_{STARTADR} + T_{travel}) < 2T_{MOD}. \quad (3.25)$$

Eq. (3.7) to Eq. (3.11) and Eq. (3.18) to Eq. (3.21) hold true in Case 4 as well, and applying Eq. (3.14) in Eq. (3.25) results

$$T_{travel}^{Case4} = 2T_{MOD} - \frac{U_{int.SB}}{U_{int.SA} + U_{int.SB}} \cdot T_{WIDTH} - T_{STARTADR}$$

$$\text{with } U_{int.SA} \neq 0 \cap U_{int.SB} \neq 0,$$

$$T_{STARTADR} \in [0, T_{MOD}[, \quad T_{WIDTH} \in ]0, \frac{T_{MOD}}{2}], \quad (3.26)$$

$$\frac{3}{2}T_{MOD} < (T_{STARTADR} + T_{travel}) < 2T_{MOD}.$$

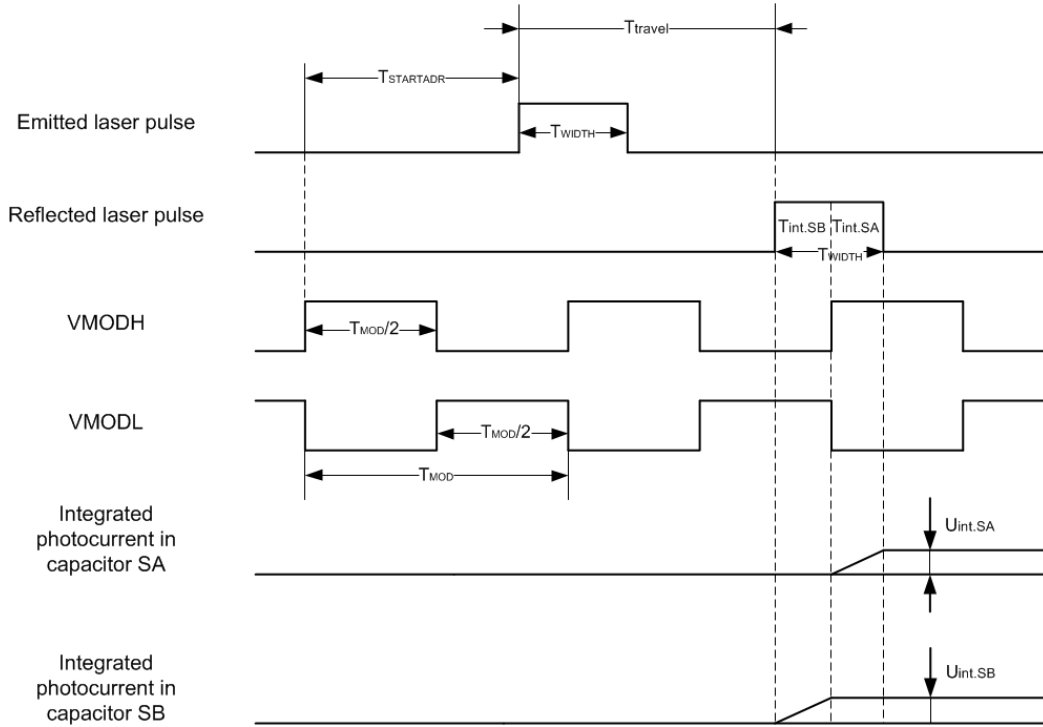


**Figure 3.23: DriMix measurement (Case 4)** - Example of timing diagram for single measurement Case 4.

So far the single measurement of distance has been discussed within two periods of drift voltage. In fact  $T_{travel}$  can be extended with one or multiple periods of drift voltage

### 3.2 Investigated Depth Cameras in the Project

---

without changing  $U_{int.SA}$  and  $U_{int.SB}$ , which causes the so-called *aliasing* problem (range ambiguity). In special case as depicted in Fig. 3.24 the distances being calculated from Case 1 and Case 3 have the following relationship

$$T_{travel}^{Case3} = T_{travel}^{Case1} + T_{MOD}$$

$$\text{with } T_{int.SA} \neq 0 \cap T_{int.SB} \neq 0, \quad T_{MOD} < (T_{STARTADR} + T_{travel}) < \frac{3}{2}T_{MOD}. \quad (3.27)$$

In general  $T_{travel}$  in the above mentioned four cases can be interpreted as follows

$$T_{travel}^{Case*} = T_{travel}^{Case*} + k \cdot T_{MOD} \quad (3.28)$$

$$\text{with } k = 0, 1, 2, \dots$$

Case\* in Eq. (3.28) denotes Case 1, Case 2, Case 3 or Case 4.

In order to avoid aliasing problem the distance measurement shall be performed with different modulation frequencies of drift voltage ( $f_{MOD}$ ). Alternatively the measuring distance can be determined from the two aliasing values by using priori knowledge for the scene, e.g., the maximum distance of measuring object away from the DriMix sensor.

As mentioned previously  $T_{travel}$  can be computed as per Eq. (3.16), Eq. (3.22), Eq. (3.24), Eq. (3.26) for four different cases if the following conditions are fulfilled:  $U_{int.SA} \neq 0 \cap U_{int.SB} \neq 0$ ,  $T_{STARTADR} \in [0, T_{MOD}[$ , and  $T_{WIDTH} \in ]0, \frac{T_{MOD}}{2}]$ . Afterwards the measuring distance can be determined according to Eq. (3.5).

To determine the maximum measurement range of the DriMix sensor the dynamic range of  $T_{travel}^{Case1}$ ,  $T_{travel}^{Case2}$ ,  $T_{travel}^{Case3}$ ,  $T_{travel}^{Case4}$  are investigated. As per Eq. (3.16), Eq. (3.22), Eq. (3.24), Eq. (3.26) it can be identified:  $T_{travel}^{Case1} \in [0, \frac{T_{MOD}}{2}[$ ,  $T_{travel}^{Case2} \in [\frac{T_{MOD}}{2}, T_{MOD}[$ ,  $T_{travel}^{Case3} \in [T_{MOD}, \frac{3}{2}T_{MOD}[$ ,  $T_{travel}^{Case4} \in [\frac{3}{2}T_{MOD}, 2T_{MOD}[$ . To sum up it has

$$0 \leq T_{travel} \leq 2T_{MOD}. \quad (3.29)$$

By applying Eq. (3.29) in Eq. (3.5) the maximum measurement range of the DriMix sensor can be determined under conditions  $T_{STARTADR} \in [0, T_{MOD}[$  and  $T_{WIDTH} \in ]0, \frac{T_{MOD}}{2}]$  as follows

$$d = c \cdot \frac{T_{travel_{max}}}{2} = c \cdot \frac{2T_{MOD}}{2} = c \cdot T_{MOD} = \frac{c}{f_{MOD}}. \quad (3.30)$$

The charge integration of the background light is due to multiple measurements and by the four-phase integration mostly compensated and therefore does not come

### 3. ADVANCED EMBEDDED VISION SYSTEMS FOR ADAS

into the derived computation formula. The systematic delay of the electronic circuits and from the laser driver is for the time being, together with the adjustable laser pulse delay as  $T_{STARTADR}$  considered.

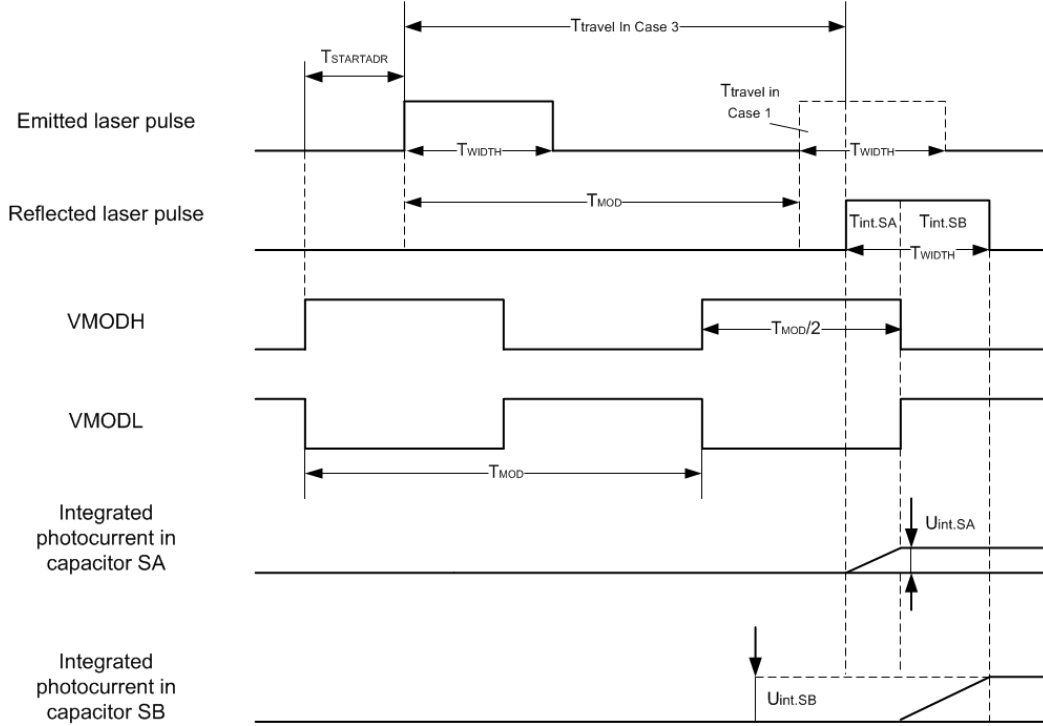


**Figure 3.24: DriMix measurement (aliasing)** - Example of timing diagram for aliasing issue between Case 1 and Case 3.

#### 3.2.1.2 DriMix Camera System Evaluation

First evaluations to validate the calculation model of distance measurement using DriMix camera system are described in this section.

The charge separation of photocurrent from SA and SB integration capacitors is considered in the first place. After removal of DC offset (caused by background illumination) the maximum voltage difference of SA and SB (peak-to-peak) remains almost constant, before and after the intersection of the SA and SB curves. However, the further the object is away from the camera, the lower is the  $|SA - SB|$  due to the attenuation of reflected light intensity along with a increased distance. To achieve better charge separation the system parameters  $T_{WIDTH}$  and  $f_{MOD}$  should be properly



### 3.2 Investigated Depth Cameras in the Project

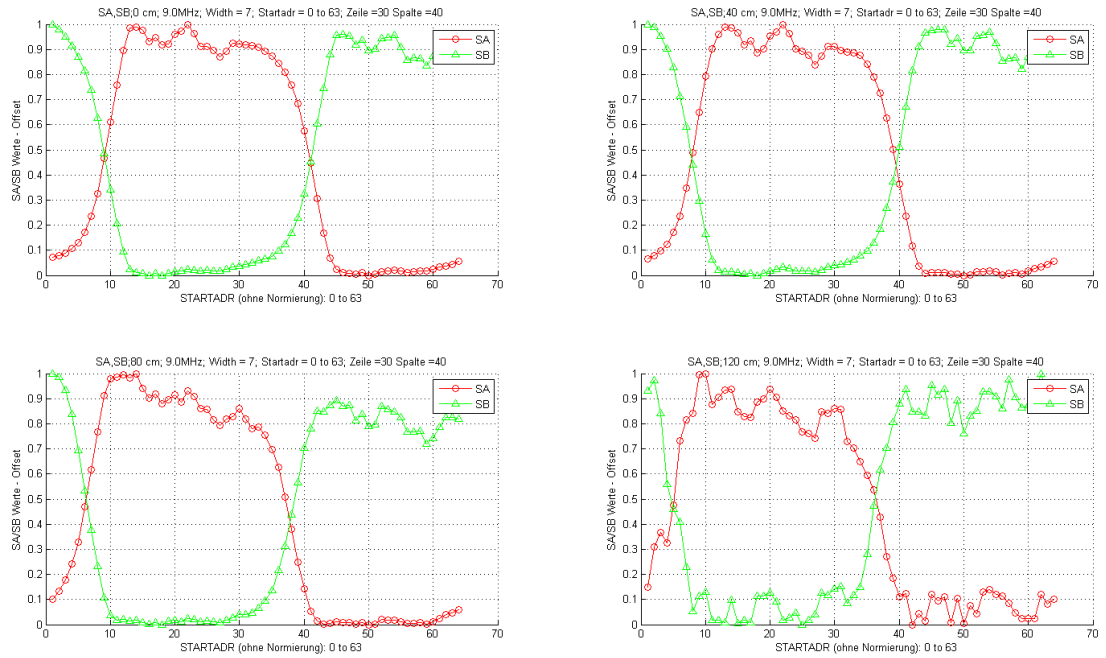


**Figure 3.25: DriMix Evaluation (normalization)** - Normalized SA/SB values of the sensor pixel on row 30, column 40, left to right and top to bottom: distance between sensor array and object, 0 cm, 40 cm, 80 cm, 120 cm,  $WIDTH = 7$ ,  $f_{MOD} = 9$  MHz.

### 3. ADVANCED EMBEDDED VISION SYSTEMS FOR ADAS

---

adjusted in accordance with the depth range of the measuring object. In the DriMix camera evaluation test (see Fig. 3.30), the modulation frequency of drift-voltage ( $f_{MOD}$ ) was chosen to be 9 MHz. Using Eq. (3.30) the maximum range can be determined in this case as 33 m. The distance of measuring object to DriMix is less than 33 m, thus no aliasing issue to be considered. The parameter  $WIDTH$  was set to 7, i.e.,  $\frac{7}{64}$  of  $T_{MOD}$ , thus no multiple integration (see Fig. 3.20) was observed, and Eq. (3.16) can be used to estimate the time of flight and calculate the distance here.

For one pixel of the sensor array, the integrated voltage of SA/SB capacitor, here in the form of 12-bit ADC output, is normalized as follows,

$$\begin{aligned} U'_{int.SA} &= U'_{int.SA} - Offset_{DC}, \\ U_{int.SA} &= \frac{U'_{int.SA} - \min(U'_{int.SA})}{|\max(U'_{int.SA}) - \min(U'_{int.SA})|}, \end{aligned} \quad (3.31)$$

where  $U'_{int.SA}$  is the raw data representing the voltage of SA capacitor,  $\max(U'_{int.SA})$  and  $\min(U'_{int.SA})$  give the maximum and minimum integrated voltage on SA capacitor of the pixel within the measurement window. The voltage value normalization is applicable for SB capacitor of the same pixel as well. An example of the normalized SA/SB values of a single pixel on the DriMix sensor can be found in Fig. 3.25.

Using normalized SA and SB values the measured distance can be computed. As shown in Fig. 3.26, in Case 1, four different distances measured by the same DriMix sensor pixel at row 30, column 40, are represented as four parallel running horizontal lines with constant vertical spacing where  $STARTADR = 34$  to 44 (see Fig. 3.27).

The depth measurements of DriMix sensor pixel can be evaluated using MSE (Mean Square Error) of the computed depth differences ( $\Delta d$ ), so that the inherent offset of depth measurements can be eliminated. In Fig. 3.25 it should be noted that the cross points of SA- and SB-curve are used to identify the linear section of SA, where Eq. (3.16) can be used to compute the measured distance.  $\Delta d1$  are depth differences of the computed values based on the sample point right after the second cross point of SA- and SB-curve;  $\Delta d2$  are depth differences of the computed values based on the sample point right before the second cross point of SA- and SB-curve;  $\Delta d3$  are mean values of the respective  $\Delta d1$  and  $\Delta d2$ . The measurement results of DriMix sensor pixel at row 30, column 40, are summarized in Table 3.1.

### 3.2 Investigated Depth Cameras in the Project

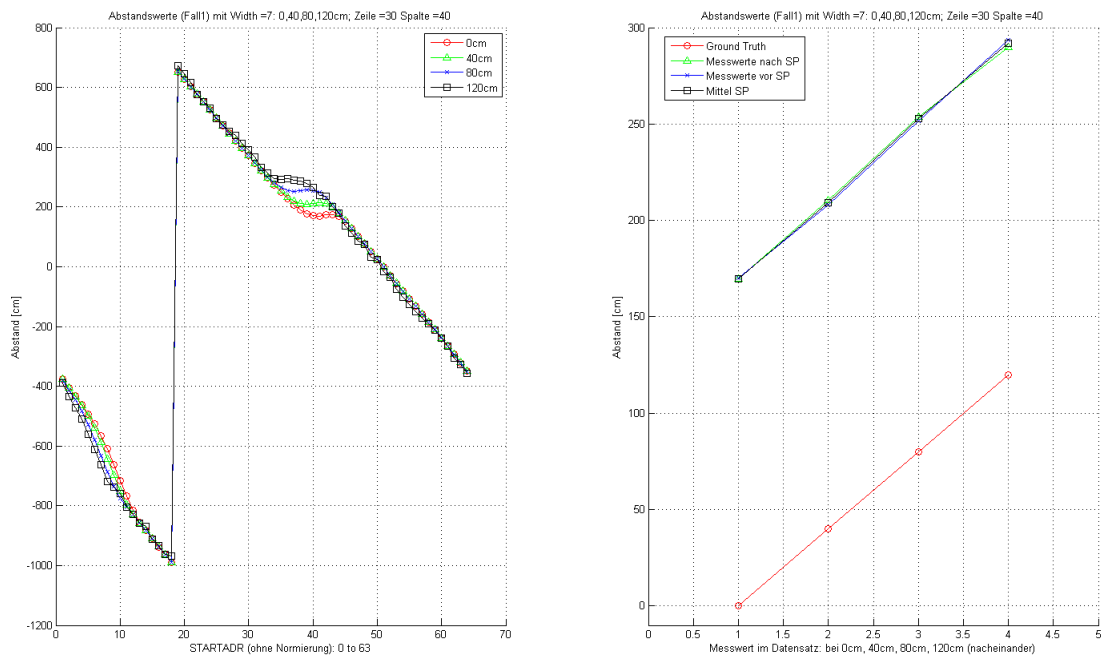


**Figure 3.26: DriMix Evaluation (distance calculation)** - The distance calculation with normalized SA/SB values in Case 1 (refer to Eq. (3.16)) for distance 0 cm, 40 cm, 80 cm, 120 cm;  $WIDTH = 7$ ;  $f_{MOD} = 9$  MHz. Left: distance computation based on *STARTADR* values; right: computed linear distances of four measuring objects with constant offset 152 cm.

### 3. ADVANCED EMBEDDED VISION SYSTEMS FOR ADAS

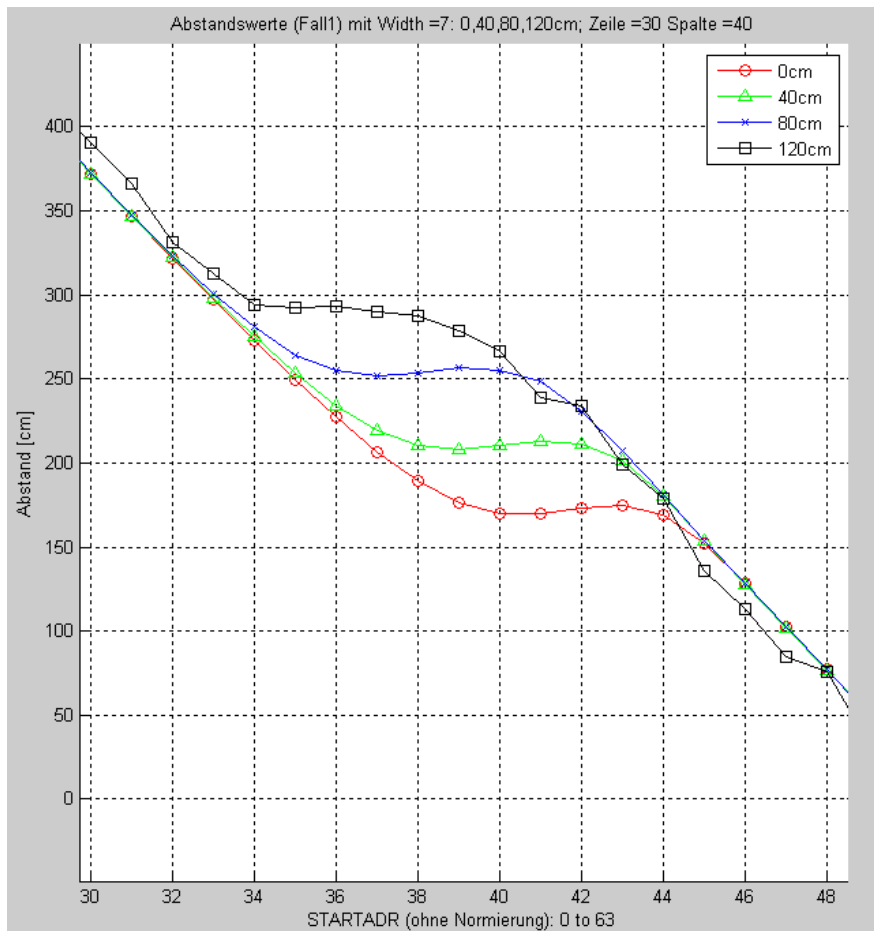


Figure 3.27: DriMix Evaluation (distance calculation with details) - The flat watershed on the curve in Fig. 3.26 left,  $WIDTH = 7$ .

### 3.2 Investigated Depth Cameras in the Project

**Table 3.1:** Depth measurement evaluation of a single DriMix sensor pixel

$\Delta d_{GT}$	True Value in [cm]	$\Delta d1$ in [cm]	$\Delta d2$ in [cm]	$\Delta d3$ in [cm]
40cm - 0	40	40.5577	38.0126	39.2851
80cm - 0	80	83.8107	81.6946	82.7526
120cm - 0	120	120.0040	123.6167	121.8104
80cm - 40cm	40	43.2530	43.6820	43.4675
120cm - 40cm	80	79.4463	85.6042	82.5253
120cm - 80cm	40	36.1933	41.9221	39.0577
MSE in [cm <sup>2</sup> ]	-	6.7019	11.4269	5.1090

The measurement flow of the developed DriMix camera system prototype (see Fig. 3.28) is designed and validated in the experiments. The current measuring frame rate is up to 10 fps with the designed measurement flow.

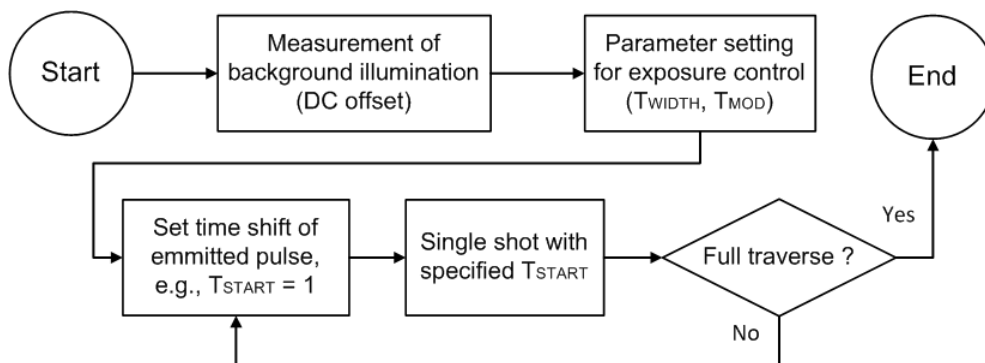


**Figure 3.28:** DriMix measurement flow - The software-controlled depth measurement flow.

Compared to other state-of-the-art (ToF) depth cameras (refer to Table 3.2) DriMix camera system does not bring superior measurement results with respect to depth resolution (accuracy), frame rate, and operation range. The following aspects should be considered to improve the DriMix camera system.

- Firstly, the fill factor of DriMix sensor pixel (currently < 30%) can be increased to improve the SNR.
- Additive record maneuver, i.e., a single-pass of the measurement flow (see Fig. 3.28), with elevated magnitude of  $T_{WIDTH}$  should be taken while maintaining both SA,

### 3. ADVANCED EMBEDDED VISION SYSTEMS FOR ADAS

SB values within the dynamic range, so that sensor pixels can collect more photons during exposure.

- In addition, aiming to improve the (depth) frame rate and overall camera performance, the measurement flow described in Fig. 3.28, which is currently handled in the host application, can be further implemented and integrated in the sensor/camera in terms of firmware, especially, for the exposure control process. The repetitive record maneuver can be realized in the camera firmware, which can be re-programmed afterwards if required.
- Last but not least, for depth image pre-processing, the outliers on the SA/SB-curves can be removed by applying linear regression. However, it requires special care to smartly "locate" the intersection interval of SA and SB curves, otherwise the results deteriorate dramatically when non-intersection record samples are involved. Thus, linear regression may therefore only be applied in the vicinity of the cross point of SA and SB.

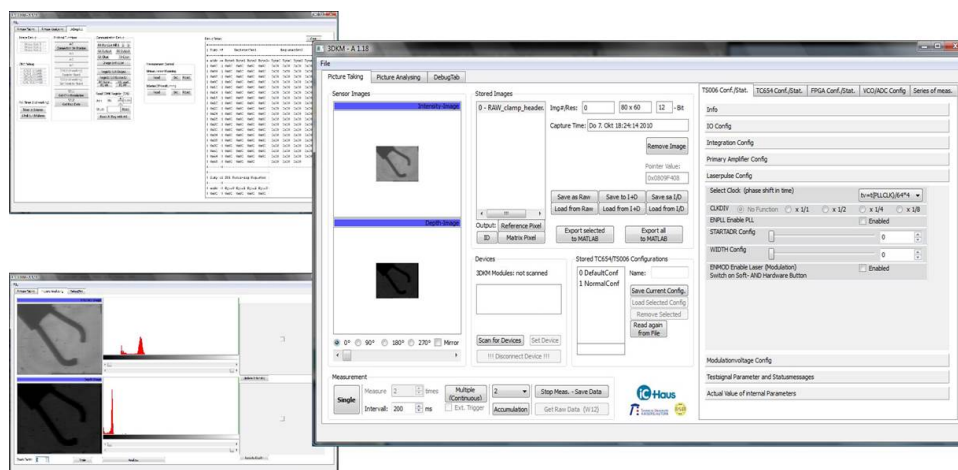


**Figure 3.29: DrIMix host application** - The PC-based host application features a customized user interface for the modulation control of light pulses, exposure (time) control, and some basic post-processing functions such as histogram of grayscale image.

The PC-based back-end host application is demonstrated in Fig. 3.29, which was developed by Benjamin Lutgen in the frame of 3DKM project. The host application

## 3.2 Investigated Depth Cameras in the Project

issues commands that afterwards are processed by the FPGA and expansion board, and communicated to the camera board, so as to manage the modulation control of light pulses, exposure (time) control, and data transmission control. In addition, some basic post-processing functions such as computation of histogram from grayscale image are realized in the host application.

Fig. 3.30 shows the test environment of the DriMix camera system. The validation test of the DriMix sensor was conducted in the frame of the 3DKM project, and more details can be found in Appendix.

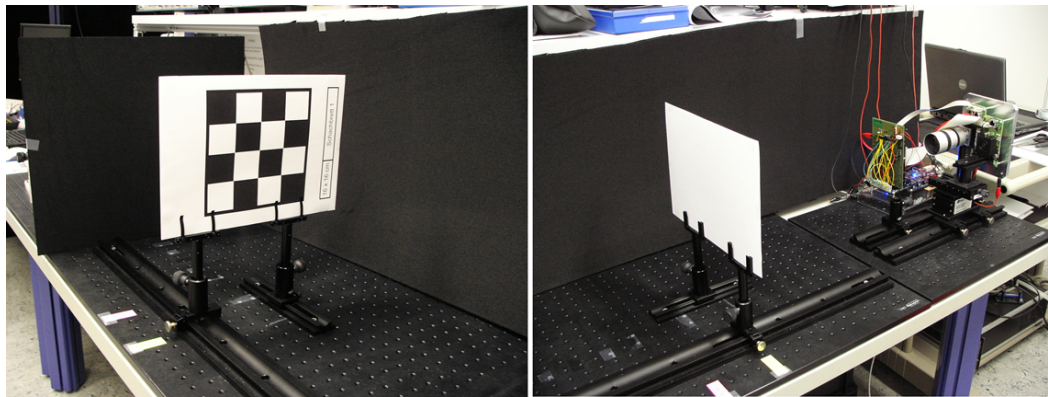


**Figure 3.30: DriMix validation test** - Test on camera system in the laboratory of iC-Haus GmbH.

### 3.2.2 Microsoft Kinect: Commodity IR Depth Camera

Microsoft launched in 2010 a new depth camera – Kinect for its Xbox 360 video game platform [KinectV1], hereinafter referred to as "Kinect V1 sensor". Similar to ToF depth cameras, Kinect has dual image output, i.e., depth and color/intensity images, which are pixel-aligned through a so-called *Registration* procedure. Depth measurement of Kinect V1 sensor is based on active IR Light Coding<sup>TM</sup> technology of PrimeSense which is claimed to be immune to ambient light [PrimeSense]. As mentioned in Section 3.1.2.2 it uses a static spatially encoded IR pattern (scattered points) projected onto the scene. The built-in camera captures an image of the scene and decodes the result from the projected pixels.

The hardware system of Kinect V1 sensor consisting of optical sensor electronics including depth image CMOS and color image CMOS, the associated IR light source,

### 3. ADVANCED EMBEDDED VISION SYSTEMS FOR ADAS

audio sensor array and microphones, flash memory, control logic (SoC), and communication interface, was developed based on PrimeSensor product (see Fig 3.31) of PrimeSense company (acquired by Microsoft in 2010).

Along with audio signal output Kinect V1 sensor can provide different types of image output as follows,

- Intensity and depth image (ID) output,
- Color and depth image (RGBD) output,
- Point cloud (with 3D coordinates) output,

where image output (ID or RGBD) can be provided at video frame rate, and point cloud output is optimized for applications such as robot control.

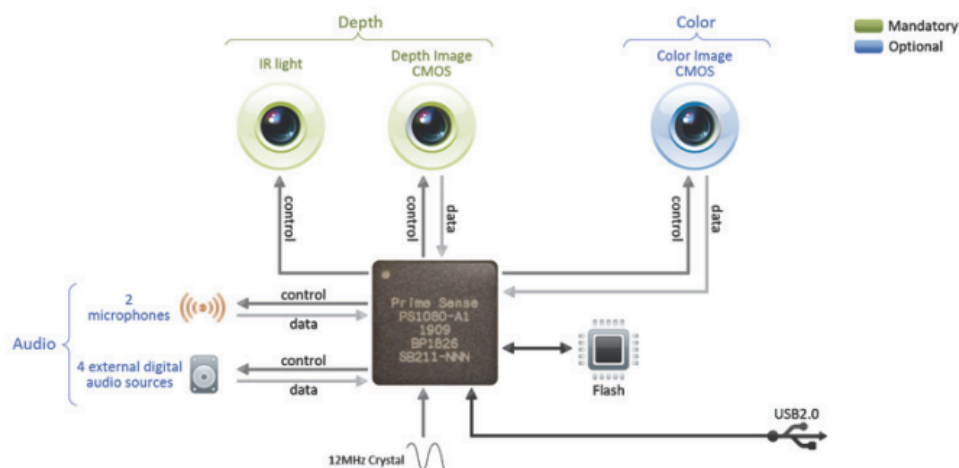


**Figure 3.31: PrimeSensor** - System block diagram [PrimeSense].

There are Kinect V1 sensors for different hardware platforms such as Xbox 360 game console and Windows PC with the following specifications:

- Spatial resolution (h x v): 640x480 (RGB) 640x480 (Depth)
- Depth accuracy: 1cm
- Operation range: 0.8m to 3.5m
- Illumination type: near infrared (NIR 830 nm).



### 3.2 Investigated Depth Cameras in the Project

The second generation of Kinect sensor hardware was released together with Xbox One game console in late 2013 – Kinect for Xbox One, hereinafter referred to as "Kinect V2 sensor". Compared to the structured-light based Kinect V1 sensor, the new ToF based Kinect V2 sensor provides higher resolution in both depth and color images, higher precision in motion sensing, and does not suffer from shadowing effects.

There are rich software development resources with regard to sensor drivers, tools, APIs, as well as open source applications. In particular, Kinect for Windows software development kit (SDK v1.8/v2.0) contains sensor device interfaces, code samples, and comprehensive guidelines to simplify the development of applications for commercial deployment. For instance, the *Kinect Identity* technology developed by Microsoft Research uses three visual cues to recognize different users: the faces and heights of users as well as the colors of their clothing. Robust face recognition is the key component of Kinect Identity [CYTS10]. In this approach a new unsupervised learning-based encoding method for salient facial components is introduced. Combined with a pose-adaptive matching technique the Kinect based face recognition is capable of compensating facial pose variation in real-life scenarios. As proposed by OpenKinect community [OpenKinect10] the Kinect based user-recognition can be further improved with 3D body size and human voice information to realize enhanced biometric identification.

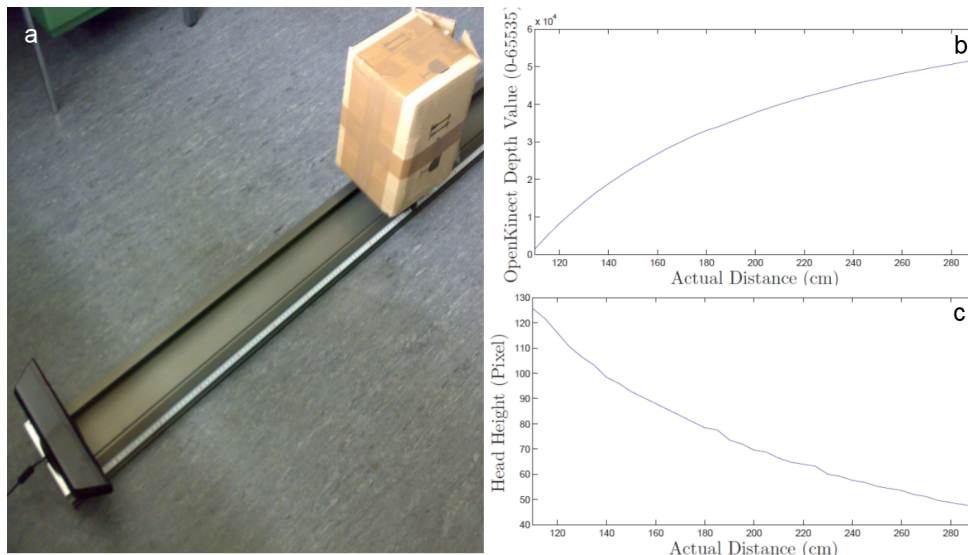


**Figure 3.32: Kinect V1 sensor calibration** - (a) Kinect sensor calibration on optical bench; (b) Kinect depth calibration results; (c) Kinect head height calibration results [LXK12].

### 3. ADVANCED EMBEDDED VISION SYSTEMS FOR ADAS

---

Before this work, the Kinect based researches in automotive applications are still scarce. In [KSB13] a 3D experimental framework for exploring driver's body activity using low-cost IR depth sensor (Kinect) has been proposed. The study was focused on driver's body movements when performing specific maneuver types such as lane changing and merging, and aiming to identify potential unsafe situations.

Driven by the advances in 3D embedded vision, in the frame of this research work, the Kinect V1 sensor was investigated for human-machine interactions [LXK11, LXK12], in particular for human-vehicle interfaces [LWK12], with the focus on head/eye localization and tracking. As an illustrative example, a Kinect calibration method intended for head tracking is depicted in Fig. 3.32.

### 3.3 Algorithms and Methods for 3D Embedded Vision

The following sections provide additional insights in useful algorithms and methods for 3D embedded vision and signal processing in ADAS.

#### 3.3.1 Single-/Multi-Person Eye Localization

Until recently, the application of 3D embedded vision systems in ADAS aimed at driver status monitoring is still scarce. On the hand the usage of such systems is constrained by environmental conditions, e.g., light conditions, vibrations, and the employment is limited by production cost. On the other hand, the traditional image/signal processing methods are facing challenges to deal with 3D objects, thus seek for adaptations and enhancements.

In [LXK11] a novel approach to IR depth camera based single-/multi-person eye localization is proposed for the use in human-machine interactions. The proposed algorithm is outlined in Fig. 3.33. After image denoising procedure with median filter, foreground object segmentation is performed on the input depth image to extract individual objects from the foreground. It should be highlighted that with additional depth information it is much easier to cut out the background and analyze the spatial relations among foreground objects. Contour analysis is applied on the detected object regions to find potential faces in the scene. Facial sub-images are extracted from the input intensity image based on the face region masks obtained from the previous stage. Using predefined template eye candidates are located and paired in group in the normalized

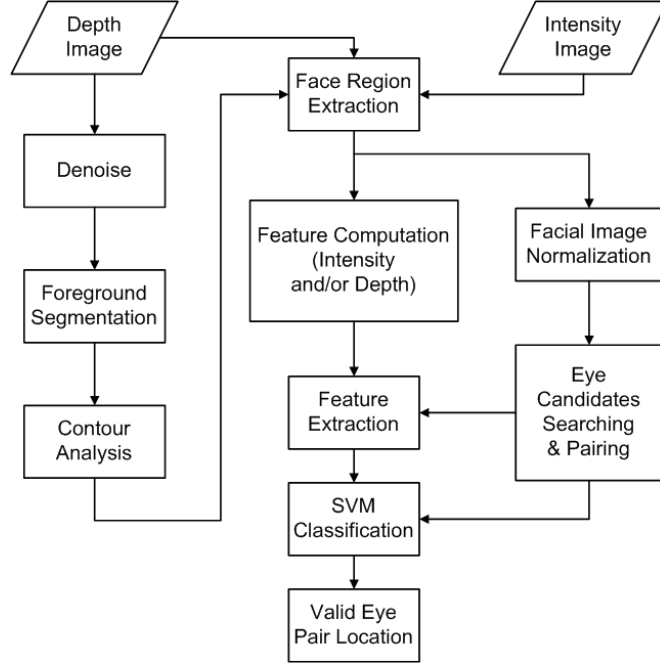


**Figure 3.33: Eye localization (algorithm)** - The processing pipeline of the proposed algorithm for single-/multi-person eye localization [LXK11].

face region. Afterwards, the geometric features of the eye pair candidates are extracted based on the extended eye template. Along with a supervised training procedure a support vector machine (SVM) is employed to classify the eye pair candidates.

It should be noted that the extracted facial sub-images have different scales depending on the distance between the user and camera. To apply the predefined template for eye candidates searching the face size normalization is required. Since the original image output of Kinect is with  $640 \times 480$  spatial resolution, the facial sub-images are normalized in the size of 60 by 50 pixels. The located eyes on the normalized facial sub-image can be mirrored back to the original image based on the scale factor as determined here.

A predefined eye template (see Fig. 3.34: left eye and right eye) is employed to search the left and right eye candidates in the obtained facial intensity image. The design of the eye template is based on the fact that the iris is darker than the surrounding sclera in the eye region. In addition, the template highlights the bilateral symmetry of a pair of eyes with respect to the pixel intensity. The implementation of the eye template is inspired by Monotonie-Operator [KZ89], Harris [HS88] and SUSAN [SB97] corner

### 3. ADVANCED EMBEDDED VISION SYSTEMS FOR ADAS

---

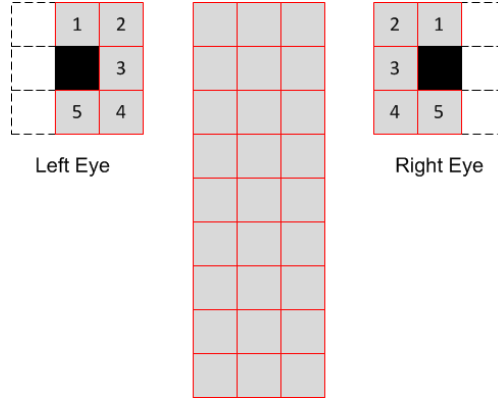


**Figure 3.34: Eye template** - The predefined left and right eye template (18 pixels/blocks) and its extension (45 pixels/blocks) for feature extraction [LXK11].

detectors. The left eye map  $M_{left}(x, y)$  is defined in the template as follows,

$$M_{left}(x, y) = \begin{cases} 1 & \forall I(x, y) \in I, I(x, y) < \min(I_i^{left}) \\ 0 & \text{otherwise} \end{cases} \quad i = 1, 2, \dots, 5 \quad (3.32)$$

where  $I(x, y)$  is the intensity value of the current pixel with the given coordinates  $(x, y)$  in the image  $I$ ;  $I_i^{left}$  denotes the intensity values of the neighboring pixels defined in the eye template as shown on the left side in Fig. 3.34. Similarly, the right eye map  $M_{right}(x, y)$  can be defined as

$$M_{right}(x, y) = \begin{cases} 1 & \forall I(x, y) \in I, I(x, y) < \min(I_j^{right}) \\ 0 & \text{otherwise} \end{cases} \quad j = 1, 2, \dots, 5 \quad (3.33)$$

Based on Eq. (3.32) and Eq. (3.33) a consolidated eye map  $M$  for all the eye candidates are generated as

$$M = M_{left}(x, y) \cup M_{right}(x, y). \quad (3.34)$$

To rule out the spurious eye candidates various condition checks with respect to intensity level, geometric characteristics (e.g., distance, angle, symmetry, etc.) are specified in the algorithm described in [LXK11].

The mean ( $H$ ) and Gaussian ( $K$ ) curvatures are well-known measures for surface classification [PS85]. According to the sign of the computed  $H$  and  $K$  surface curvatures the image pixels can be classified in one of the eight different surfaces, i.e., peak,

### 3.3 Algorithms and Methods for 3D Embedded Vision

---

pit, flat, minimal, ridge, valley, saddle ridge and saddle valley. Generally  $H$  and  $K$  surface curvatures are computed from depth images. However, on the one hand the surface coherency property inferred by reflectance information can be used to estimate the curvatures from the intensity image [BJ88], and on the other hand the surface curvature estimation is preferred to be done on intensity images due to relatively poor discrimination among facial components in depth images. Hence, a geometric feature map is computed from the intensity values of the facial sub-image using the method implemented in [HBMB07]. This procedure can be performed in parallel with eye candidates searching (see Fig. 3.33) to achieve higher processing speed. The extended eye template consisting of prominent regions of the potential eyes and nose (see Fig. 3.34) is applied on the region of interest (ROI) of the computed feature map for feature extraction as shown in Fig. 3.35. In the end, the extracted curvature measures can be used as local features for the classification of eye candidates.

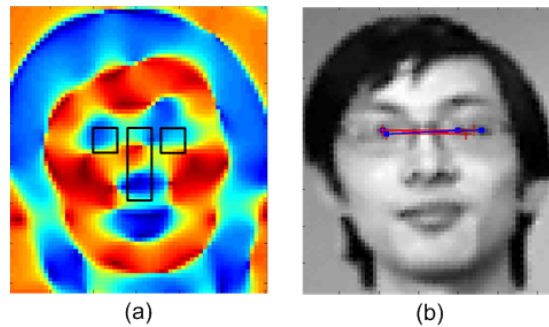


**Figure 3.35: Eye localization (feature map)** - (a) the computed feature map with the extended eye template and (b) eye pair candidates on the facial sub-image [LXK11].

The experimental results in [LXK11] show that the proposed eye template is particularly suitable for images with low spatial resolution. Using ARTTS 3D-TOF database [ARTTS08] and self-made Kinect image database the SVM classifier is trained in a supervised manner with hand labeled true eye pairs (ground truth) and non-eye-pair candidates detected through the eye template based searching procedure. The average detection accuracy of eye pairs on different face image databases with up to three persons in a scene is more than 92% despite of the simplified scheme for face detection [LXK11].

The above mentioned eye localization algorithm has evolved afterwards to a multi-user eye tracker by taking significant optimizations and by incorporating video-based

### 3. ADVANCED EMBEDDED VISION SYSTEMS FOR ADAS

---

object tracking [LXK12]. The proposed object tracking method, which is based on difference map of consecutive depth images, achieves superior results compared to state-of-the-art intensity image based tracking techniques with respect to tracking accuracy and occlusion handling. Using this method the head/eye positions of multiple users can be detected and tracked accurately with relatively low overall computational cost. This method can be further enhanced with effective real-time tracking algorithms, so as to serve the needs of human-vehicle interfaces in ADAS system for automatic (multi-user) eye gaze estimation, intention prediction, etc., and to perform driver status monitoring or in-vehicle surveillance.

#### 3.3.2 Kinect based Object Tracking

Depth camera can extend driver status monitoring in the 3rd dimension. By using state-of-the-art depth cameras, vision systems are able to perceive distance and build up 3D profile of objects without compromising field-of-view, robustness to lighting conditions and computation performance, which are intrinsically limited in stereo vision systems [LXK11]. As a low-cost commodity depth camera Kinect sensor is incorporated in the presented system due to its satisfactory depth sensing resolution, ease of use, as well as the variety of software resource. The key software components of Kinect are the skeleton tracking algorithm derived from the human body parts recognition method [SFCS11], and the CANDIDE-3 based face tracking algorithm.

In [SFCS11] a new method is proposed to estimate 3D positions of body joints from a single depth image, in a fast and accurate way, without using temporal information. Thanks to large-scale and highly varied training data, the realized classifier is able to estimate body parts invariant to body shape, pose, clothing, etc. The classification result is re-projected on the scene to find local modes, and finally the 3D proposals of body joints with confidence score are generated. Based this method, a human body skeleton made of several body joints can be detected from the recorded depth images, and be applied on the object under tracking afterwards.

CANDIDE, a parameterized face mask specifically developed for model-based coding of human faces, was created by Mikael Rydfalk in 1987 [Ryd87]. It became well known to a larger public through the research of Forchheimer *et al.* [FK89, LRF93, LLF94]. With low number of polygons (approximately 100), CANDIDE allows fast reconstruction at moderate computation cost. As an updated parameterized face

### 3.3 Algorithms and Methods for 3D Embedded Vision

model, CANDIDE-3 [Ahl01] consists of 113 vertices and 168 surfaces and has improved mouth and eyes modeling significantly compared to its earlier versions. CANDIDE and its improved versions has been widely used in computer vision, e.g., MPEG-4 Facial Animation Parameters [MPEG4]. With the built-in CANDIDE-3 face model, the Face Tracking Software Development Kit (SDK) along with Kinect for Windows SDK [FaceTracking] is adopted in this research work with modifications, so as to utilize the real-time face tracking for driver status monitoring. Fig. 3.36 visualizes the wire-frame model CANDIDE-1 and its improved version CANDIDE-3. The head movement seen by Kinect can be captured in terms of pitch, yaw, roll around three axes in 3D coordinate system. Facial features such as locations of eyebrows, mouth, nose, and other facial components are computed as well.

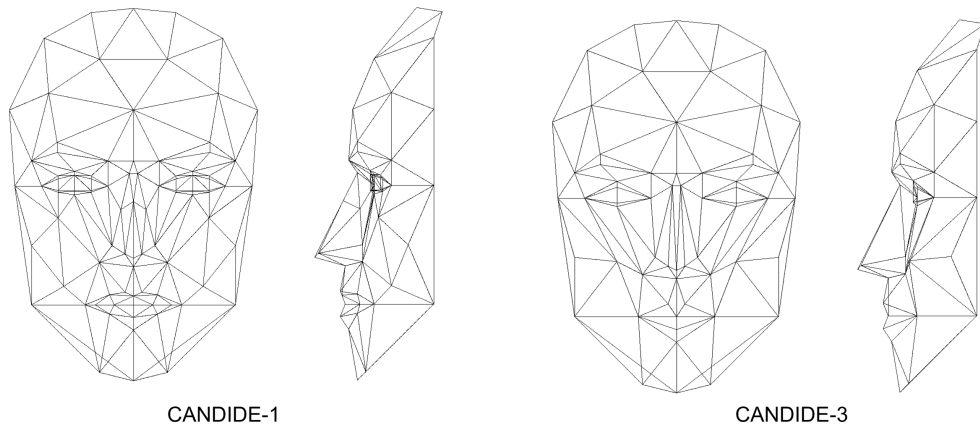


**Figure 3.36: CANDIDE** - The different versions of the parameterized face mask: CANDIDE-1 (front and side views) and CANDIDE-3 (front and side views).

Many Active Appearance Model (AAM) methods are based on CANDIDE. A real-time 3D face tracking algorithm based on AAM constrained by depth data is developed by Microsoft and used in the Kinect system [SHLA14].

Among the selected sensory data/features, such as ocular measures, etc., the relation of observed head orientation (yaw, pitch and roll) and driver's drowsiness state has been investigated by utilizing the state-of-the-art IR depth camera in the frame of this research work. A similar study on driver's head orientation and drowsiness state, however, with focus on the estimation of head orientation by exploiting three points face features using conventional RGB camera, can be found in [AM13].

#### 3.4 Summary and Discussion

Depth perception is a valuable complement to conventional color/intensity imaging in a variety of application fields, e.g., industrial, robotics, consumer electronics for home/office use, etc. Despite many application-driven innovations have been made in 3D sensing, depth camera based 3D embedded vision in automobile is still scarce. In the recent years novel IR depth sensors/cameras bring the embedded vision in the third dimension to enhance the sensing capability for better human-vehicle interactions, and to move forward towards smart driving. There are new sensor components/systems with decent depth resolution, computing power, and intelligent data processing algorithms. The fusion of various depth perception principles in a single compact sensor embodiment starts to emerge as well.

To gain depth/distance information stereo imaging system is able to compute disparity map out of stereo views, so as to facilitate the image segmentation procedure, which is usually the precondition for further processes such as object detection/tracking. However, stereo imaging has several intrinsic limitations such as correspondence problem (stereo matching) which requires complex algorithm and high computational cost to compensate and stereo imaging itself is also sensitive to illumination change.

Light sheet based 3D object sensing (see 3D laser scan in 3.1.4.2) is a very robust method of 3D imaging. Many industrial applications have linear motion of the objects, thus, profile scan methods can fit such purpose very well. Multiple cameras can be used for 360 degree coverage. 3D sensing on static objects/scenes requires sensor movement, and as such the technology is not suitable for object tracking applications.

Light-field imaging seems to remain immature to the present day. It offers rich features including after-the-fact-refocusing, depth map, etc., but it demands high processing power, and sacrifices image quality with regard to sharpness and resolution severely. The depth resolution of light-field images is coarse, and real-time video recording is not available. Thus, light-field technology requires further improvements to comply with applications of 3D embedded vision.

ToF imaging benefits from active illumination that can suppress or limit the influence of environment light conditions. No matter using continuous wave or pulse modulation, the obtained intensity and depth images are registered pixel by pixel accordingly in ToF camera, thus, do not require extra computational effort for image



matching which is crucial in conventional stereo imaging systems. In general, ToF imaging requires high accuracy time measurement – a good balance among light source power, integration time, and frame rate.

Depth sensing with novel structured light triangulation such as the Kinect sensor vitalizes the machine vision market, and enables massive innovations. Based on standard CMOS technology the Kinect sensor becomes a popular mass-production consumer electronics device with low cost, despite the fact that the operation range is limited by the baseline between IR light source and depth sensor, and depth sensing capability can be impaired by the shadow effect of projection.

It must be noted that depth cameras are having great potential for gesture based human-machine interactions, e.g., natural user interface (NUI), gesture recognition/control in consumer applications for gaming/home/office use, robot control, etc. Here are the emerging application fields where (IR) depth cameras are already employed.

- Interactive digital signage for commercial advertisement
- Digital identity (player-recognition),
- Full body 3D scan, human body mass estimation with Kinect [VDPA12]
- Industrial robot control
- Surveillance (people counting and classification)
- Automotive applications such as driver assistance
- Telepresence and video conference
- Virtual reality
- Augmented reality (e.g. LEGO® vending machine)
- Gesture control in car infotainment system

The combination of conventional 2D color vision with depth sensing, low-power consumption and miniaturization of sensor/camera components exhibit the technological advances and trends of depth cameras. For example, Microsoft Kinect V2 is so far the highest resolution 3D depth camera (full HD) available on the market which combines ToF technology with 2D imaging. Similarly, the 1.3 megapixel 2+3D<sup>TM</sup> camera from

### 3. ADVANCED EMBEDDED VISION SYSTEMS FOR ADAS

---

Depth imaging gives comparable depth accuracy with fairly lower color image resolution. PMD CamBoard nano [PMDnano15] with a ToF image sensor and a single LED as light source in compact design ( $37 \times 30 \times 25$  mm) is developed for consumer electronics such as smart phone and tablet PC. More technical details of the state-of-the-art depth cameras are summarized in Table 3.2.

Additional technical specifications of depth cameras, such as field of view (FOV), illumination power of light source, modulation frequency, data and control interfaces, e.g., USB, Ethernet, data (output) format, price information (if available), and product feature highlights, can be found in *Depth Sensor Database* in Appendix.

Considering automotive applications, in particular, ADAS applications, the following system design metrics with respect to 3D embedded vision should be taken into account:

- Compact design
- Energy footprint (power consumption)
- Computational requirements
- Potential cost (affordable)
- Robustness

In the final system realization of the research work, DriMix Micro-3D-Camera is not used, because

1. the image registration rate of the camera prototype is not real-time, yet to be improved by implementing the depth calculation algorithm in the sensor hardware directly;
2. the laser power used is not eye-safe for human, thus, not suitable for driver monitoring applications.

Despite certain limitations as mentioned previously such as limited operation range due to baseline setup between light source and depth sensor, weakness against shadow effect of projection, the Kinect sensor, however, exhibits good usability, decent depth sensing accuracy, robust performance, as well as excellent built-in real-time functions (e.g. object tracking and face recognition), and it is prevailing in consumer electronics

### **3.4 Summary and Discussion**

---

(availability and affordability). Therefore, the Kinect sensor V1 was selected as the key system component in the DeCaDrive project which will be addressed in Chapter 6.

### 3. ADVANCED EMBEDDED VISION SYSTEMS FOR ADAS

---

**Table 3.2:** Specifications of the State-of-the-Art Depth Cameras

Depth Camera Model Name	Tech. Mode	Depth Acc. [cm]	Frame Rate [fps]	Operation Range [m]	Wavelen. [nm]	Output Resolution
MESA SR3000 [MESA]	$CW^1$	1	25	0.8 – 8	850	$176 \times 144$
MESA SR4000 [MESA]	$CW$	1	50	0.8 – 8	850	$176 \times 144$
PMD Tech CamCube3 [PMDnano15]	$CW$	1	80	0.3 – 7	870	$200 \times 200$
PMD CamBoard nano [PMDnano15]	$CW$	0.5	90	0 – 2	850	$160 \times 120$
Canesta DP208 [Canesta]	$CW$	0.6 – 30	30	0.1 – 6	785	$64 \times 64$
Fotonic B70 [Fotonic]	$CW$	0.3 – 1.5	75	0.1 – 7	808	$160 \times 120$
Panasonic D-Imager [Panasonic]	$CW$	3 – 14	30	1.2 – 9	850	$160 \times 120$
odos VS-1000 [odos15]	$PG^2$	1	30	0.5 – 10	905	$1280 \times 1024$
TriDiCam LDPD [TriDiCam]	$PM^3$	1	100	0.3 – 10	850	$128 \times 96$
OptriCam DS10k-A [Optrima]	$PM$	1 – 3	50	1 – 10	870	$120 \times 90$
Point Grey Bumblebee2 [PointGrey]	$PT^4$	0.2	48	0.5 – 29	N/A	$648 \times 488$
DriMix iC-TS006 [iC-Haus]	$PM^5$	1 – 10	10	1 – 5	850	$80 \times 60$
Microsoft Kinect V1 [KinectV1]	$AT^6$	1	30	0.8 – 3.5	830	$640 \times 480$
Microsoft Kinect V2 [KinectV2]	$PG$	1	30	0.5 – 4.5	830	$1920 \times 1080$

1. Continuous wave modulation with lock-in pixels
2. Pulsed light with fast gating
3. Pulse modulation with lateral drift-field photo detector
4. Passive triangulation with stereo vision
5. Pulse modulation with drift-field-mixing concept
6. Active triangulation with structured light

## Chapter 4

# Further Sensory Building Blocks for ADAS

This chapter gives a survey on the state-of-the-art methods of measurement and sensory principles with the focus on ADAS building blocks complementing the solely vision-based solutions for general-purpose driver status monitoring. These diversified building blocks are ranging from conventional vehicle sensors, driver body measurement (skin impedance) sensor, EEG, ECG to electronic nose that are discussed in Section 4.1 to 4.5 respectively. The associated sensory data evaluation and feature computation of the building blocks are addressed in the respective sections. Finally, this chapter is summarized in Section 4.6.

### 4.1 Vehicle Dynamics Measurement

#### 4.1.1 Measurement and Sensory Principles

Today's vehicles are having up to four wheel speed sensors used for the anti-lock braking system (ABS). Wheel speed sensors generate an electrical signal that is proportional to the speed of the wheel. The ABS module can condition the generated signals to determine vehicle speed and transfer the data via controller area network (CAN). The transferred data can be visualized by the connected instrument cluster for speedometer function, and can be used by power train control module for functions like adaptive cruise control (ACC). The vehicle speed information can be further processed with other data to determine the fuel efficiency. In addition, vehicle speed is needed by

#### 4. FURTHER SENSORY BUILDING BLOCKS FOR ADAS

---

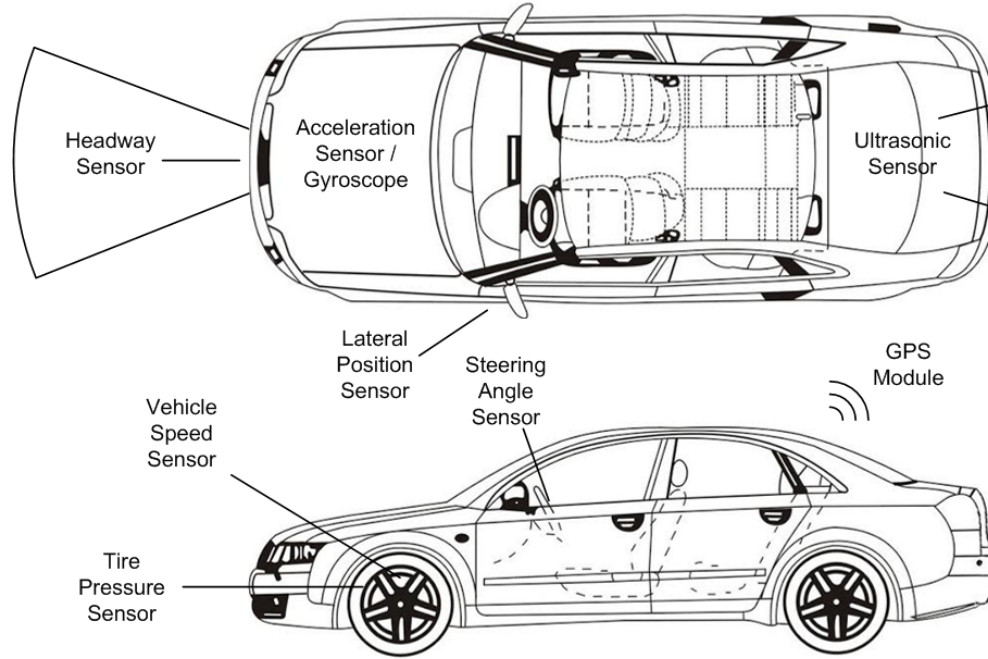


**Figure 4.1: Vehicle sensors to measure dynamic motions** - The number of automotive sensors in a single vehicle has been steadily rising over time.

body control modules (BCM) like door lock module to realize automatic door locks after vehicle start and beyond a specified speed.

The steering wheel (position/angle) sensor is used to monitor actual steering wheel position to determine the driver's intended path of travel. It has a potentiometer capable of generating analog voltage signal in relation to steering wheel rotation. The generated analog voltage signal is conditioned and further processed by BCM to gain steering wheel position. Nowadays the steering angle sensors are mostly photoelectric sensors that detect the rotation of steering wheel using light-sensitive elements [Hol10].

As mentioned previously in Section 1.1, vehicle lateral position, or say, lane position is considered as key indicator for detecting driving ability in case of driver fatigue. Lateral position sensor is used to measure the distance between the vehicle and the lateral lane markings. Infrared sensor, radar sensor can perform well in certain situations to determine lateral position of vehicle. Video-camera-based lateral position sensor is able to cope with a wide variety of situations, thus, can be taken as a good base to build a robust lane departure warning system [SJBG03].

The ultrasonic sensors transmit and receive acoustic waves beyond human audible

range (ultrasound) at a frequency between 25 kHz and 50 kHz. An ultrasonic sensor is used for calculating the distance and/or detecting objects based on the time-of-flight of ultrasound to travel to the target and reflect back. Automotive ultrasonic sensors are commonly seen in applications such as parking assistance, blind spot detection, etc., where the system performs object detection based on range sensing, and acoustically alarm the driver to other vehicles or obstacles within close proximity. In recent years, the ultrasonic sensors are evolving into automatic parking systems, automatic braking systems (for collision avoidance), as well as autonomous driving systems, along with other sensing technologies such as vision, radar, LIDAR, etc.

As attitude indicator, gyroscopes are useful for measuring or maintaining object orientation in space. The success story of advanced Micro-Electro-Mechanical Systems (MEMS)-based gyroscopes in automotive applications started nearly 20 years back, since the first yaw rate sensor in MEMS was introduced and incorporated in electronic stability program (ESP) by Bosch in 1998 [CFKE07]. The ESP system, recognized as one of the most important active safety systems, relies on the input of yaw rate sensors to detect the loss of steering control, and apply yaw control via ABS to brake individual wheels, so as to aid control over the vehicle. Three-axis MEMS-based gyroscopes commonly seen in consumer electronic devices provide 6 component motion sensing, i.e., acceleration for X-, Y-, and Z-movement, and gyroscopes for measuring the extent and rate of rotation in space (roll, pitch and yaw). Similarly, flexible inertial sensor clusters encompassing gyroscope and accelerometer can be seen in the automotive subsystems. In addition, 9-axis (acceleration, gyro, magnetic x/y/z sensing) MEMS units are available on the market [InvenSense, ST9D, BOSCH].

Since the first Global Positioning System (GPS)-based car navigation system was introduced in the early 1990s, automotive navigation systems prevail gradually and become a standard function in modern automobile. A GPS module allows the car navigation system to calculate routing based on current positions and to aid driving activity. To gain improved position resolution, differential GPS (DGPS), utilizes fixed, ground-based reference station networks to broadcast the difference between the GPS positions provided by the satellite signals and the known reference positions. Assisted GPS (A-GPS) further augments stand-alone GPS by using data of cellular base stations to enhance localization precision and navigation quality in case of poor satellite signal

## 4. FURTHER SENSORY BUILDING BLOCKS FOR ADAS

---

conditions. Hence, such GPS-based automotive navigation requires infrastructure improvements and relies on up-to-date and accurate map data. In addition, the sensory data of gyroscope and accelerometer can be used for greater reliability, as GPS signal loss and/or multipath propagation may occur in situations like traveling down through urban canyons, tunnels, etc.

The headway sensors can detect the distance between a vehicle and any vehicles or large objects in front of the vehicle. These sensors are used by ACC and/or collision avoidance systems (also known as precrash detection system). Most existing headway sensors use a 76.5 GHz radar, but other frequencies (e.g. 24 GHz, 35 GHz and 79 GHz) are also in use. Radar signals are very good at detecting objects that strongly reflect electromagnetic radiation, e.g., metal objects. These radar signals operate at wavelengths on the order of a few millimeters, thus, automotive radar systems are suitable for detecting objects of several centimeters or larger sizes. Some systems use infrared sensors instead of (or in addition to) the radar sensors. Furthermore, the gyroscope sensor in vehicle can be used to compensate the measurement error of headway sensor, so as to cope with diversified landforms and road characteristics (e.g. uphill, downhill, pit).

The tire pressure sensors can directly or indirectly measure the air pressure of individual wheels which can have severe impact on vehicle dynamics. A tire pressure monitoring system (TPMS), usually consisting of tire pressure sensors, battery management, wireless communication interface and microcontroller, can continuously monitor the tire pressure and report the measurement results via human-vehicle interface (in real-time). TPMS can be used to avoid traffic accidents, poor fuel economy due to under-inflated tires by detecting the hazardous states of tires in early phase.

To give an overview the important sensors for vehicle dynamics measurement are visualized in Fig. 4.1.

### 4.1.2 Data Analysis for Vehicle Sensors

Speed variation can be used as a metric of driver response to situations where the speed changes are required. It can be influenced by voluntary speed changes, e.g., due to change of road environment, or by involuntary speed changes due to loss of speed control. However, the relation between speed variation and accident risk is difficult to comprehend and explain. Thus, there are more useful alternatives, e.g., mean speed



and headway metrics, which are relatively easy to interpret with respect to driving performance and risk of accident.

Mean speed, speed variation and maximum speed are frequently used speed metrics. Mean speed is defined as the average travel speed (km/h). Mean speed is a reliable and valid metric of driving performance in scenarios where the driver determines and controls the speed, such as in rural road and motorway driving during low traffic intensity hours. Mean speed is not useful in scenarios where speed is controlled by traffic flow or other environmental factors. Maximum speed can reveal occasional severe loss of speed monitoring. Occasional speeding behavior can be caused by visual and cognitive distraction.

In general, increased lateral position variation indicates a reduced lateral control, while reduced lateral position variation is found when drivers are under cognitive load [BVW91, EJO05].

Mean lateral position is defined as the average distance between the right side of the front or rear right wheel and the inner (closest) edge of the right hand lane marking. Lateral position (LP) should be measured perpendicular to the lane marking. In case of several lanes (e.g. motorways), the lane markings of the current lane should be used. Mean lateral position is not defined during lane changes.

Mean time-to-line-crossing (TLC) is defined as the mean of the TLC local minima, where TLC is defined as the time to cross either lane boundary with any of the wheels of the vehicle if speed and steering wheel angle are kept constant. TLC metrics are only defined if the vehicle is within a lane. Decreased mean TLC indicates a decreased lateral control performance on either a regulatory or tracking level. Visual distraction and heavy cognitive load lead to decreased mean TLC.

Minimum time headway is defined as the minimum time gap (seconds) to a lead vehicle, traveling in the experimental vehicle's path of travel, while mean time headway is defined as the mean value of the time gap (seconds) to a lead vehicle. Headway is calculated as the distance to the lead vehicle (bumper to bumper) divided by the experimental vehicle travel speed. Small headways are related to high risk of collision. Headway larger than 3 seconds can be considered safe and are of little interest. Headway less than 1 second can be considered unsafe, but the subjective estimation of safe headway varies a lot between drivers. Decreased and increased headway may reflect loss of situation awareness if the driver is engaged with a distracting (visual or cognitive)

#### 4. FURTHER SENSORY BUILDING BLOCKS FOR ADAS

---

task. Increased headway may also indicate that the driver decides to increase the distance to the lead vehicle in order to compensate for increased distraction/cognitive load.

The brake jerks metric is a binary metric, which is true or = 1 if there was one or several abrupt onsets of the brakes during driving, and false or = 0 otherwise. Abrupt onset of the brakes is defined as the occurrence of a deceleration change higher than  $10 \text{ m/s}^3$ , induced by braking. As with line crossings, analysis of situations where brake jerks are found may give valuable understanding of the effects of distraction and cognitive load on the driver. Brake jerks of the specified amplitude only occur in very hazardous situations, thus indicate high risk of accident. Only brake jerks that would have been avoided if the driver was not distracted or under cognitive workload indicate that driving performance was deteriorated.

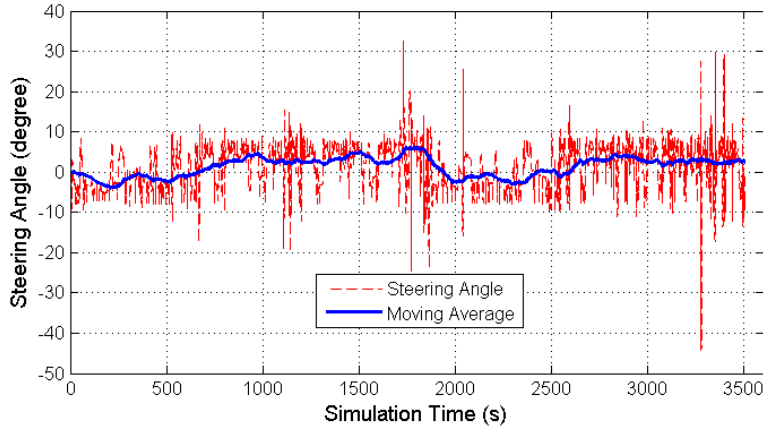


**Figure 4.2: General trend of steering angle** - A general trend of steering wheel movement over a 58-minute driving simulation can be computed based on moving average of steering angle data.

An example of general trend of steering angle in a driving simulation experiment illustrated in Fig. 4.2. The following features of steering angle sensor data can be considered in driver status monitoring. Steering reversals being related to micro-corrections indicate the frequency of lateral motion changes (left-right or right-left) within gap size  $\theta$ . Depending on  $\theta$  two features are taken into evaluation (with  $\theta = 1^\circ$  and  $\theta = 3^\circ$  respectively). Steering-same-side represents the frequency of steering motion in the same direction above threshold  $\vartheta$  which indicates lane changing or curve turning movements. Two features are computed based on  $\vartheta = 12^\circ$  and  $\vartheta = 32^\circ$  respectively. Mean

## 4.2 Body Measurement: Impedance Spectroscopy

---

and standard deviation of steering wheel positions within a measurement time frame are evaluated. The percentage of micro-corrections being taken to the overall steering motion as well as the steering velocity are considered here. In addition, FFT based frequency domain analysis of steering movement statistics can be performed to extract respective features. It should be noted that the parameters for feature computation are depending on system calibration and steering wheel specifications such as steering wheel size, resolution of steering angle sensor.

Despite the dependency on driving experience, type of vehicle, road and weather conditions, etc., the steering behavior indicated by steering wheel movement or by lane departure/line crossing is regarded as the most trustworthy measure of driving performance and has been widely employed in mainstream ADAS systems [LWK12]. The correlation between steering wheel movement and lane position processes which can be jointly used for drowsiness detection has been studied in [SP96].

## 4.2 Body Measurement: Impedance Spectroscopy

### 4.2.1 Measurement and Sensory Principles

Impedance spectroscopy (IS), also known as electrochemical impedance spectroscopy (EIS), measures the dielectric properties of a medium as a function of frequency. Since long time, it has been used in study on the electrical properties of biological tissues, regarded as bioimpedance analysis.

Thomasset explored the utilization of bioimpedance measurement in total body water estimation using bipolar electrode method [Tho63]. The bipolar electrode method employs single electrode for both purpose without separated current electrode and voltage electrode, so that the number of electrodes can be reduced and the lineup of the electrical circuitry as well as the sensor product composition can be simplified. The minimum required number of electrodes is 2 (+ electrode and - electrode). The electrodes can be actually attached to both arms and legs, so that the number of electrodes is possible to increase up to 8 (bi-polar electrode method using 8 touch type electrodes). The accuracy of this method is, however, lowered by the contact resistance generated from electrodes.

Nyboer applied quad surface electrode readings for bioimpedance measurements to estimate the fat free mass of the human body [Nyb70]. Hoffer *et al.* introduced the

## 4. FURTHER SENSORY BUILDING BLOCKS FOR ADAS

---

association between total body impedance and total body water content in reference to tritium dilution techniques [HMS69]. The tetra-polar electrode method separates the current electrode pair from the voltage electrode pair. Hoffer *et al.* and Nyboer introduced this method to make up for the weak point of bi-polar electrode method, so that contact resistance of electrodes was considerably reduced. Though, the lineup of electric circuit is complex and the number of electrodes is increased. The minimum required number of electrodes is 4 (current electrodes +/- and voltage electrodes +/-). Similar to the bipolar electrode method, the number of electrodes in the tetra-polar electrode method can be increased to cover both arms and legs in body impedance measurement.

A graphical comparison between bipolar and tetra-polar electrode methods for IS measurement can be found in Fig. 4.3. The problem of bipolar electrode method is that the true endogenous bioimpedance  $Z_{TUS}$  is masked through  $Z_k (\approx Z_{Skin} + Z_{Electrode})$ , i.e., the contact impedance of the joint current and voltage electrode on the measured skin surface, which leads to the measured frequency dependent impedance  $Z(\omega)$  as follows.

$$Z(\omega) = \frac{U(\omega)}{I(\omega)} = Z_{k1} + Z_{TUS} + Z_{k2}, \quad (4.1)$$

where  $Z_{k1}$  and  $Z_{k2}$  denote the contact impedance generated from the positive and negative electrodes respectively;  $Z_{TUS}$  is the tissue impedance to be measured.

Using tetra-polar method, where one pair of current electrodes to excite the tissue and another pair of voltage electrodes measure the voltage difference, there is almost no current flowing through the high impedance voltage electrodes, thus almost no  $Z_k (\approx 0)$  is measured along with  $Z_{TUS}$ . In this case, Eq. 4.1 can be reformulated as

$$Z(\omega) = \frac{U(\omega)}{I(\omega)} = Z_{TUS}. \quad (4.2)$$

### 4.2.2 Data Analysis for Skin Impedance Measurement

For impedance analysis of solids and liquids a simple RC circuit model as shown in Fig. 4.4 are often used. Any electrode system in measurement has a geometrical capacitance  $C_g \equiv C_\infty = C$  and a bulk resistance  $R_b \equiv R_\infty = R$  in parallel with it, which lead to the time constant  $\tau_d = R_\infty C_\infty$ , representing the dielectric relaxation time of the basic material [MM05].

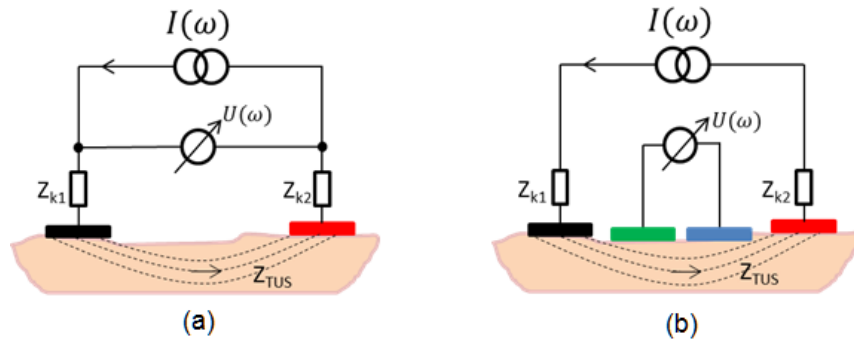


**Figure 4.3: Bipolar and tetra-polar electrode methods** - (a) Bipolar method with joint current and voltage electrode; (b) tetra-polar method with separate current and voltage electrodes [BT13].

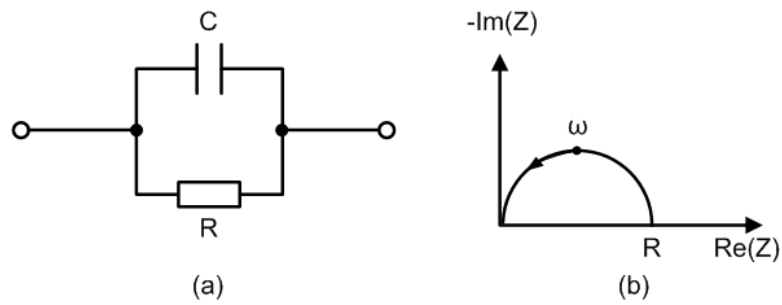


**Figure 4.4: Impedance plane plot** - Part (a) shows a common RC circuit. Part (b) shows the corresponding impedance plane plot. Arrows indicate the direction of increasing frequency [MM05].

#### 4. FURTHER SENSORY BUILDING BLOCKS FOR ADAS

Three-dimensional plot is often used to examine and visualize the IS data. A 3D plot, as depicted in Fig. 4.5, consists of a normal complex plane plot in the real-imaginary plane plus the third frequency axis showing the impedance response in a proper 3D perspective [MM05]. In addition, software tools such as ZView® [ZVIEW] can be used to generate Cole-Cole plot.

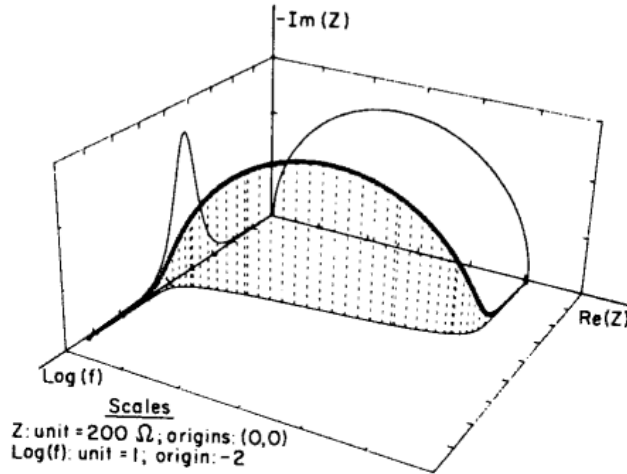


**Figure 4.5: Impedance plane 3D plot** - A 3D plot of impedance response, where a  $\log(\text{frequency})$  axis has been added at right angles to the ordinary  $-\text{Im}(Z)$ ,  $\text{Re}(Z)$  complex plane plot, allows frequency response to appear explicitly [MM05].

Electrical bioimpedance measurements are most often performed as deflection measurements by measuring the response of the system to an external electrical excitation [PW01]. The electrodes are a critical element of such IS measurement systems. They function as an electronic-to-ionic interface between the electronic conductor in the measurement leads and the ionic conductor in the load, i.e., biological tissue. This interface can be modeled as a parallel circuit of a variable resistance  $R_E$  and a variable capacitance  $C_E$  along with a variable voltage source  $U_{EP}$  at the interface (see Fig. 4.6). After measuring the response to the excitation in terms of voltage or current, the complex impedance is estimated by applying methods such as sine correlation and Fourier analysis [SFSB08].

The skin impedance  $Z$  varies in response to the frequency of the measurement alternating current (AC). The higher the frequency the more easily the current passes through, thus, the lower the impedance. A periodically measured skin impedance of approx.  $0.9 \text{ k}\Omega$  with  $30 - 100 \text{ kHz}$  measurement frequency is visualized in Fig. 4.7.

## 4.2 Body Measurement: Impedance Spectroscopy

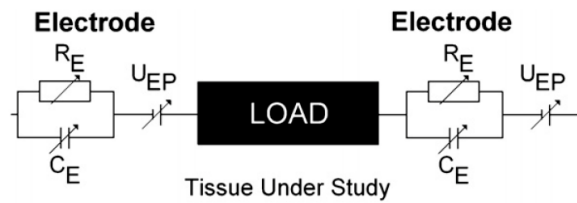


**Figure 4.6: Skin impedance measurement** - Equivalent model for the electronic-ionic-interface, and its connection with the working load – tissue under study (TUS) [SFSB08].

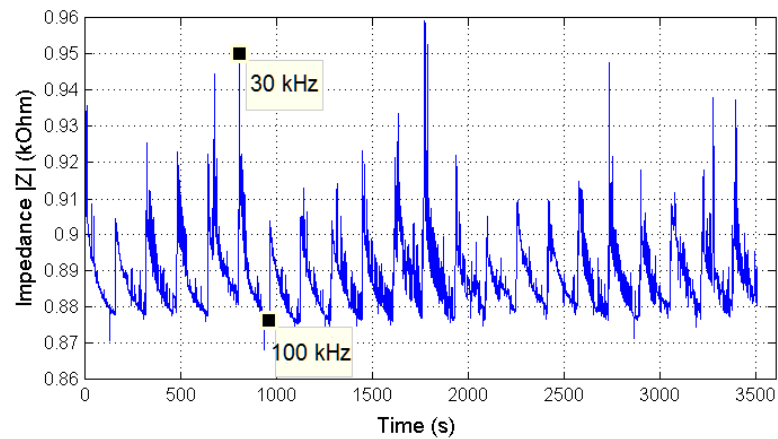


**Figure 4.7: Skin impedance response in time** - The magnitude of skin impedance  $Z$  changes in time in response to the periodically repeated measurement frequency 30 – 100 kHz.

### 4.3 Electroencephalography

#### 4.3.1 Measurement and Sensory Principle

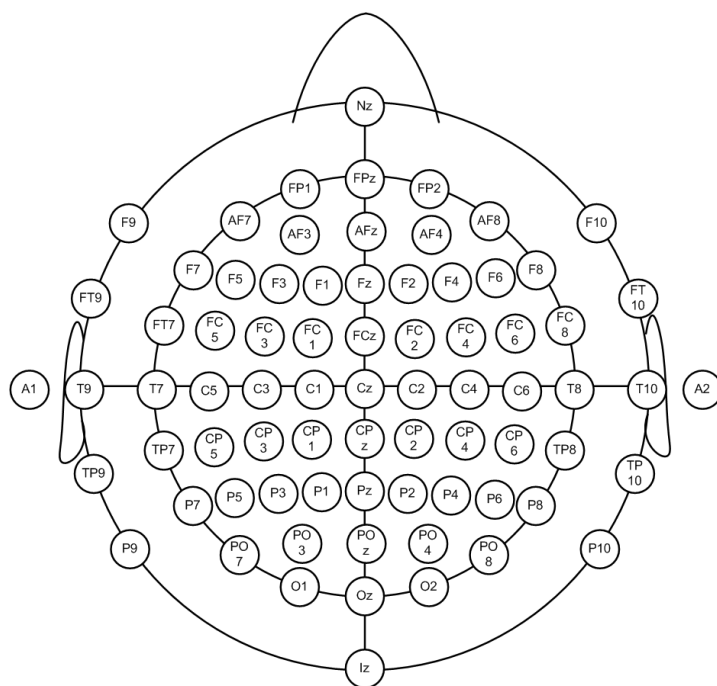


**Figure 4.8: The 10-20 system for EEG** - The standard locations of scalp electrodes specified in the 10-20 system [AES91].

As a typical non-invasive method, electroencephalography (EEG) can record electrical activity of the brain along the scalp. It measures voltage fluctuations resulting from ionic current within the neurons of the brain. In clinical contexts, EEG records the brain's spontaneous electrical activity in a certain time frame from multiple electrodes placed on the scalp. The locations and nomenclature of these electrodes are standardized by the American Electroencephalographic Society [AES91]. The 10-20 system is an internationally recognized method to describe and apply the location of scalp electrodes in the context of an EEG test or experiment (see Fig. 4.8). The "10" and "20" refer to the fact that the actual distances between adjacent electrodes are either 10% or 20% of the total front-back or right-left distance of the skull.

The clinical diagnostic applications generally focus on the spectral content of EEG signals that is the type of neural oscillations. The frequency spectrum of EEG signal is



ranging from 0.1 Hz to 70 Hz, which is classified in the following five frequency bands: delta, theta, alpha, beta and gamma, reflecting different levels of consciousness [BG10].

- Delta waves are the slowest in frequency but are the highest in amplitude. Observed in deep, dreamless sleep, this frequency is the gateway to the universal mind and the collective unconsciousness, where information received is otherwise unavailable at the conscious level. It is a dominant brainwave of infants (birth to 24 months) and even adults in deep sleep.
- Theta brainwaves occur during deep relaxation and meditation, light sleep or lucid dreaming including the REM dream state (Rapid Eye Movement sleep). The lower the brain frequency the faster the learning. Most children and teenagers have dominant theta brainwave patterns.
- Alpha brainwaves are slower in frequency as compared to Beta, which translates to a highly relaxed state of awareness. It is a normal brainwave pattern in people who are naturally relaxed and creative. Alpha brainwaves are considered the healthiest brainwave range and 10 Hz has widely been accepted as the "safest" brainwave frequency to train.
- Beta are the brainwaves of our normal waking consciousness. It is associated with a heightened state of alertness, logical thinking, problem-solving ability, concentration, when the mind is actively engaged in mental activities. But higher Beta levels also result into stress, anxiety and restlessness.
- The Gamma brainwave is the fastest frequency at which the brain functions, where an individual can experience bursts of insight or high-level information processing.

A brief summary of the EEG signal frequencies and the associated functions can be found in Table 4.1. In detection of driver drowsiness, particularly for microsleeps, EEG based approach has given results indicating that microsleeps have EEG shift to lower frequencies (from alpha to theta waves) [BTTPR08].

In recent years, consumer brain-computer interface (BCI) devices emerge thanks to the development of EEG technology. The representative products seen in the consumer market are NeuroSky and Emotiv devices as illustrated in Fig. 4.9.

#### 4. FURTHER SENSORY BUILDING BLOCKS FOR ADAS

---

**Table 4.1:** EEG signal frequencies and the associated functions [BG10]

Brainwave Type	Frequency Range	Mental States and Conditions
Delta	0.1 Hz to 3 Hz	Deep and dreamless sleep, unconscious sleep, unconscious state
Theta	4 Hz to 7 Hz	Intuitive, creative, recall, fantasy, imaginary, dream
Alpha	8 Hz to 12 Hz	Relaxed, but not drowsy, tranquil, conscious
Beta	12 Hz to 25 Hz	Relaxed yet focused, integrated, thinking, aware of self and surroundings, alertness, agitation
Gamma	26 Hz to 70 Hz	Higher mental activity, to be seen in conscious waking state and REM dreams

NeuroSky released the first affordable consumer based EEG along with the game NeuroBoy in 2007. This was also the first large scale EEG device to use dry sensor technology. ThinkGear is the technology inside every NeuroSky product or partner product that enables a device to interface with the wearers brainwaves. It includes the sensor that touches the forehead, the contact and reference points located on the ear pad, and the on-board chip that processes all of the data. Both the raw brainwaves and the eSense Meters (attention and meditation) are calculated on the ThinkGear chip. *eSense<sup>TM</sup>* is a NeuroSky's proprietary algorithm for characterizing mental states. To calculate eSense, the NeuroSky ThinkGear technology amplifies the raw brainwave signal and removes the ambient noise and muscle movement. The eSense algorithm is then applied to the remaining signal, resulting in the interpreted eSense meter values. Please note that eSense meter values do not describe an exact number, but instead describe ranges of activity.

Emotiv EPOC headset is a high resolution, multi-channel, portable EEG system that features 14 EEG channels with saline soaked felt pads (at location AF3, AF4, F3, F4, FC5, FC6, F7, F8, T7, T8, P7, P8, O1, O2 as per the 10-20 system), plus 2 references with left/right mastoid process / Alt P3-P4. The advanced model *EPOC+* features motion sensors (accelerometer, gyro, magnetometer) and provides more user configurable options. The EPOC headset is able to detect the following facial expressions and emotional states.

- Facial expressions: blink, left wink, right wink, furrow (frown), raise brow (sur-



**Figure 4.9: Brain-computer interface** - Emotiv EPOC (left) [EPOC] and NeuroSky MindWave (right) [MindWave].

prise), smile, clench teeth (grimace), glance left, glance right, laugh, smirk (left side), smirk (right side).

- Emotional States: instantaneous excitement, long term excitement, frustration, engagement, meditation.

### 4.3.2 EEG Data Analysis

The advent of digital computers enables the advanced signal processing of high-density EEG recordings. Some open-source toolboxes can be used to process EEG data. As a prominent example EEGLAB is a toolbox with interactive graphic user interface (GUI) developed by Swartz Center for Computational Neuroscience, UC San Diego. The EEGLAB toolbox is available under the GNU public license for noncommercial use and open source development. It can be used under the cross-platform MATLAB environment to process collections of single-trial and/or averaged EEG data of any number of channels. The available functions of EEGLAB include EEG data, channel and event information importing, data visualization (scrolling, scalp map and dipole model plotting), preprocessing (including artifact rejection, filtering, epoch selection, and averaging), independent component analysis (ICA) and time/frequency analysis

#### 4. FURTHER SENSORY BUILDING BLOCKS FOR ADAS

---

(TFA) as well as standard averaging methods [DM04]. In particular, a primary function of EEGLAB is to facilitate the process of applying and evaluating the ICA results of EEG data. The core mathematical concept of ICA is to minimize the mutual information among the data projections or maximize their joint entropy. ICA algorithms have proven in [JMHL00] to be capable of isolating both artifactually and neurally generated EEG sources, whose EEG contributions across the training data are maximally independent of each other [DM04].

Further new plug-in toolboxes for advanced EEG signal processing, e.g., NFT – 3D head and source location modeling, are developed for EEGLAB in recent years.

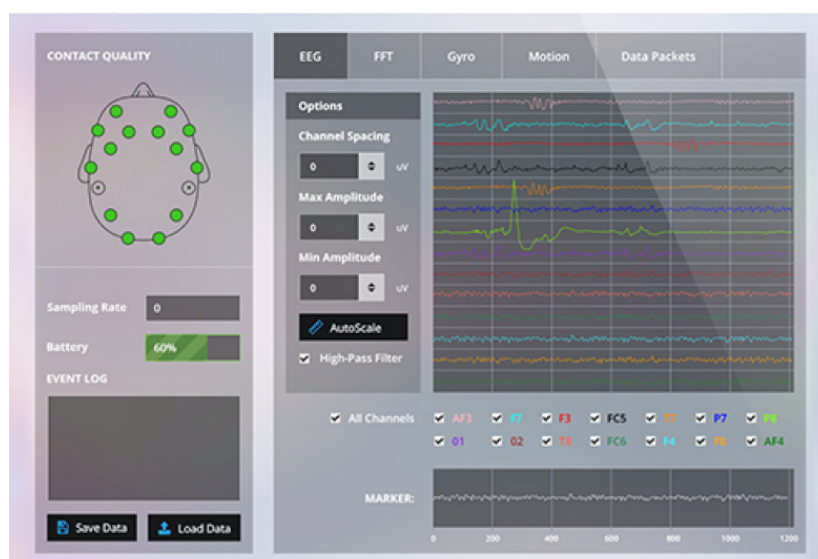


**Figure 4.10: Emotiv TestBench** - Features: 5 second rolling time window (chart recorder mode); all or selected channels can be displayed; automatic or manual scaling (individual channel display mode); adjustable channel offset (multi-channel display mode); synchronized marker window [EPOC].

Nowadays, with the advent and popularity of commodity EEG devices, a good example of EEG data analysis based on such devices can be seen in Fig. 4.10. Real-time display of the Emotiv headset data stream is shown on the *TestBench* GUI, including EEG, contact quality, FFT, gyro (if fitted custom option), wireless packet acquisition/loss display, marker events, headset battery level. Record and replay files are in binary EEGLAB format. Command line file converter is included to produce *.csv* format. Timed markers can be defined and inserted into the data stream, including

on-screen buttons and defined serial port events. Markers are stored in EEG data file. Marker definitions can be saved and reloaded. Markers are displayed in real time and playback modes.

## 4.4 Heart/Pulse Rate Measurement: ECG and PPG

### 4.4.1 Measurement and Sensory Principle

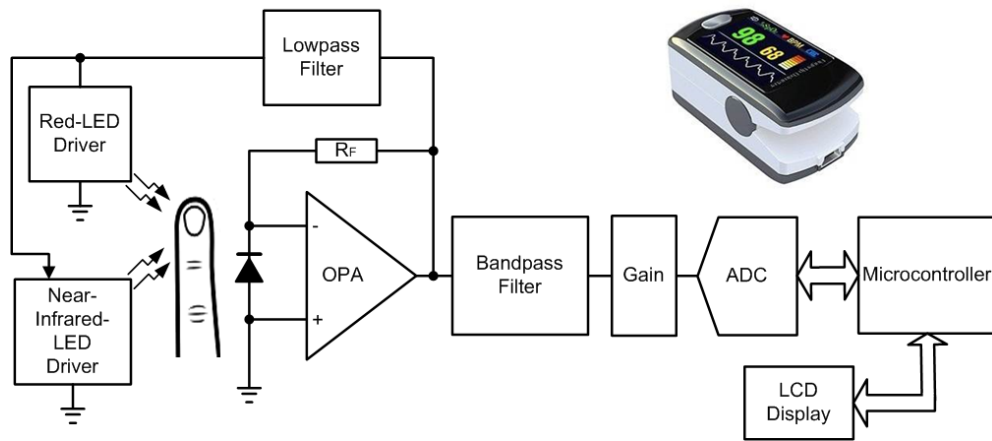


**Figure 4.11:** Pulox - Finger Clip Pulse Oximeter CMS-50E (top right) and a functional block diagram of PPG-based pulse oximetry. The red LED is on for 50 sec, both LEDs are off for 450 sec, the NIR LED is on for 50 sec, and then both LEDs are off for 450 sec. The system repeats this cycle continuously.

Electrocardiography (ECG or EKG) is the process of recording the electrical activity of the heart over a period of time using electrodes placed on a human body. These electrodes detect the tiny electrical changes on the skin that arise from the heart muscle depolarizing during each heartbeat. Until recently, ECG-based electrical biosensors were found only in high-end medical equipments.

The most common digital application of the highly informative ECG trace is heart rate variability (HRV) [WLAL11]. HRV can also be reliably estimated from photoplethysmography (PPG) [SJSD08]. ECG directly measures the bio-potential generated by electrical signals that control the expansion and contraction of heart chambers, while PPG senses the rate of blood flow during heart activity using electrical signals derived from changes in reflected light due to blood flow. In addition, PPG based methods

## 4. FURTHER SENSORY BUILDING BLOCKS FOR ADAS

---

have already been intensively studied and afterwards exploited for noninvasive pulse oximetry [Men88].

A typical PPG-based solution for heart rate measurement and blood oxygen metrics is visualized in Fig. 4.11. The pulse-oximeter circuit alternates the on-time of a red LED and a near-infrared LED to monitor blood oxygen saturation ( $SpO_2$ ). The transimpedance amplifier, A1, converts the photodiode current generated by the LEDs to a voltage at the output. The signal then travels through a bandpass filter and gain stage to the 12-bit ADC. The signal also travels through a lowpass filter to regulate the driver power to the LEDs. The microcontroller acquires the signals from the 12-bit ADC, computes the ratio of the red- and NIR-LED signals, and compares the results with a  $SpO_2$  look-up table. The LCD shows a percentage of oxygenated hemoglobin versus nonoxygenated hemoglobin and the heart rate [Tow01].

### 4.4.2 ECG/PPG Data Analysis

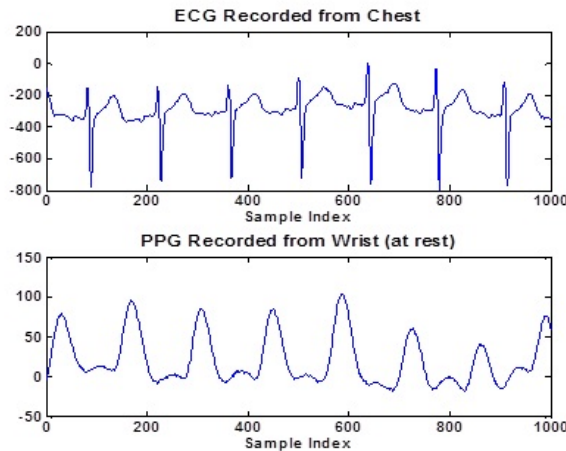


**Figure 4.12: ECG and PPG record comparison** - Simultaneously recorded ECG (from chest) and PPG (from wrist) when the subject was at rest. One cycle of PPG corresponds to one cycle of ECG with sampling rate 250 Hz [ECGPPG].

Pulse rate is one of the measurable vital signals that can be used to check heart health and fitness level. Pulse rate can be estimated from PPG signal records.

Fig. 4.12 shows a PPG segment and an ECG segment recorded at the same time when the subject was at rest (no obvious noise was present in both signals). In the recorded waveform one cycle of the PPG corresponds to one cycle of the ECG.

Accurately estimating pulse/heart rates from the PPG signals is sometimes quite challenging. In scenarios where e.g., subjects perform physical exercises or carry out strong motions, such as fast running, jumping, etc., it can result in huge motion artifacts in recorded PPG signals, making the pulse/heart rate estimation difficult.

Based on embedded pulse rate sensor on steering wheel the LF/HF ratio of heart rate variation, or say pulse rate, in frequency domain is suggested as an indicator for drowsiness detection in [Yu09]. With predefined low frequency band 0.04 – 0.15 Hz (LF) and high frequency band 0.15 – 0.4 Hz (HF) the LF/HF ratio of pulse rate course within a measurement time frame is computed. The mean value of pulse rate is taken up in feature computation as well.

There are interesting researches in ECG/HRV and pulse oximetry highlighting their potential applications in bioinformatics, e.g., human identification [BPPW99] and human state recognition [TVGS11].

## 4.5 Electronic Nose

### 4.5.1 Measurement and Sensory Principle

The term "electronic nose" (e-nose) was coined in 1988 by Gardner and Bartlett, who later defined it as "an instrument which comprises an array of electronic chemical sensors with partial specificity and appropriate pattern recognition system, capable of recognizing simple or complex odors/flavors [GB94].

A typical electronic nose system consists of a multi-sensor array, an information-processing unit based on e.g. artificial neural network (ANN), software with digital pattern classification/recognition algorithms, and reference databases. The multi-sensor array is composed of various sensors responding to a wide range of chemical classes and collectively discriminating diverse mixtures of possible analytes. The commonly used sensors for electronic noses include MOSFET devices, conducting polymers, polymer composites, quartz crystal microbalance, surface acoustic wave (SAW) devices, electrochemical gas sensors, fiber-optic gas sensors, etc. [WB09]

E-nose is utilized in a wide variety of industries such as automobile, food, cosmetic, analytical chemistry and biomedical industries for a broad and diverse range of applications including quality control of raw and manufactured products, process design, freshness and maturity (ripeness) monitoring, classification of scents and perfumes, and

## 4. FURTHER SENSORY BUILDING BLOCKS FOR ADAS

---

environmental assessment studies [WB09]. Finally, the exploratory use of e-nose to aid in the detection of driving impairment/deprivation due to inebriation is expected in ADAS domain.

There are commercial products, e.g., Micronas gas sensors based on CCFET (Capacitive Coupled Field Effect Transistor) technology [MICRONAS], UST gas sensing/e-nose systems based on resistive effects used in intelligent ventilation systems in cars [USTGAS].

### 4.5.2 Data Analysis for Electronic Noses

The typical analysis techniques for e-nose data can be classified in three main categories as follows [SBE98]:

- Graphical analyzes: bar chart, profile, polar and offset polar plots
- Multivariate data analyzes (MDA): principal component analysis (PCA), canonical discriminate analysis (CDA), featured within (FW) and cluster analysis (CA)
- Network analyzes: artificial neural network (ANN) and radial basis function (RBF)

The selection of the utilized method(s) depends on the type of sensory input and the type of information that is sought. In general, MDA is very useful when e-nose sensors have partial-coverage sensitivities to individual compounds in the sample mixture. The artificial neural network (ANN) can be used to identify underlying nonlinear models of e-nose data, so as to perform the (aroma) pattern recognition based on analyte-specific reference database [WB09].

## 4.6 Summary and Discussion

To gain reliable and as comprehensive as possible descriptions of the vehicle's dynamic motions, versatile sensory inputs including wheel speed, angular rates, lateral position, tilt angles, headway, linear accelerations, etc. need to be measured and evaluated. In addition, the road safety related automotive sensory components are vastly demanded due to the steadily strengthened regulations. For instance, from 1st November, 2014, all new passenger cars sold in the European Union must be equipped with a tire pressure



monitoring system (TPMS) (refer to Section 4.1.1) to avoid traffic accidents and poor fuel economy.

The bioinformatical data of driver, on the other hand, can contribute to the improved road safety as well. Skin impedance, heart/pulse rate, and EEG measures of the driver's brain, as well as the driver's body odor can be sensed and processed to monitor the driver's physiological and psychological states. Other novel sensor components/systems, e.g., E-Taster assistance system with Lab-on-Spoon [LabOnSpoon] and Lab-on-Fork as "electronic tongues" [ETaster] intended for smart kitchen and ambient assisted living (AAL) applications, could also be interesting in ADAS domain, and seek for their potential applications.

These diversified sensory building blocks including advanced embedded vision systems (see Chapter 3) can expand the range of ADAS applications and enable creative and innovative solutions to address active safety mechanisms such as collision avoidance, driver drowsiness detection as well as to maintain the general safe state of JCS. Hence, the selection of the suitable building blocks and their interconnections become crucial for the sensor data fusion and will impact the overall system performance. With regard to this, the top level ADAS system modeling concept and the associated design methodology are discussed in Chapter 5.

#### **4. FURTHER SENSORY BUILDING BLOCKS FOR ADAS**

---

## Chapter 5

# ADAS System Modeling Concept

Next generation ADAS aiming at smart driving and moving forward to its ultimate manifestation - autonomous driving, raises a set of challenging requirements on driving safety, connected security, and cutting edge signal processing as well as human-vehicle interfaces.

Inspired by the novel ADAS concept coupled with COCOM/ECOM model (see Chapter 2.2), and the advances in sensor electronics, functional building blocks (as described in Chapter 3 and Chapter 4), a generic system concept of driver status monitoring and the adopted design methodology are underlined in this chapter. An overview of the proposed system concept along with the holistic and integrated development and validation framework are given in Section 5.1, followed by the discussions on sensor feature selection and fusion algorithms in Section 5.2. Afterwards, an insight into relevant flat and hierarchical classification techniques is addressed in Section 5.3. The limitations and possible improvements are discussed in Section 5.4.

### 5.1 System Concept and Design Methodology

The challenges in the development of ADAS are large quantities of data from diversified sensor devices such as radar, lidar, ultrasonic, laser and video-based systems must be visualized and validated. The major goal of this research work was to study human driving behavior as well as vital signs of driver by exploiting novel sensing technologies and the combinations thereof, which can facilitate the realization of driver drowsiness detection in ADAS.

## 5. ADAS SYSTEM MODELING CONCEPT

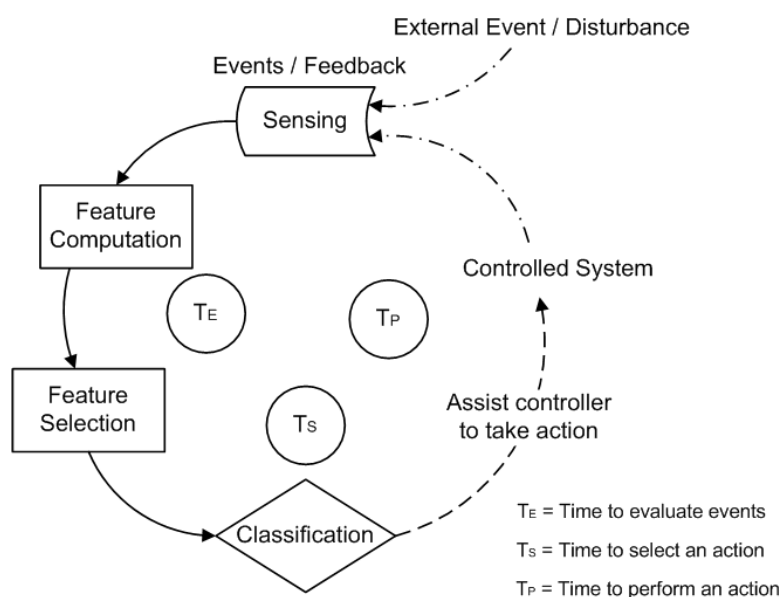


**Figure 5.1: Sensor signal processing pipeline mapped in COCOM** - The stages of sensor signal processing pipeline in ADAS, such as sensing, feature computation, feature selection, and classification can be mapped in the COCOM model as introduced in Section 2.2.1.

Based on the top level system concept involving controller and controlled system, the modeling of driver behavior in the context of human-vehicle interactions can be viewed in the decomposition of JCS. As part of JCS the sensor signal processing pipeline, which assists driver to perform a single control process on vehicle, can be mapped in COCOM model as shown in Fig. 5.1. The process including the assistance to decision making of the controller and the action being performed on the controlled system is marked with dashed arrow to differentiate itself from the sensing and data processing procedures. In addition, the feedback of controlled system in response to the undertaken action, as well as the input from external environment (outside of controlled system) construct the stimulus to JCS in terms of events/feedback.

The proposed system concept in the form of JCS has been broken down to building blocks on the function level as shown in Fig. 5.2. Benefiting from smart sensing and intelligent soft-computing, the proposed system concept has been formed as extendable/scalable, multi-sensory ADAS-architecture being able to cope with driver status monitoring and intention prediction. Smart sensors also adaptation/learning and self-x concepts can be discussed in this context. The information flows, or say, data and con-

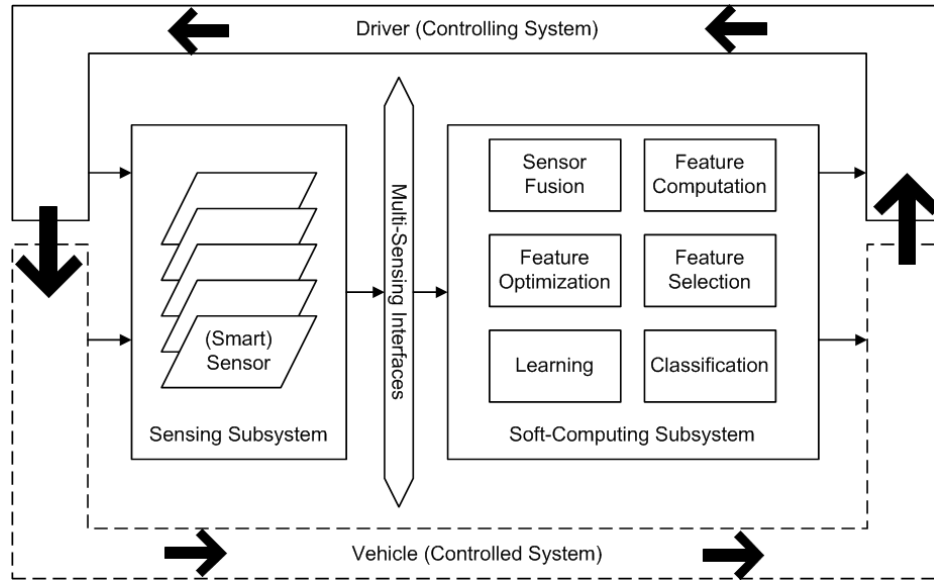


**Figure 5.2:** The proposed system concept - Extendable/scalable, multi-sensory ADAS-architecture for driver status monitoring.

control signal paths, within and surrounding the whole system are indicated by the (bold) black arrows. The common multi-sensing interfaces enable the interconnection between (smart) sensors and back-end system components. A structural metadata being formed by multi-sensing interfaces is crucial here for the exchange of sensory data along with descriptive information (e.g., timestamp, sensor type, data type, linkage to other data, etc.) among building blocks inside of the system.

**Design methodology:** The X-in-the-Loop (XiL) is a framework for validation of complex mechatronic drive systems. This approach can be used as a generic and scalable design methodology for the development of automotive and other mechatronic systems [Dus10]. For example, the IPEX XiL framework provides a holistic and integrated development and validation framework for powertrain systems. "X" represents the Unit Under Test (UUT). Compared to the widely used Hardware-in-the-Loop (HiL) approaches, the UUT in the XiL framework can be a real prototype as well as a simulated virtual prototype. The XiL framework can be used for design validation activities throughout the whole process of automotive engineering (see Fig. 5.3). It enables the system designers to focus on the interactions between the vehicle and its driver, its environment as well as its subsystems and interfaces at different levels of abstraction [ASM11].

## 5. ADAS SYSTEM MODELING CONCEPT

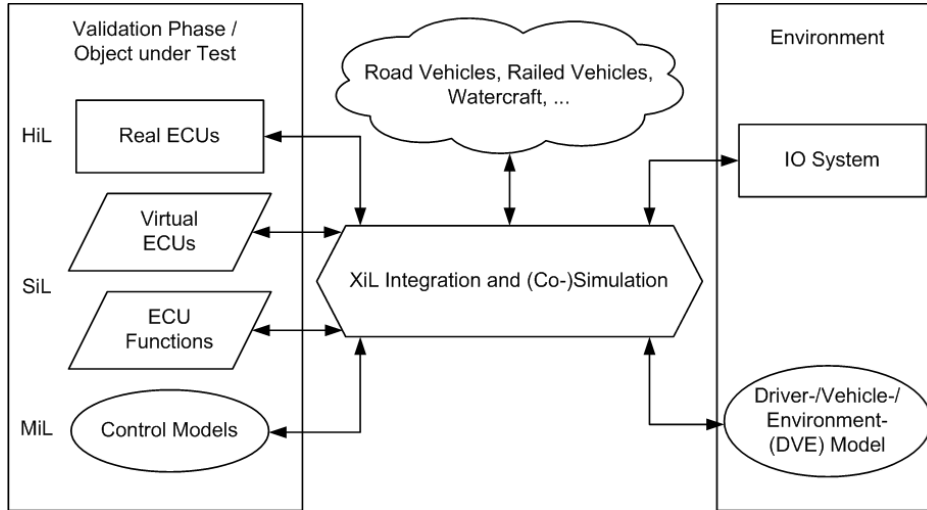


**Figure 5.3: The XiL approach** - XiL application in embedded software and system development: ECU denotes Electronic Control Unit; HiL, SiL, MiL stand for Hardware-in-the-Loop, Software-in-the-Loop, Model-in-the-Loop, respectively [EtasXiL].

In addition, considering the use of emerging smart sensors capable of self-monitoring, -trimming, -repair/healing/rejuvenation, the automated design approach of dependable intelligent sensory systems with self-x properties in [IK11] can be incorporated into the system design flow.

**AUTOSAR-based layered modular software design paradigm:** In order to achieve the technical goals: modularity, scalability, transferability and re-usability of functions, Automotive Open System Architecture (AUTOSAR), as shown in Fig. 5.4, provides a common software infrastructure for automotive systems of all vehicle domains based on standardized interfaces for the different layers [AUTOSAR]. Considering the future trend (refer to Section 2.3), next-generation ADAS systems have more extreme demands on e.g. network connectivity, 3D graphics processing, which leverage large code bases and possibly third party software with the lack of formal safe software development process. Designers must plan for serious problems with these increasingly complex systems and build a reliable, scalable software patch/upgrade system [Hoo15].

**The modularization and standardization of ADAS software components:** A world-wide recognized standard for ADAS is so far not yet established due to the diversity of applications and the complexity of system functions. It would be difficult to form the ADAS standard without consolidation of system architecture, configuration

## 5.1 System Concept and Design Methodology

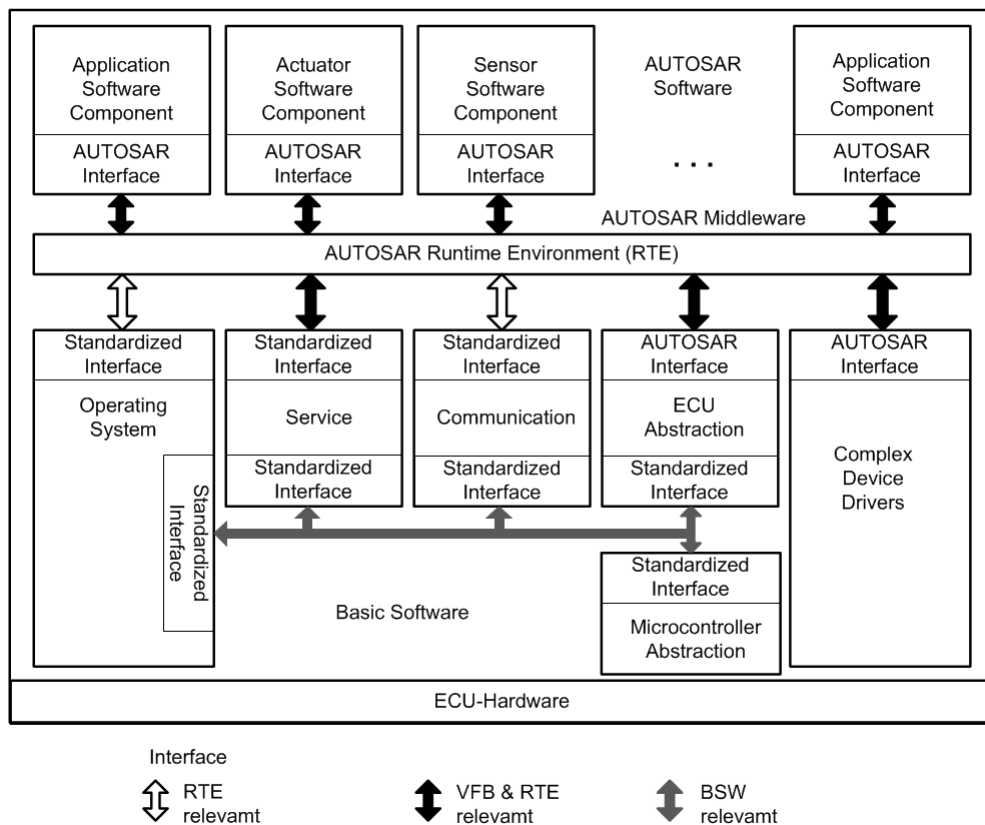


**Figure 5.4: AUTOSAR software architecture** - The AUTOSAR software components have well-defined interfaces, which are described using a standardized exchange format defined in AUTOSAR. An user application is decomposed and encapsulated in the respective AUTOSAR software components which run on the AUTOSAR infrastructure [AUTOSAR].

## 5. ADAS SYSTEM MODELING CONCEPT

---

schemes, standard functions (API), data exchange format, etc. There are companies in the automotive industry attempting to standardize the system design for ADAS or facilitate the formation of ADAS standards. A bold example is the joint work of BASELABS and Vector, where modular data fusion software components [BASELABS] and a framework for ADAS applications [vADASdeveloper] have been seamlessly integrated. It should be noted that BASELABS modules are design as open as possible, thus, not counting on any specific runtime environment (e.g., AUTOSAR). However, these modules can be adapted to an AUTOSAR environment if it is needed.

**ISO 26262 functional safety in system design considerations:** Since the year 2011, ISO 26262 functional safety standard provides the guidance for the automotive industry and has been extensively accepted throughout the automotive community. Although governments have not yet issued an mandate of the standard to fulfill the challenging safety requirements of ADAS and other automotive E/E systems, ISO 26262 compliance is deemed to be an internal mandate by automotive industry leaders including some OEMs, Tier-1s, and Tier-2s [Hoo15].

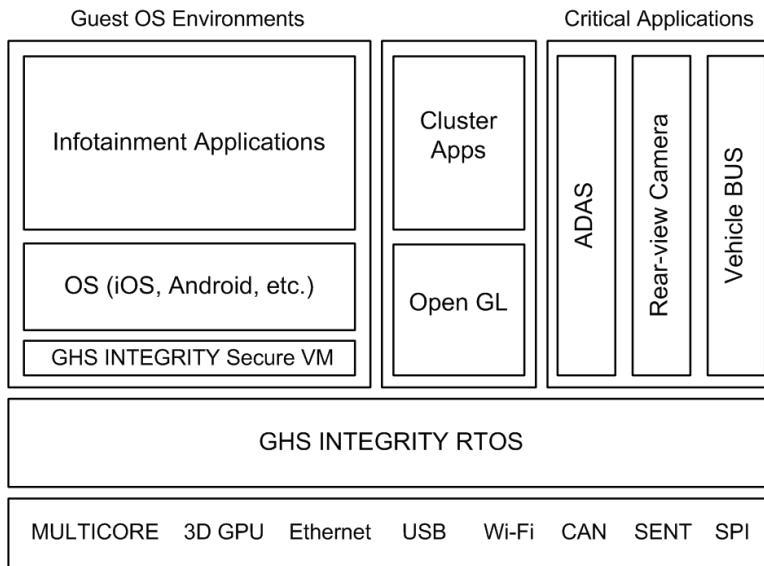


**Figure 5.5: ADAS on multicore system** - ADAS subsystems and non-critical partitions consolidated on a multicore processor based on Green Hills (GHS) INTEGRITY RTOS (real-time operating system) [Hoo15].

To meet ISO 26262 functional safety standard, the mind-set of safety design must be applied on various levels of system abstraction (see Fig. 5.5), especially by introduc-



ing diversified redundancy on the safety critical signal paths. For example, in ASIL-D compliant automotive Electric Power Steering (EPS) system, different torque sensors (e.g., optical and hall effect) can be employed via Serial Peripheral Interface (SPI) and Single Edge Nibble Transmission (SENT) respectively on the same (torque) signal path to the ECU for the torque measurement inputs. Such double sensory inputs enable the plausibility check by comparing one input against the other, and improve the robustness of torque measurements by applying redundancy in the design. Another example of diversified redundancy can be found in an ADAS system for collision avoidance. Radar and vision sensors in the ADAS jointly contribute to the object detection and tracking so as to assist driver to avoid potential collisions. Both sensors or sensor arrays work independently and can actually complement each other to help the system accommodate various environmental conditions and driving scenarios. The EPS system realizes the diversified redundancy on the sensor signal level, i.e., the same type of measurements provided by different torque sensors, while the above ADAS example establishes the diversified redundancy on the system function level - object detection and tracking employing different types of sensors and measurement principles. Such design decisions may fall due to different system design flows (e.g., top-down or bottom-up).

## 5.2 Sensor Fusion Algorithms

A multi-sensor system relies upon sensory inputs using diversified measurement principles (refer to Chap. 3 and 4). Multiple metrics need to be employed to fully characterize objects under inspection, because neither a single sensor nor an individual measurement system can fulfill the requirements. Thus, in order to benefit from the advantages of all the inspection systems for the evaluation, various testing and inspection methods should be used. The fusion of the acquired data facilitates the diminishment of uncertainty and the enhancement of signals. The combination with present measurement systems and advanced data processing methods can give a better evaluation outcome [ZFK07].

The JDL process model for sensor fusion, which was introduced by Joint Directors of Laboratories, is conceptualized by sensor inputs, human-computer interaction, database management, source preprocessing, and six key subprocesses: signal refinement, object refinement, situation refinement, significance estimation, process refine-

## 5. ADAS SYSTEM MODELING CONCEPT

ment, cognitive refinement [LHL08]. In other words, sensor fusion can be carried out at different abstraction levels, i.e., (raw) signal/data level, feature level, decision level.

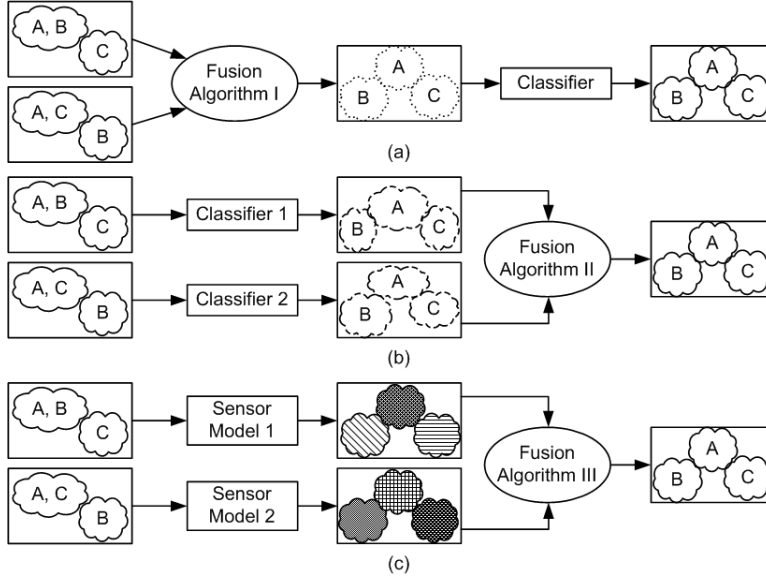


**Figure 5.6: Data fusion schemes** - (a) Feature integration; (b) Feature discrimination; (c) Feature discrimination [ZFK07].

The following typical sensor fusion schemes can be observed in practice. Fig. 5.6 showed that A, B and C are distinguished from each other by fusing sensors 1 and 2. The salient features from the two data sources are combined by the first type of data fusion (see Fig. 5.6(a)), while a higher level approach, i.e., decision or feature level, can use the second or third type of data fusion shown in Fig. 5.6(b) and Fig. 5.6(c) respectively. The preprocessing unit, which can be ANN, data clustering, segmentation algorithm, or other types of classifiers, are planned for the input sensor data. A thematic map can be generated afterwards through the preliminary results, which are fused by the probabilistic theory, fuzzy logic operator, or numerical combination. An alternative approach in terms of sensor modeling can be employed instead of using categorizing methods. Therefore, the sensor model can be built by implementing statistical methods through calibration, supervised, or unsupervised learning. The outputs are fused to generate the posterior probabilities by applying the Dempster–Shafer theory, Bayesian inference, or fuzzy logic method [ZFK07].

In the proposed conceptual ADAS system, sensor fusion can be performed in multi-sensing interfaces to refine the signal; it can be performed in the soft-computing sub-

system at feature level by applying feature selection and optimization techniques to enhance the salient features and increase the class separability in feature space; it can also be applied in driver-vehicle-interfaces at decision level to warn/assist the driver to make proper reaction.

### 5.3 Multiclass Classification Methods

Many real-world problems in the context of ADAS such as pedestrian detection, traffic sign recognition, driver drowsiness detection, automatic parking, etc. can be resolved based on classification systems. Classification methods aim to produce a mapping from inputs  $x$  to outputs  $y$ , given a labeled set of input-output pairs  $\mathcal{D} = \{(x_i, y_i)_{i=1}^N\}$ , where  $\mathcal{D}$  is the training set,  $y_i$  is a categorical variable from the finite set,  $y_i \in \{1, \dots, L\}$ , and  $N$  is the number of training examples. If  $L > 2$ , it is known as multiclass classification, while it is regarded as binary classification when  $L = 2$  [Mur12a].

#### 5.3.1 Artificial Neural Networks (ANNs)

Artificial Neural Networks (ANNs), in particular the Multilayer Perceptrons (MLP), are employed in order to classify instances that are also non linearly separable. In feed-forward ANNs, neurons are grouped into distinct layers as depicted in Fig. 5.7(a). Output of each layer is connected to input of nodes in the following layer. Using a number of output neurons and proper class designation, MLP can naturally address multiclass classification problem.

Inputs of the first layer (input layer) are the inputs to the network, while the outputs of the last layer form the outputs of the network. The input-output mapping is determined by the network, which is trained on a labeled set of input-output pairs. The weights of the connections between neurons are then fixed, and the network is used to determine the classifications of a new set of data. When the input and activation functions of the neurons as well as the network architecture are fixed, the current values of weights define the behavior of the ANN. For estimating the values of the weights, the back propagation algorithm is regarded as the most well-known and widely used learning algorithm [Kot07].

A two-layer feed-forward neural network with sigmoid hidden neurons and linear output neurons was employed in the research work to classify driver drowsiness levels.

## 5. ADAS SYSTEM MODELING CONCEPT

---

The details of the neural network with learning algorithms are described in Section 6.4.2. And the data evaluation results in application can be found in Section 7.4.

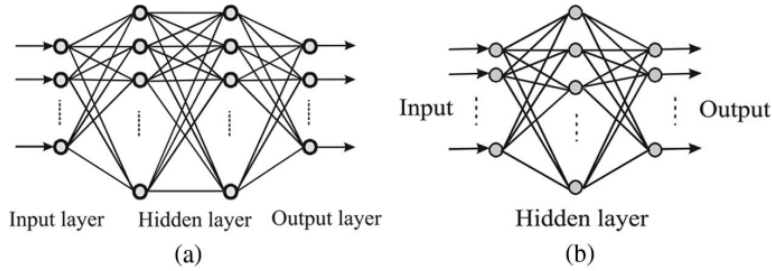


**Figure 5.7: Multilayer perceptrons and RBF** - (a) Multilayer perceptrons; (b) RBF network.

An RBF network is a three-layer feed-forward network as shown in Fig. 5.7(b), in which each hidden unit implements a radial activation function and the output of the network is a linear combination of radial basis functions of the inputs and neuron parameters. On the other hand, MLP may have one or more hidden layers. Both RBF and MLP are universal function approximators [Hay99a]. The difference between RBF networks and MLP lies in the activation functions in the hidden layers as well. MLP typically uses S-shaped sigmoid functions, as formulated in Eq. (5.1), in the hidden layers,

$$S(t) = \frac{1}{1 + e^{-t}} \quad (5.1)$$

while RBF uses the *multivariate Gaussian function* defined as follows in the hidden layers.

$$G(x, x_i) = \exp\left(-\frac{1}{2\sigma^2}\|x - x_i\|^2\right) \quad (5.2)$$

Here  $x_i$  denotes the center of the function and  $\sigma$  is known as the width. Eq. (5.2) is an example of a radial basis function, since it is only a function of *Euclidean norm* of the difference vector  $x - x_i$ , i.e.,  $\|x - x_i\|$  [Hay99b]. The selection of different ANNs for classification purposes depends on the shape of the class boundaries.

### 5.3.2 Support Vector Machines (SVMs)

As a supervised machine learning technique, Support Vector Machines [Vap95] are very popular. The basic SVMs support only binary classification. Given a set of training examples, each marked for belonging to one of two categories, SVM-based

learning algorithm constructs a hyperplane in a multidimensional space that separates given examples by maximizing the margin (large margin principle), i.e., the minimum distance from the separating hyperplane to the nearest example (see Fig. 5.8).

SVMs do not result in calibrated probabilistic outputs, which makes it difficult to use them in the multiclass classification setting [Mur12b]. However, extensions of SVMs such as [WW99] and [CS01] are proposed to solve this problem. Another approach to tackle multiclass classification, known as Hierarchical Support Vector Machine (HSVM), is to construct a decision tree with an SVM at each node that is used as binary classifier (see [CCG04] for details).

In addition to performing linear classification, SVMs can efficiently perform non-linear classification using kernel method, implicitly mapping their inputs into high-dimensional feature spaces. The SVM model complexity is not affected by the number of features contained in the training data, thus, SVMs are well suited to deal with learning tasks with large number of features with respect to the amount of training instances [Kot07].

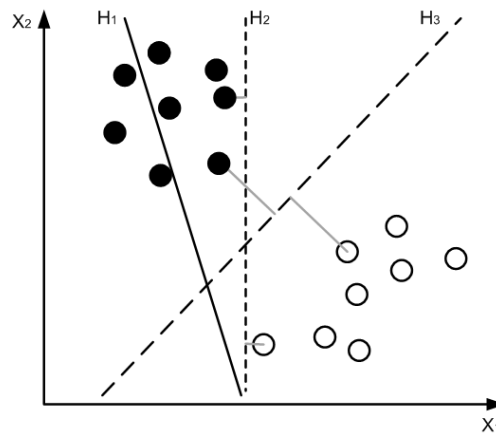


**Figure 5.8: SVM-based classification** - Hyperplane  $H_1$  does not separate the classes.  $H_2$  does, but only with a small margin.  $H_3$  separates them with the maximum margin.

Other effective methods for multiclass classification such as decision trees, k-Nearest Neighbor (KNN), Naive Bayes classifiers, etc., are not discussed here in details. It should be noted that the Bayesian Networks (BN) based method has been utilized in drowsiness detection by monitoring the physical behavior of the drivers [JLL06], and it has been shown that the BN is able to capture dynamics associated with fatigue [YMT09].

### 5.4 Summary and Discussion

The proposed JCS-based conceptual ADAS model can be partitioned in two parts. One is focused on the driver-based approach underlining the methods for driver monitoring, interior monitoring, driver-vehicle interactions, etc., surrounding the driver or any specific travel participants inside of the vehicle. In the other part, vehicle-based approach is pursued with respect to vehicle control, localization and navigation, collision avoidance, etc., centering around the vehicle and its interactions with transport infrastructures (V2X). The holistic design of ADAS covering these two parts remains as the major challenge of such complex systems (see Fig. 5.9). Industrial standards like AUTOSAR, ISO 26262, as well as XiL being highlighted in the above sections should be jointly considered and employed properly in the system design/validation processes.

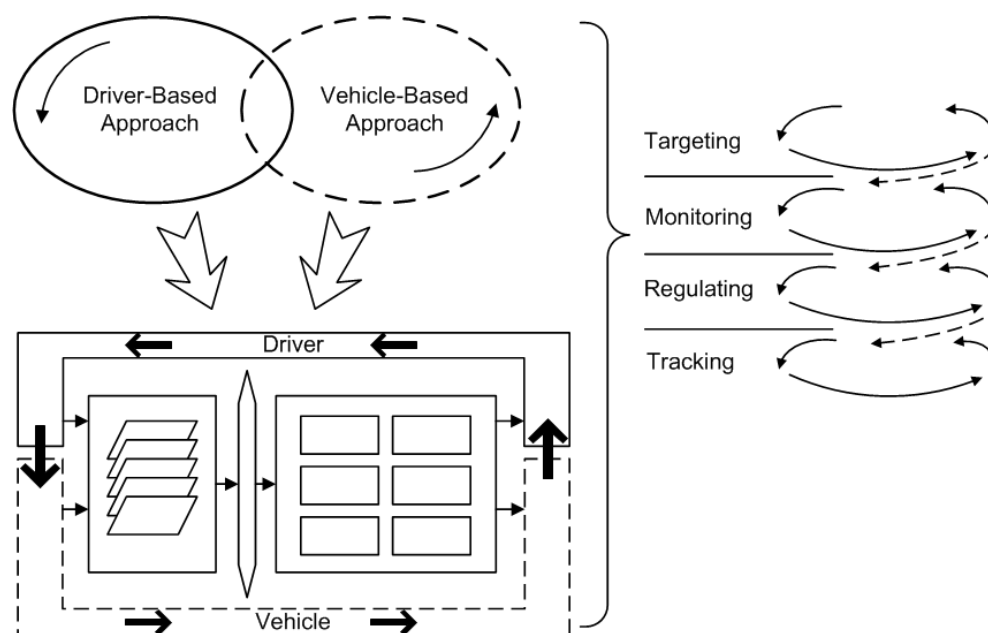


**Figure 5.9: Holistic design of ADAS** - Driver-based approach and vehicle-based approach jointly form a more comprehensive driver assistance system that can be mapped to one or several layers (typically tracking, regulating and monitoring) in the ECOM model.

## Chapter 6

# DeCaDrive: System Architecture and Implementation

Following the proposed system concept and model in Chapter 5, driver-based approach is employed in the DeCaDrive project aiming at driver status detection and intention prediction. The insight into system realization of DeCaDrive with respect to the evolution of system requirements, the relevant building blocks, as well as the design considerations and changes is given in this chapter. An overview of the implemented DeCaDrive system is given in Section 6.1 followed by its development history in Section 6.2. The system hardware and software components are described in Section 6.3 and 6.4 respectively. Finally, the system implementation is summarized with known limitations, possible improvements and new features in Section 6.5.

### 6.1 DeCaDrive System Architecture

Recalling the JCS system concept and the associated COCOM/ECOM model, the proposed intelligent system incorporating such processing pipeline that covers sensor signal acquisition, feature extraction/computation, feature selection and optimization, as well as learning and classification, positions itself in the *Monitoring* layer of the hierarchical control model - ECOM (see Fig. 2.3 and Fig. 5.9). The system block diagram in Fig. 6.1 gives an overview of the involved subsystems, functional building blocks, interfaces, and the associated operation environment (marked with dash lines) in the implemented DeCaDrive system. Instead of testing on a real vehicle, a simulated

## 6. DECADRIVE: SYSTEM ARCHITECTURE AND IMPLEMENTATION

---

driving environment is built and integrated in DeCaDrive for experiment and validation purposes.

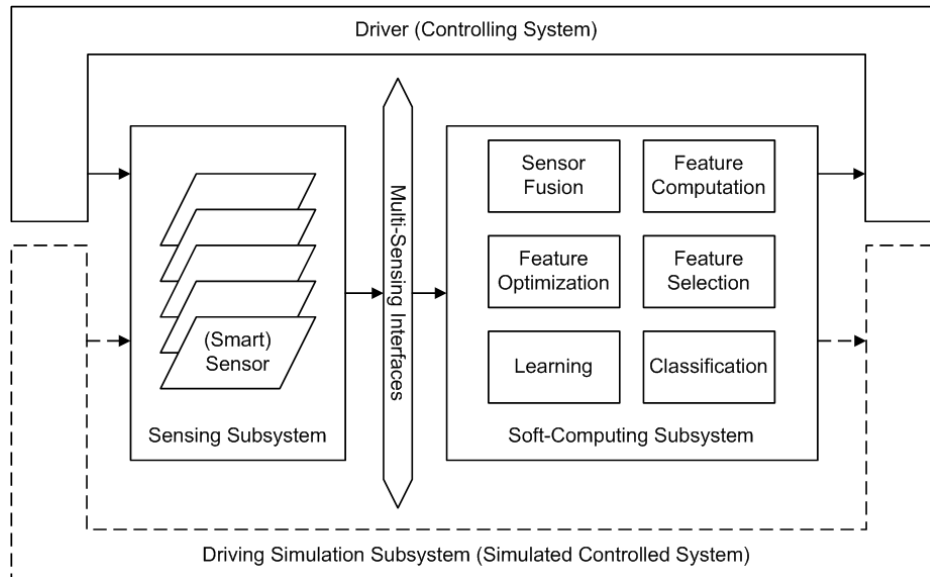


**Figure 6.1: DeCaDrive system concept** - The block diagram of the implemented system concept includes the relevant system components, interfaces and the operation environment.

To enable driver drowsiness detection that can be modeled as (multiclass) pattern classification, the DeCaDrive system to be viewed as JCS, can be partitioned in four subsystems, i.e., the sensing subsystem, the soft-computing subsystem, and the driving simulation subsystem (simulated controlled system) as well as driver (controlling system) as shown in Fig. 6.1. It should be noted that the driving performance metrics derived from vehicle dynamics, such as vehicle speed, acceleration, heading angle, etc., are not evaluated in the implemented DeCaDrive system. Hence, DeCaDrive belongs to the category of driver-based approaches for drowsy driver assistance, which has a different focus compared to the vehicle-based approaches.

The proposed sensing subsystem consists of steering angle sensor, pulse rate sensor, impedance spectroscopy sensor, so as to monitor the steering behavior, pulse rate, and skin impedance of driver respectively. As a key component the IR depth camera with active illumination, here the Kinect sensor, is integrated in order to reliably provide visual cues of driver including eye gaze estimation and blink detection as well as head



orientation and pose. In the soft-computing subsystem the feature computation, (feature) dimension reduction and optimization, as well as learning and classification in the processing pipeline are realized. In general a multi-sensor approach based on color and depth vision, vehicle driving data, and biomedical driver data with efficient sensor fusion and a learning system architecture has been pursued here to address driver status detection and intention prediction. The driving simulation subsystem is able to simulate different driving scenes for highway, city streets, country roads, etc., for various types of vehicles such as passenger cars, buses or trucks. The multi-sensing interfaces, which interconnect sensory components and the soft-computing subsystem, enable A/D conversion if needed, sensor data streaming, multi-sensor time-based synchronization. With scalable adaptive sensing interfaces the diversified (redundant) sensory inputs can be realized. Furthermore, if required the DeCaDrive system can be flexibly adapted to the respective driving simulation scenarios through the best suitable sensor configurations. For example, for a simulated truck driving in the night on highway, it would be requiring IR vision with depth sensing for better performance of driver status monitoring, since traditional vision sensors without active illumination won't help in this case. Pulse rate sensor would be especially needed when monitoring a driver with a history of heart disease to detect potential heart attacks.

## 6.2 DeCaDrive Development History

Initially the project was motivated by the novel IR depth sensing technology during the investigation and experiment on the proprietary DriMix Micro-3D-Camera (see Section 3.2.1). By that time, drowsy driving issues still remained unsolved, thus the idea about using depth and color sensing in driver status monitoring and drowsiness detection emerged. A low-cost commodity depth camera, the Kinect V1 sensor (by the time it was released), was firstly selected to serve the comparison study purpose, and it was finally taken into the system as the vision sensor component due to its availability, comprehensive features, and low cost. Thus, the system was originally designed based on a single IR depth camera with inspiration: **Depth-Camera-based Driver** status monitoring – DeCaDrive.

The validation results of *ISE EyeLoc demonstrator* based on the previous study in [LXK11, LXK12] unveiled the potential of IR depth camera in multi-user eye localiza-

## 6. DECADRIVE: SYSTEM ARCHITECTURE AND IMPLEMENTATION

---

tion/tracking applications, which laid the foundation of the first DeCaDrive prototype in early 2012. The sensory data was initially acquired by IR depth camera (depth and RGB outputs), pulse rate sensor, and steering angle sensor. The tactile sensor button on the steering wheel and the pressure sensors behind the throttle and brake pedals were considered as auxiliary inputs to the system, which generate additional information on the side of driving simulator.

To enhance the sensing capability and to study the relation of driver's skin impedance and drowsy state, DeCaDrive has been extended with embedded impedance spectroscopy, which has a novel embodiment integrated in the steering wheel.

The DeCaDrive system has finally evolved from Windows/C/MATLAB based implementation to C/C++/Python/Orange based multi-platform-compliant system that is capable of on-line data acquisition and classification. A demonstrator of DeCaDrive has been successfully presented on the International Motor Show – IAA Nutzfahrzeuge 2014 in Hannover, Germany.

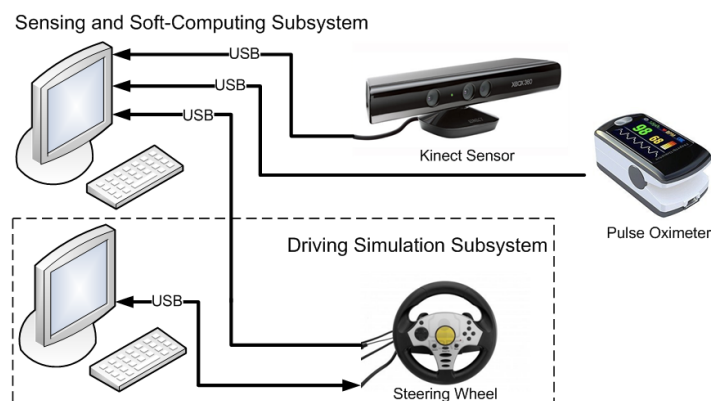


**Figure 6.2: DeCaDrive (the first version)** - The system overview of the first version of DeCaDrive: the sensing and soft-computing tasks are carried out in a merged subsystem in one PC; the simulated human-vehicle interfaces and the driving environment are realized in another PC [LWK12].

In the first version of DeCaDrive the implementation was mainly focused on Kinect-based face tracking and Kalman-filter based eye gaze estimation, as well as sensor fusion among Kinect, steering angle and pulse rate data. The implementation of the face tracking algorithm of Kinect provided in Windows SDK was optimized in DeCaDrive with multi-threads instead of single thread for both RGB and depth input data, i.e., one

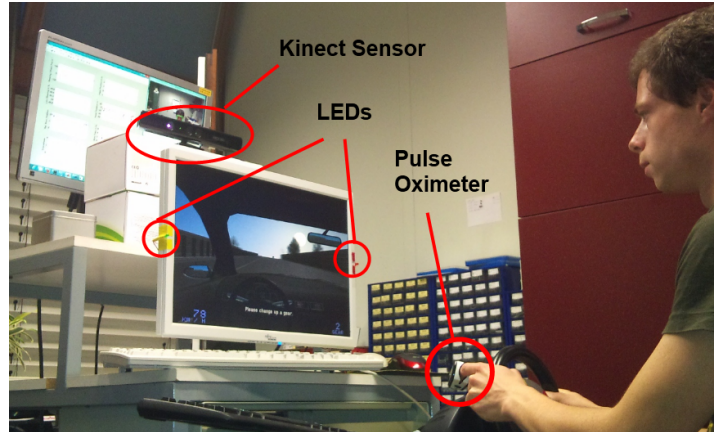


**Figure 6.3: DeCaDrive (the first demo)** - A test subject is operating the demonstrator of DeCaDrive [Wer12].

thread for RGB image processing and another thread for depth image processing. This method enables intrinsic synchronization/alignment between RGB and depth images by explicit control on both threads, especially when the frame rates of RGB and depth deviate from each other due to the disturbances on the Kinect sensor or the lack of computation resources [Wer12]. The system was constructed using two PCs: one for the sensing and soft-computing tasks, the other for the simulated driving environment as shown in Fig 6.2. An off-the-shelf PPG-based pulse oximeter was employed to collect the on-line sensory data of pulse rate and oximetry and record the data into file for later (off-line) use. As illustrated in Fig 6.3 the pulse oximeter was attached to the finger of test subject. The Kinect sensor was set on top of the screen, where the simulated driving environment was visualized. Two LEDs on each side of the screen were used to randomly generate stimulating light pulses to attract the attention from test subject, which can facilitate the evaluation of test subject's response time during driving simulation. The first graphic user interface (GUI) of DeCaDrive was developed based on MATLAB showing on-line technical computation of input sensory data (see the plots on the left side of Fig. 6.4) and face tracking, eye detection, eye gaze estimation results (see the right side of Fig. 6.4).

DeCaDrive was enhanced with embedded impedance spectroscopy for driver drowsiness detection afterwards. A novel embedded IS-sensor was designed and integrated on the steering wheel to monitor driver's (skin) impedance response in a non-invasive

## 6. DECADRIVE: SYSTEM ARCHITECTURE AND IMPLEMENTATION

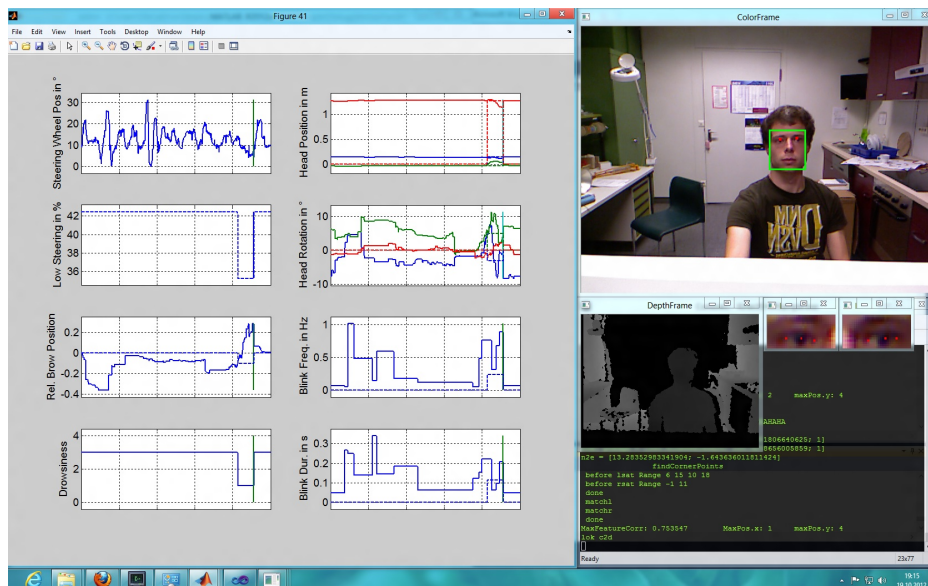


**Figure 6.4:** DeCaDrive GUI of the first demo - MATLAB-based GUI of DeCaDrive; left: the visualization of technical evaluation of sensory data; top right: test subject observed by the vision sensor; bottom right: real-time depth image, eye detection and gaze estimation [Wer12].

manner. As illustrated in Fig. 6.5, data links of various embedded sensors on steering wheel were channelized to a microcontroller based digital front-end, so as to establish scalable and adaptive multi-sensor interfaces. The IR depth camera, as a key component of the sensing subsystem, was connected via USB interface to the PC-based system back-end directly.

Finally, the system realization of DeCaDrive has been advanced towards higher flexibility, sensor feature optimization, as well as on-line recognition capability by migrating to ORANGE – a new open-access multi-platform environment [DCEG13], and by utilizing Support-Vector-Machine (SVM) based classifier [MMRT01]. The final system architecture with more computational intelligence is visualized in Fig. 6.6, which employs hierarchical classification and automated feature selection methods.

### 6.3 Hardware Components

DeCaDrive system originated from a prototype based on single depth camera and afterwards has evolved in so far to an intelligent system incorporating diversified embedded

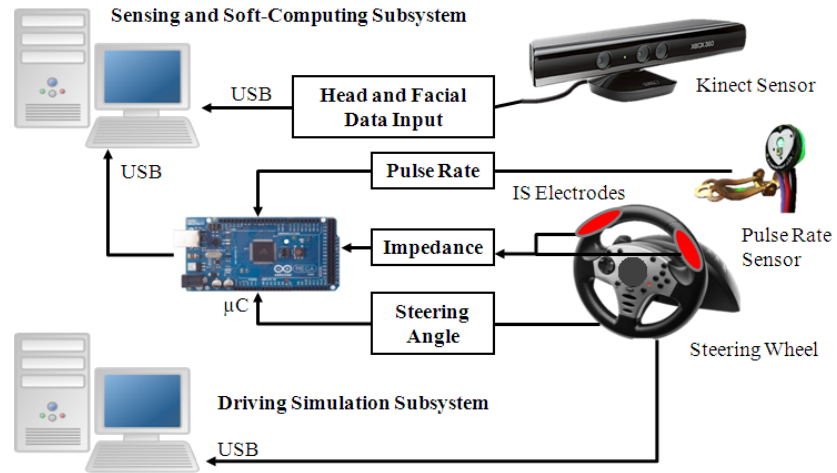


Figure 6.5: DeCaDrive with IS enhancement - The system overview of DeCaDrive with integrated IS-sensor and microcontroller based digital front-end [LBK13].

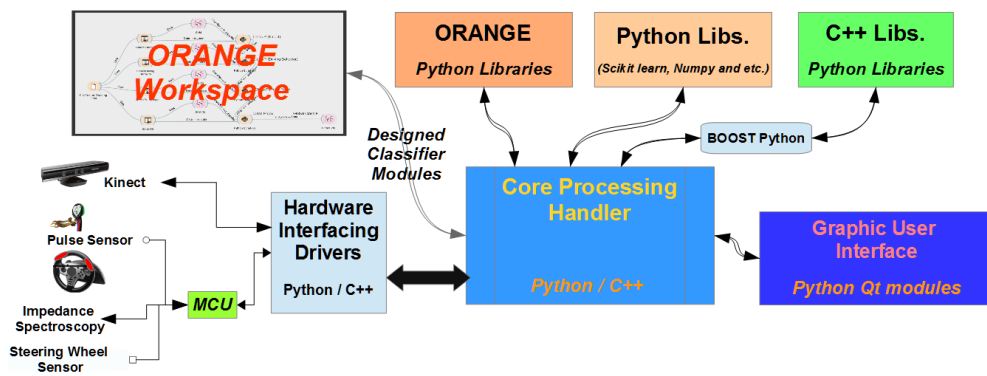
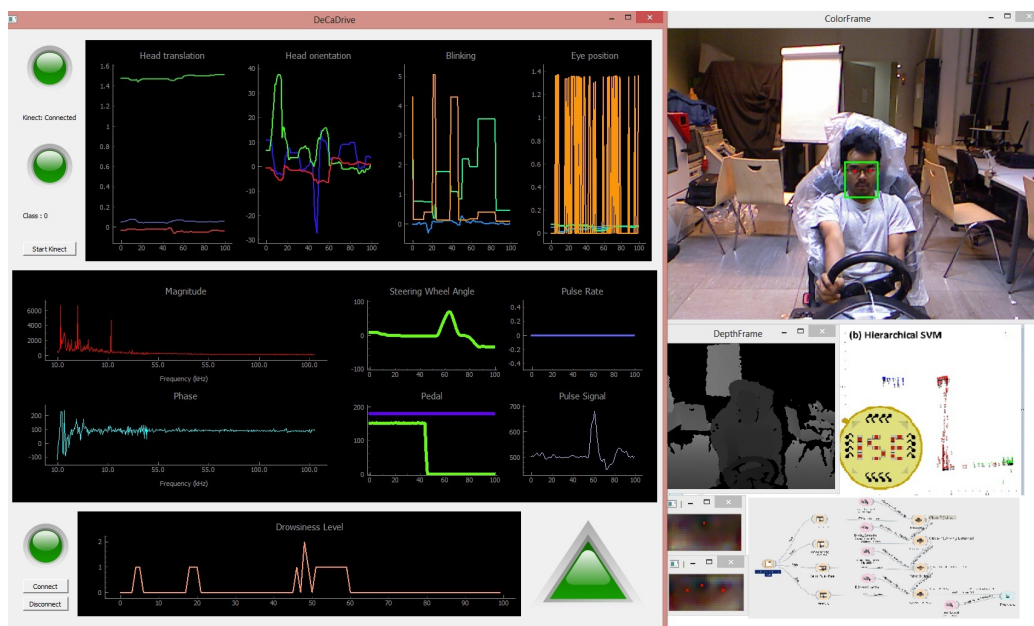


Figure 6.6: DeCaDrive (the final version) - The system architecture with the focus on the realization of sensing and soft-computing subsystems [LTK14].

## 6. DECADRIVE: SYSTEM ARCHITECTURE AND IMPLEMENTATION

---



**Figure 6.7:** DeCaDrive host application GUI - Left: the visualization of technical evaluation of sensory data was optimized, and switch buttons for sensor connection and system activation were made available on the GUI panel; top right: test subject observed by the vision sensor; bottom right: real-time depth image, eye detection and gaze estimation [LTK14].

sensors including IR depth camera, pulse rate sensor, blood oxygen saturation meter, steering angle sensor, tactile and pressure sensors, IS-sensor, and more in the future development. The analog and digital front-end, especially for the embedded IS-sensor, as well as the scalable adaptive multi-sensor interface are highlighted in this section.

### 6.3.1 Analog and Digital Front-End

In typical bioelectrical impedance analysis only the tissue impedance is of interest which is usually measured with tetra-polar electrode method (see Fig. 4.3(b)), or say, four-wire measurement configuration [Ivo03]. In DeCaDrive, for embedded impedance spectroscopy, a two-wire (bipolar electrode method in Fig. 4.3(a)) impedance measurement configuration is adopted, because not only tissue impedance but galvanic skin response (GSR) of driver are under research. And both measures can be used as indication of psychological or physiological arousal in driving simulation context. Fig. 6.8(a) illustrates two-wire configuration on a single hand where the tissue impedance of palm ( $Z_{TUS}$ ) is measured along with contact impedance at two electrode positions ( $Z_{k1}$  and  $Z_{k2}$ ). Two-wire impedance measurement configuration can be applied on two hands as well. The overall measured impedance  $Z$  is interpreted as follows

$$Z = \frac{U}{I} = Z_{k1} + Z_{TUS} + Z_{k2}, \quad (6.1)$$

when contact impedance of two electrodes are the same, e.g., using one-hand measurement as Fig. 6.8(a), where  $Z_{k1} \approx Z_{k2} = Z_k$ , Eq. (6.1) can be simplified to

$$Z = 2Z_k + Z_{TUS}. \quad (6.2)$$

As depicted in Fig. 6.8(c) the measurement signal path is from one electrode over the body (including arm and thorax impedance) to the other electrode; thus, it forms a two-wire measurement configuration with two hands.

For non-intrusive impedance measurement two dry electrodes made of flexible copper tape were embedded on the steering wheel at standard "ten to two" position. The electrodes are connected via the analog front-end to the impedance converter AD5933 as shown in the shield board on top of Arduino Mega 2560 microcontroller in Fig. 6.8(b), which operates from 10–100 kHz and covers the impedance range 0.1 k $\Omega$  – 10 M $\Omega$ . The microcontroller-based digital front-end communicates with the impedance converter via

## 6. DECADRIIVE: SYSTEM ARCHITECTURE AND IMPLEMENTATION

---

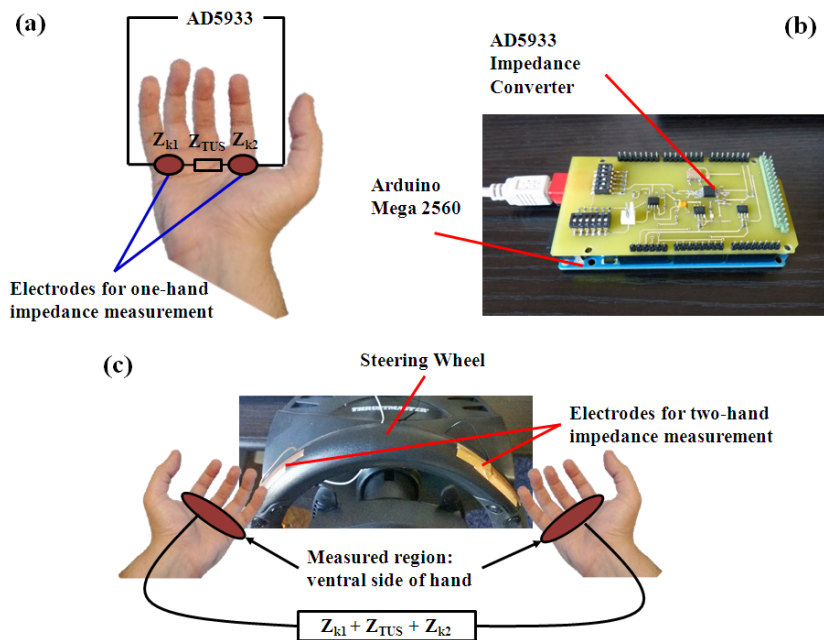


**Figure 6.8: Embedded IS-sensor in DeCaDrive** - (a) Two-wire configuration for one-hand impedance measurement; (b) the analog front-end (top shield board) of IS-sensor, and the microcontroller-based digital front-end (bottom Arduino board) of DeCaDrive; (c) two-wire configuration for two-hand impedance measurement [LBK13].



$I^2C$  link. A switch array of 12 ports were installed to realize a resistor network of high precision calibration and feedback resistors (tolerance  $\pm 0.05\%$ ) allowing a faster and easier calibration process. Due to the analog front-end the DC level on the signal path of impedance measurements remains constant, thus, the effects of electrode polarization can be minimized.

One-hand and two-hand measurement configurations can be combined in a proper manner to address different driving styles. With the embedded IS-sensor the system is able to detect whether the steering wheel is handled with a single hand or two hands in addition to monitoring the impedance response. Such information can be used in the context of driving scenario to facilitate the assessment of driving behavior of individuals.

The copper-based dry electrodes used in the early implementation of DeCaDrive are, however, facing the limitations such as higher contact impedance in general, low biocompatibility and weak corrosion resistance. Thus, in the final system the copper electrodes have been replaced by conductive textile electrodes which allow flexible adaptation of the electrodes on the steering wheel contour despite very high impedance ( $M\Omega$ ) of textile electrodes. Alternatively, medically safe materials like stainless steel or titanium can be considered for electrodes. These metal electrodes could be attached to a precisely fitting milling groove in the steering wheel.

The remaining issue of the current IS-sensor is less robustness against movement artefacts like hand contact loss or high contact pressure on the electrodes which directly affect the measurement results. On the other hand such movement artefacts, however, may indicate abnormal stress situations during driving, especially in conjunction with video cues and other sensory inputs, hence can be considered in the assessment of driving performance.

### 6.3.2 Scalable Adaptive Multi-Sensor Interface

The sensory components used in DeCaDrive are summarized in Table 6.1. There is a direct connection of Kinect sensor to the PC-based soft-computing subsystem via USB. Other sensory inputs are channelized to a microcontroller ( $\mu C$ ) based digital front-end. After preprocessing the sensor data are transferred via USB interface of the microcontroller to the soft-computing subsystem, where the sensor features are extracted and fused.

## 6. DECADRIVE: SYSTEM ARCHITECTURE AND IMPLEMENTATION

---

Analog to CAN interface for the interconnection of ECUs and on-board equipments, standardization of smart sensor interfaces is demanded for ADAS due to multi-rate heterogenous sensory data. In DeCaDrive, a preliminary scalable adaptive multi-sensor interface is established based on microcontroller and standard PC.

**Table 6.1:** Summary of sensory components used in DeCaDrive

Sensor	Output	Preprocessing	Sampling Rate	Interface
Kinect	Digital	In sensor	Up to 30 fps	USB on sensor
Steering angle sensor	Analog	$\mu C$	512 Hz	USB on $\mu C$
Pulse rate sensor	Analog	$\mu C$	512 Hz	USB on $\mu C$
IS-sensor	Digital	$\mu C$	512 Hz	USB on $\mu C$

### 6.4 Software Components

The software components used in DeCaDrive are mainly implemented in the soft-computing subsystem as shown in Fig. 6.1. From functional point of view, they can be categorized in the following groups.

- Sensor data preprocessing
- Sensor data synchronization
- Sensor fusion
- Feature computation and optimization
- Feature selection
- Learning and classification

An optimized face tracking is provided in Microsoft Kinect SDK, based on which head/eye tracking algorithm is adapted and utilized in this work. Fig. 6.9 gives examples of face/eye tracking results with overlapped CANDIDE-3 face model and in poor lighting condition.



**Figure 6.9: Kinect Face Tracking** - Face and eye tracking based on Kinect sensor, left to right, CANDIDE-3 face model in Kinect Face Tracking Demo [FaceTracking], face and eye tracking under poor illumination condition [Gua12].

Diversified sensory components and sophisticated algorithms make the system scalable and adaptive to different driving profiles and scenarios. Multi-rate data sets of complementary sensors are synchronized on the same time base before being processed by the feature computation and other relevant software components.

#### 6.4.1 Sensor Feature Computation

The complete sensor feature set being extracted from various sensor inputs of DeCaDrive is summarized in Table 6.2.

**Steering angle sensor features:** The features computed from steering angle sensor data are described as follows.

- Steering reversals being related to micro-corrections indicate the frequency of lateral motion changes (left-right or right-left) within gap size  $\theta$ . Depending on  $\theta$  two features are taken into evaluation, i.e., Feature 1 and 3 in Table 6.2 with  $\theta = 1^\circ$  and  $\theta = 3^\circ$  respectively.
- Steering-same-side represents the frequency of steering motion in the same direction above threshold  $\vartheta$  which indicates lane changing or curve turning movements. Feature 2 and 4 in Table 6.2 are computed based on  $\vartheta = 12^\circ$  and  $\vartheta = 32^\circ$  respectively.

## 6. DECADRIVE: SYSTEM ARCHITECTURE AND IMPLEMENTATION

**Table 6.2:** List of features being computed from multiple sensor measurements

Feature	Sensor	Description	Feature	Sensor	Description
1, 3	Steer Wheel	Steering Reversals 1°, 3°	34, 35	Kinect	Translation, Rotation Speed
2, 4	Steer Wheel	Steering SameSide 12°, 32°	36	Kinect	Mean Eyebrow Position
5	Steer Wheel	Std of Position	37, 38	Kinect	Mean Blink Frequency, Duration
6	Steer Wheel	Low Steering Percentage	39	Pulse Rate	LF/HF
7	Steer Wheel	Mean of Absolute Position	40	Pulse Rate	Mean Pulse Rate
8	Steer Wheel	Steering Velocity	41, 42	IS	Mean of Magnitude, Phase
9-11	Steer Wheel	FFT-LowBand, -MidBand, -HighBand	43, 44	IS	Std of Magnitude, Phase
12-14	Kinect	Mean x-, y-,z-Head Position	45, 46	IS	Lin. fit coeff. of magnitude
15-17	Kinect	Pitch-, Yaw-, Roll-Head Orientation	47, 48	IS	Exp. fit coeff. of magnitude
18-21	Kinect	x-, y-, z-, Norm-FFT-LowBand	49-51	IS	Poly. fit coeff. of magnitude
22-25	Kinect	x-, y-, z-, Norm-FFT-HighBand	52, 53	IS	Lin. fit coeff. of phase
26-29	Kinect	Pitch-, Yaw-, Roll-, Norm-FFT-LowBand	54, 55	IS	Exp. fit coeff. of phase
30-33	Kinect	Pitch-, Yaw-, Roll-, Norm-FFT-HighBand	56-58	IS	Poly. fit coeff. of phase

- Feature 5 and 7 reflect mean and standard deviation of steering wheel positions within a measurement time frame.
- Feature 6 gives the percentage of micro-corrections being taken to the overall steering motion.
- Feature 8 represents the steering velocity.
- Feature 9 to 11 are frequency domain analysis of steering statistics based on FFT.

Parameters for feature computation are dependent on the steering wheel specification (e.g., wheel size, sensor resolution, etc.) and system setup.

**Kinect sensor features:** Various visual clues including head movement, eye gaze direction and ocular measures are extracted from the data provided by the Kinect sensor. The following features are used in DeCaDrive:

- Mean head position in 3D coordinate system of Kinect within a measurement time frame (see Feature 12 to 14 in Table 6.2);
- Mean head orientation measures, i.e., pitch, yaw and roll (Feature 15 to 17);
- Frequency domain analysis for head translation on three axes and its Euclidean norm based on FFT LowBand (Feature 18 to 21) and FFT HighBand (Feature 22 to 25);
- Frequency domain analysis for head rotation around three axes and its Euclidean norm based on FFT LowBand (Feature 26 to 29) and FFT HighBand (Feature 30 to 33);
- Translation speed (Feature 34) and rotation speed (Feature 35);
- Mean of eyebrow positions relative to left and right eyes (Feature 36);
- Mean eye blink frequency (Feature 37) and blink duration (Feature 38).

It should be noted that based on the outcome of eye tracking process the eye pupil and corners are further detected to estimate the gaze direction using a modified algorithm from [MZ00] in Werber’s work [Wer12] for DeCaDrive. The estimated gaze direction is evaluated for the purpose of driver intention prediction. The potential features associated with eye gaze direction are, however, not evaluated for driver drowsiness detection.

**Pulse rate sensor features:** With predefined low frequency band 0.04 – 0.15 Hz (LF) and high frequency band 0.15 – 0.4 Hz (HF) the LF/HF ratio of pulse rate course within a measurement time frame is computed in Feature 39. The mean pulse rate is provided by Feature 40.

**IS-sensor features:** Linear, exponential and polynomial regression analysis are performed on IS-sensor data in evaluation window. Considering the goodness of fit

## 6. DECADRIVE: SYSTEM ARCHITECTURE AND IMPLEMENTATION

---

of regression model (refer to R-squared value in Fig. 6.10) IS-sensor data including magnitude and phase angle is modeled as second-order polynomial in each evaluation window for feature computation. The IS-sensor features being extracted in the first cut implementation are summarized as follows.

- Feature 41, 42: mean values of magnitude and phase angle
- Feature 43, 44: standard deviations of magnitude and phase angle
- Feature 45, 46: linear fit coefficients of magnitude
- Feature 47, 48: exponential fit coefficients of magnitude
- Feature 49, 50, 51: coefficients of quadratic polynomial fit to magnitude
- Feature 52, 53: linear fit coefficients of phase angle
- Feature 54, 55: exponential fit coefficients of phase angle
- Feature 56, 57, 58: coefficients of quadratic polynomial fit to phase angle

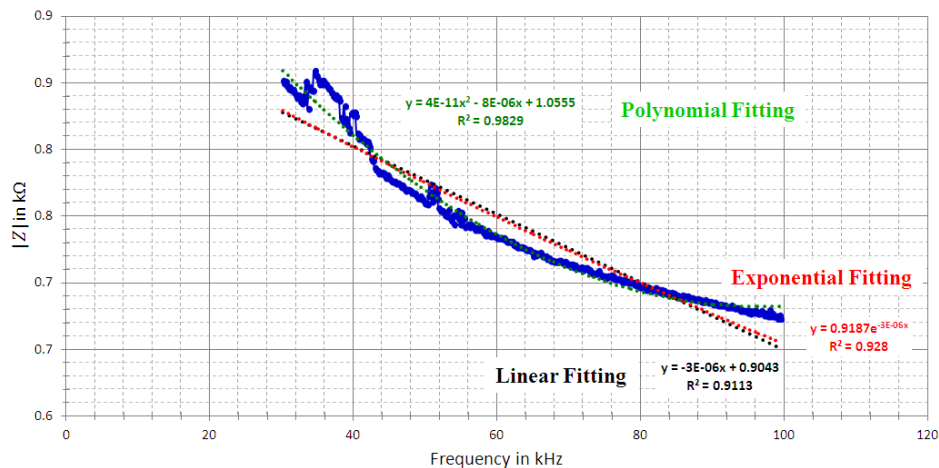


**Figure 6.10: IS-sensor features** - Linear, exponential, polynomial regression analysis on IS-sensor data in evaluation window with frequency sweep from 30 – 100 kHz [LBK13].

For correct off-line IS-data analysis the user has to make sure that the first value of the measurement data matrix starts exactly with the IS start frequency (30 kHz in this case). The duration of each frequency sweep of the IS-sensor is configured as one evaluation time window (512 data samples), hence IS data sets can be aligned with

Kinect data sets. Data sets of different sensors are synchronized on the same time base and fused on the feature level for pattern classification process. Different features are treated equally in the current DeCaDrive system, even though a proper weighting scheme can be applied.

In order to synchronize IS-sensor with other embedded sensors in system the time base and data evaluation time frame being used during system runtime have been streamlined by referring to Kinect sensor time base and taking least common multiple of respective sensor evaluation time frames.

Due to different driving styles, physiological conditions, etc., the dynamic range and variation of sensor data differ significantly among individual test subjects. In order to consolidate sensor features of respective test subjects feature vectors are normalized based on global mean and standard deviation as described in Eq. 6.3,

$$\vec{D}_{k,T,norm} = \frac{\vec{D}_{k,T,orig} - \mu_{k,T}}{\sigma_{k,T}}, \quad (6.3)$$

where  $\vec{D}_{k,T,norm}$  is the normalized feature vector of test subject T for specific sensor feature k,  $\vec{D}_{k,T,orig}$  is the corresponding original feature vector,  $\mu_{k,T}$  and  $\sigma_{k,T}$  are mean value and standard deviation of  $\vec{D}_{k,T,orig}$  respectively [Wer12].

### 6.4.2 Learning and Classification

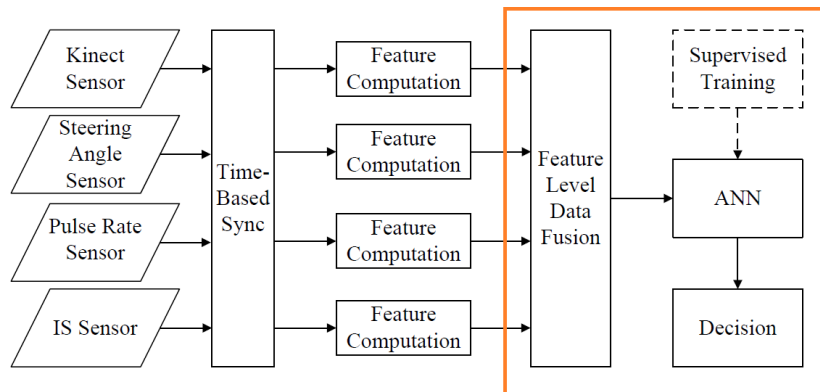


Figure 6.11: DeCaDrive data flow - Overview of the data processing flow.

**Off-Line Version – Windows/C/C++/MATLAB-based approach:** The driver drowsiness detection is modeled as a three-class pattern classification problem

## 6. DECADRIVE: SYSTEM ARCHITECTURE AND IMPLEMENTATION

---

in DeCaDrive, i.e., 1 – not drowsy (alert), 2 – a little drowsy (transition) and 3 – deep drowsy (fatigue). In the initial version, DeCaDrive was able to collect data from all the sensor inputs, however, the implemented classifier cannot process data in real-time to estimate the drowsiness states due to the limitations in software components. Thus, it is referred here as the off-line version of DeCaDrive.

As illustrated in Fig. 6.11, in the information processing architecture of DeCaDrive, the sensory data is collected from IR depth vision, steering angle, pulse rate, (skin) impedance measurements, and fused on the feature level afterwards. Based on the outcome of feature computation in the previous processing stage, the data sets are fused on the feature level to construct the input vectors, which are further optimized with regard to dimensionality reduction by employing feature selection techniques, for learning and classification procedures. Due to advantage of learning complex, nonlinear, high-dimensional patterns the classifier being used in DeCaDrive is built upon artificial neural network (ANN) or, more particularly, multilayer perceptrons (MLP) with supervised training procedures. Two learning algorithms have been evaluated here, i.e., scaled conjugate gradient algorithm (SCG) [MM93] and Levenberg-Marquardt algorithm (LM) [Mor77]. The developed approach to driver drowsiness detection is confirmed in the experimental results using multifold cross-validation.

In the first-cut implementation of DeCaDrive, the feature – driver drowsiness detection was realized based on a hybrid solution with MATLAB-scripting and C/C++ programming. Kinect sensor data acquisition and preprocessing was implemented in C++ code. It has been further combined with C-code-based data processing algorithms running on the microcontroller for the other sensor components in DeCaDrive. Sensor fusion, feature computation, as well as learning and classification procedures are realized in MATLAB code executed in the Windows PC-based soft-computing subsystem.

### **On-Line Version – C/C++/Python/Orange-based approach:**

It is aimed to achieve an effective Automated Feature Selection (AFS) as well as a robust on-line classification system. The proposed approach is based on a multiplatform flexible and open system, with on-line classification capability, which is provided by the Python-based signal processing and computation intelligent libraries as well as, ORANGE, an open source python based machine learning software through visual programming.



The on-line version of the system was implemented jointly utilizing the Python scripting in ORANGE and the heuristic DeCaDrive runtime modules which were developed previously. For example, the *Serial Port Interface* module communicates with the DeCaDrive sensing device using USB interface connection to control acquisition activity and import acquired data to store in ORANGE's data structure. The *Feature Selector* module allows user to manually filter data in term of sensory channels, e.g., pulse rate, steering angle, Kinect features and skin impedance in the design process. The *pattern classification* module analyzes multi-sensory context from the DeCaDrive data acquisition system to on-line determine the driver status. These effective modules developed in C/C++ were further improved by using BOOST for Python [AGK03] in the final DeCaDrive system.

The standard SVM classification technique was employed in DeCaDrive to validate the approach of flat/single SVM based feature-level sensor fusion together with the AFS option. In addition, inspired by HSVM (see Section 5.3.2), an effective multi-channel hierarchical SVM approach (here H-SVM to be distinguished from HSVM) [TK14] was applied here to realize a more powerful and robust classification. H-SVM consists of multiple SVM classifiers with soft output in the first level processing stage and one additional SVM classifier at the final stage, so as to produce class probability (class-P) vectors corresponding to the probabilistic patterns of different classes (see Fig. 6.12). Each SVM classifier in the first level stage of H-SVM locally and individually computes a specific sensor (feature) channel to generate a class-P vector corresponding to different classes (not drowsy, little drowsy, deep drowsy). Here, SVM is not used as a binary classifier, but a classifier being able to address multiclass setting. The SVM classifier at the final stage computes the global class-P vector, the concatenation of class-P vector from all sensor channels, to produce the final class output.

To generate an optimum SVM model, two parameters,  $C$  which controls the error penalty of non-separable data points, and  $\gamma$  of the Radial Basis Function (RBF) kernel, are recommended to be appropriately defined with regard to the input data. In general, the SVM optimum parameters searching procedure takes place in the training step based on the training data sets only. In DeCaDrive the SVM automated parameters search option implemented in ORANGE with grid search and cross-validation techniques is employed. The respective SVM parameters are individually determined for each of the investigated feature channel SVMs and for the final SVM.

## 6. DECADRIVE: SYSTEM ARCHITECTURE AND IMPLEMENTATION

---

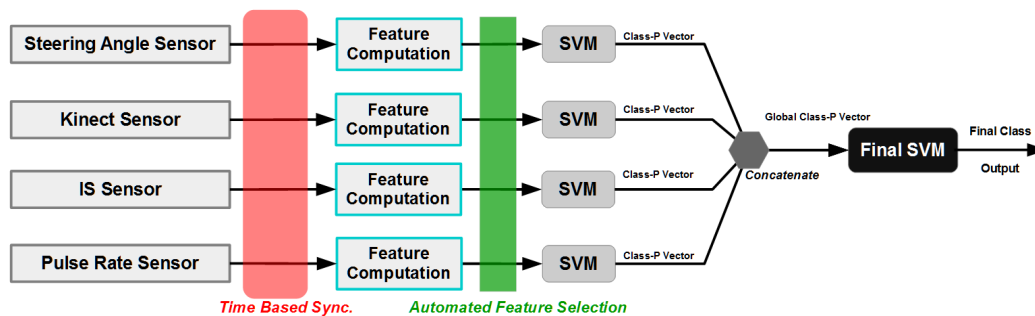


Figure 6.12: Hierarchical classification in DeCaDrive - Overview of the extended DeCaDrive system with hierarchical processing using H-SVM [LTK14].

### 6.5 Summary and Discussion

In order to investigate human driving behavior and to monitor vital signs of driver simultaneously a prototype of driving simulator was built. Initially the system was based on a single depth camera (**Depth-Camera-based Driver-state monitoring**) and afterwards has evolved to a multi-sensor soft-computing system encompassing PC-based driving simulation and diversified sensing interfaces including IR depth camera, PPG-based blood oxygen saturation meter with integrated pulse rate sensor, steering angle sensor, tactile sensor and pressure sensor. The initial version of DeCaDrive, which was published in [LWK12] and carried out within Werber's diploma thesis [Wer12], received the annual award of the Pfalzmetall foundation 2013 (Preis der Stiftung Pfalzmetall 2013) [PfalzMetall13].

The possible new features of DeCaDrive and its future development considerations are listed as follows.

- The runtime environment can be enhanced to store the sensory data for off-line use, comparative study, and can replay the recorded data for simulation purposes.
- Bioelectrical impedance with tetrapolar electrode method should be considered to further investigate driving impairments such as inebriation.
- To integrate the embedded IS-sensor together with PPG-based pulse rate sensor to realize a more elegant and compact embodiment.
- To improve the embedded IS-sensor to support both one-hand and two-hand configurations on the steering wheel, so that the system can adaptively evaluate

the IS-sensor inputs in continuously changing driving styles.

- Context by tactile sensor and pressure sensors is also useful to avoid spurious readings of the skin impedance during absence of one or both hands from the steering wheel.
- EEG-based methods (e.g., brain-computer interface described in Section 4.3.1) can be used as in sleep research to get a better, somehow invasive, determination of the ground truth for DeCaDrive.
- To fuse the driver's data with the measurements of vehicle dynamics such as brake and throttle information - a combination of driver- and vehicle-based approaches.
- The sensing and soft-computing subsystems can be merged/unified in an embedded solution for future on-board equipments in vehicle. Advanced integration of the key components and IPs into a single SoC-based solution can be pursued.

In the presented DeCaDrive implementation the sensor interfaces to soft-computing subsystem are USB ports, mainly due to the PC-based architecture. In the order of a seamless integration of DeCaDrive into the mainstream ECU-based ADAS architecture, the following considerations and adaptations are required:

- Sensing and soft-computing subsystems shall be miniaturized and further integrated by migrating from PC to embedded computing systems, e.g., high performance feature-rich microcontroller, FPGA, SoC or a combination thereof. Thus, both physical and energy footprint can be significantly reduced and yield a more cost-effective system solution, which is conclusive for automotive mass market.
- System architecture shall be further optimized to realize modular design at different levels of abstraction following automotive standards such as AUTOSAR.
- Inter-system communication link shall be using state-of-the-art automotive networking technologies such as CAN, CAN-FD (flexible data rate with higher bandwidth), LIN, FlexRay, MOST, Ethernet. Due to demand on high communication bandwidth, Ethernet is of particular interest for ADAS related applications. The interconnection with existing automotive (sub)systems is crucial for emerging

## 6. DECADRIVE: SYSTEM ARCHITECTURE AND IMPLEMENTATION

---

novel ADAS systems with respect to functionality, extendability and compatibility. Using compatible communication links can facilitate the extensive fusion of sensory data generated by various automotive components/systems. Thus, it may further improve the validity and efficiency of DeCaDrive.

- Functional safety (ISO 26262) compliant design/development shall be adopted for the integration of such ADAS system in mass-produced vehicles.
- Elegant expansion of human-vehicle interfaces can be realized with the improved ergonomic designs of embedded sensory components in DeCaDrive.

## Chapter 7

# Experimental Work

The system validation and experimental results are discussed in this chapter with the focus on the design of experiments addressed in Section 7.1, the simulated driving environment in Section 7.2, the ground truth definition in Section 7.3, as well as the evaluation/validation results in Section 7.4. In the end, the chapter is finalized with summary and discussion in Section 7.5.

### 7.1 Design of Experiments

To validate the DeCaDrive system for driver status monitoring, in particular, for driver drowsiness detection purpose, an experiment with a set of simulated driving tests has been designed and carried out as follows.

- Five test subjects volunteered to participate in an experiment with simulated driving environment under room temperature (20 to 25 degrees Celcius).
- All test subjects are male with average age of 28 ( $\pm 3$ ) years old. One participant is not in possession of driving license while the other four drive regularly and have 7 to 12 years of driving experience.
- The test subjects were instructed in advance to follow their normal daily routine and to avoid taking any stimulating substances (coffee, caffeine, etc.) before the experiment.

## 7. EXPERIMENTAL WORK

---

- The sensory components were calibrated properly before the experiment. The dry electrodes of IS-sensor on the steering wheel were finely prepared each time before a test subject started with driving simulation.
- A monotonous driving scenario (highway with low traffic density at daytime) was chosen for the experiment in order to promote driver drowsiness. The duration of driving session for each test subject was limited to 60 minutes. The speed limit in driving simulation for the experiment is up to 100 km/h.
- To minimize driving style dependent influence on IS-sensor inputs all test subjects performed two-hand driving operations with proper skin-electrode contact areas. It was ensured that the embedded pulse rate sensor on steering wheel was touched properly by test subjects during driving simulation.
- In early phase of each test (2 to 5 minutes from the beginning) the measured impedance was biased due to temporal changes of dry electrode-skin interface (electrolyte diffusion process). As a result, IS-sensor data of early phase was excluded from data evaluation process.
- Despite that sensor data evaluation can be performed during system runtime, all the sensor measurements of driving simulation were time-based synchronized and recorded in files for later off-line analysis.

### 7.2 Simulated Driving Environment

As visualized in Fig. 7.1 the simulated driving environment consists of a real-size driver seat, steering wheel with support stand, brake and throttle pedals, as well as a standard PC with 22-inch computer monitor showing the front view of driver (later it has been replaced by a 55-inch LCD TV panel in the DeCaDrive demonstrator prepared for IAA Nutzfahrzeuge 2014). Before conducting the experiment the test subjects were instructed to spend some time and get themselves familiar with the simulated driving environment.

Based on a PC software (see Fig. 7.2) different driving scenes for highway, city streets, country roads, etc. can be simulated for a typical passenger car. Other environmental factors such as weather, light conditions can be simulated in the driving

## 7.2 Simulated Driving Environment

---



**Figure 7.1: DeCaDrive demonstrator** - The simulated driving environment of DeCaDrive (the final version).



**Figure 7.2: Driving Simulator 2011** - A simulated driving scene of the city streets.

## 7. EXPERIMENTAL WORK

---

scene as well. As mentioned in Section 7.1 a monotonous driving task in the simulation software, i.e., highway driving at daytime with very few traffics, was chosen and performed by the test subjects in the experiments. Software packages aimed at e.g. bus or truck driving simulations can be adopted in DeCaDrive as well to extend the supported driving profiles.

### 7.3 Ground Truth Definition

To detect and classify driver drowsiness level, the ground truth (GT), or say, the target class of drowsiness level is defined with three-class scale: 1 – not drowsy (alert), 2 – a little drowsy (transition) and 3 – deep drowsy (fatigue).

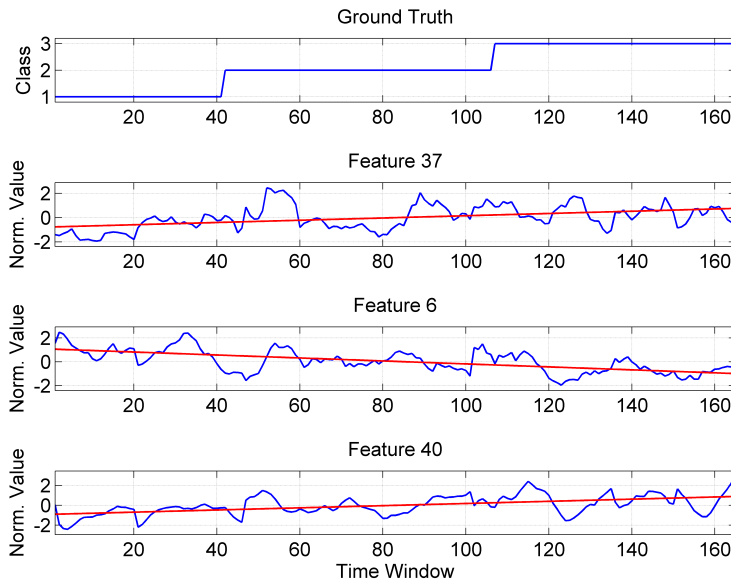


**Figure 7.3: Ground truth and extracted features** - a) Ground truth; b) blink frequency (Feature 37 in Table 6.2); c) low steering percentage (Feature 6); d) mean pulse rate (Feature 40) [LWK12].

Initially, two criteria, i.e., self-rated score (subjective) and measured response time (objective) are combined to assess the drowsiness level and to establish the ground truth (see Fig.7.3). In the experiment the test subjects were asked to rate their subjective sleepiness every 10 minutes based on the predefined three-class scale. In the early



implementation of DeCaDrive, a green and a red LED were mounted on the left and right side of the monitor respectively (see Fig. 6.3) for the purpose of driver response time measurements. Two LEDs were turned on in a random order and on a randomly generated time base. It was expected that the test subject will press the corresponding button on steering wheel as soon as he notices the light-up of the green or red LED, so that the LED can be turned off, thus, the next round of random light-up procedure can be triggered. The response time of the test subject during driving simulation was measured as the elapsed time from light-up to turn-off of the LED.

In practice, however, according to the feedback of test subjects and the preliminary measurement results of response time, it was observed that all test subjects were more reactive to the red LED compared to the green one. This led to biased measurement results of the response time on green LED. In addition, the correlation between self-rated drowsiness level and the one derived from the response time is still under investigation and yet to be concluded. In many cases, two independent methods result in discrepancies in the estimated drowsiness level.

A modified Karolinska-Scale (KSS) ranging from 1 (very alert) to 9.5 (fighting sleep) was investigated in the DeCaDrive project as an alternative assessment method for the ground truth definition of driver drowsiness. As shown in Fig. 7.4a a general trend of steering wheel movement which reflects the driving scenario characteristics can be computed based on the moving average of steering angle data. The skin impedance of approx.  $0.9\text{ k}\Omega$  with 30 kHz measurement frequency is evaluated here (see Fig. 7.4b). The features extracted from the steering angle sensor and the IS-sensor are compared against the KSS scores estimated by the test subjects every five minutes during the simulated driving tests. However, KSS-based self-estimation is even more complex than the three-class scale, thus, requires more expertise in the state estimation of test subjects.

Finally, to improve the self-rating accuracy of drowsiness level estimation based on the three-class scale, additive ratings made by an independent observer/assessor are evaluated along with the self-estimated scores. This approach to ground truth definition is used in the final DeCaDrive system.

## 7. EXPERIMENTAL WORK

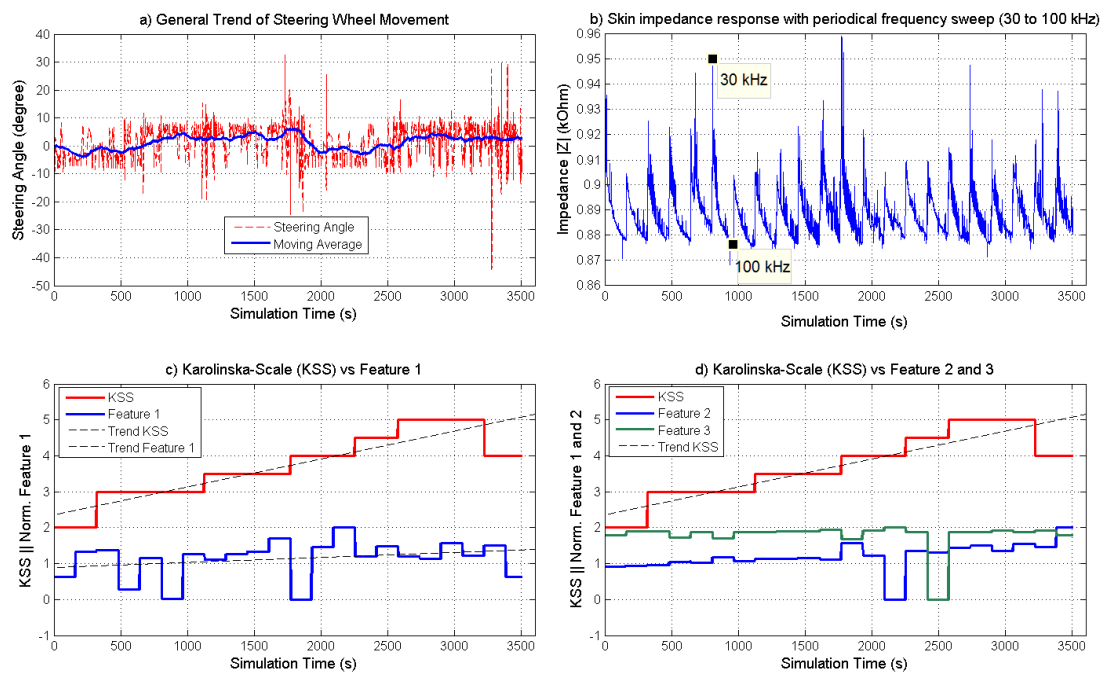


**Figure 7.4: Alternative method for ground truth definition - Data evaluation against the ground truth definition:** a) steering angle and its general trend; b) skin impedance with with periodical frequency sweep from 30 kHz to 100 kHz; c) self-estimated KSS vs feature 1 (the slope coefficient of linear regression on steering angle sensor data); d) self-estimated KSS vs feature 2 and 3 (exponential fit coefficients of IS magnitude).

## 7.4 Data Evaluation and System Validation

The sensory data of 353 time frames/windows with approximately 100-second measurement time per window are evaluated in the experiments. Each measurement consists of multiple sensor inputs including steering angle measures, head movement, ocular measures and pulse rate values.

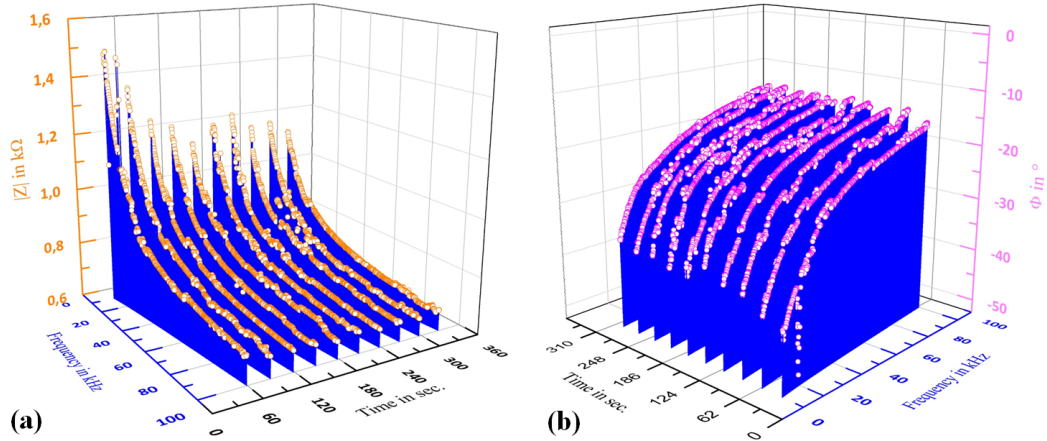


**Figure 7.5: DeCaDrive evaluation with 3D impedance spectrogram - Magnitude (a) and phase (b).**

Instead of using Cole-Cole plot a *3D impedance spectrogram* is introduced to facilitate impedance response analysis in both time and frequency domains. As depicted in Fig. 7.5 the magnitude and phase angle of measured complex impedance are visualized in 330-second time frame with 10 times of frequency sweep from 10 to 100 kHz. A time frame covering one frequency sweep with specified frequency range is referred as *evaluation window* for IS-sensor data.

Two learning algorithms, i.e., scaled conjugate gradient (SCG) algorithm [MM93] and Levenberg-Marquardt (LM) algorithm [Mor77], have been evaluated in DeCaDrive along with the ANN based classifier in the first implementation. The classification results were carried out by performing 10-fold cross-validation process. A comparison between two learning algorithms in terms of confusion matrix of classifier can be made in Table 7.1 and Table 7.2.

The classification accuracy (ACC) with dependencies on the number of hidden neurons and the learning algorithms are illustrated in Fig. 7.6. The classifier trained with LM algorithm yields superior outcome compared to the one with SCG algorithm.

## 7. EXPERIMENTAL WORK

---

**Table 7.1:** Confusion matrix of classification results based on scaled conjugate gradient algorithm (SCG)

SCG 40		Target Class (GT)			
		I	II	III	$\Sigma$
Output Class (PR)	I	339 7.1%	22 0.5%	10 0.2%	91.4% 8.6%
	II	147 3.1%	3226 67.7%	298 6.3%	87.9% 12.1%
	III	10 0.2%	101 2.1%	614 12.9%	84.7% 15.3%
	$\Sigma$	68.3% 31.7%	96.3% 3.7%	66.6% 33.4%	87.7% 12.3%

**Table 7.2:** Confusion matrix of classification results based on Levenberg-Marquardt algorithm (LM)

LM 80		Target Class (GT)			
		I	II	III	$\Sigma$
Output Class (PR)	I	494 10.4%	2 0.0%	0 0.0%	99.6% 0.4%
	II	2 0.0%	3338 70.0%	4 0.1%	99.8% 0.2%
	III	0 0.0%	9 0.2%	918 19.3%	99.0% 1.0%
	$\Sigma$	99.6% 0.4%	99.7% 0.3%	99.6% 0.4%	99.6% 0.4%

Note: GT and PR represent Ground Truth and Predicted Result respectively. Class I, II, III indicate driver drowsiness levels: not drowsy, a little drowsy, deep drowsy.  $\Sigma$  gives the aggregated results for specific rows, columns or for the overall statistics in the matrix. For instance, in Table 7.1, 7.1% in cell GT-I-PR-I (under 339) indicates the percentage of truly predicted Class I samples against the overall samples under classification; the true positive rate (TPR) of Class I is given in cell GT-I-PR- $\Sigma$  upper row, i.e., 68.3%, while the false negative rate (FNR) of Class I is 31.7% at lower row. And 91.4% in cell GT- $\Sigma$ -PR-I upper row denotes the positive predictive value (PPV) of Class I, while the lower row value 8.6% indicates the false discovery probability (FDP) of Class I on the other hand. The consolidated overall classification accuracy (ACC) is given in cell GT- $\Sigma$ -PR- $\Sigma$  upper row as 87.7%.

## 7.4 Data Evaluation and System Validation

With 40 hidden neurons the classifier based on LM algorithm achieved the ACC result of 99.6% with high performance and modest memory consumption in the experiments.

A preliminary subset with 8 features corresponding to Feature 6, 12, 13, 14, 36, 37, 39, 40 are selected from Feature 1–40 in Table 6.2 (without IS-sensor features) by applying sequential feature selection algorithm (SFS). In this case backward heuristic search is used to minimize the feature set while preserving the feature quality with respect to overlap and separability. The selected features are low steering percentage, head position in 3D coordinate system of Kinect sensor, mean eyebrow position, mean blink frequency, pulse rate LF/HF ratio and mean pulse rate.

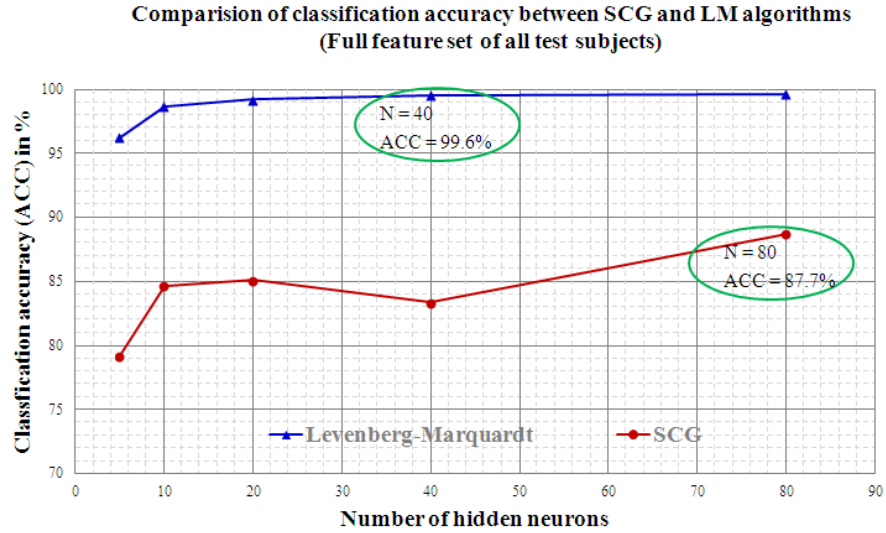


**Figure 7.6: Comparison of classification accuracy of algorithms** - Comparison between SCG and LM algorithms.

A comparison among different feature sets are summarized in Fig. 7.7, where *8 SFS* indicates 8 selected features being mentioned above; *only IS* indicates the exclusive IS-sensor features (Feature 41, 43, 45, 47, 49, 50, 51, 52, 56, 57, 58 in Table 6.2); while *without IS* means the total feature set excluding IS-sensor features, and *full* represents the complete feature set. The combined feature set *8 SFS & IS* yields the best result in the experiments. An overview of the feature sets used in the experiments is given in Table 7.3.

In the final version of DeCaDrive the flat SVM classification approach was employed and evaluated with 5 different feature sets: 8 SFS&IS, 8 SFS, w/o IS, IS, and full

## 7. EXPERIMENTAL WORK

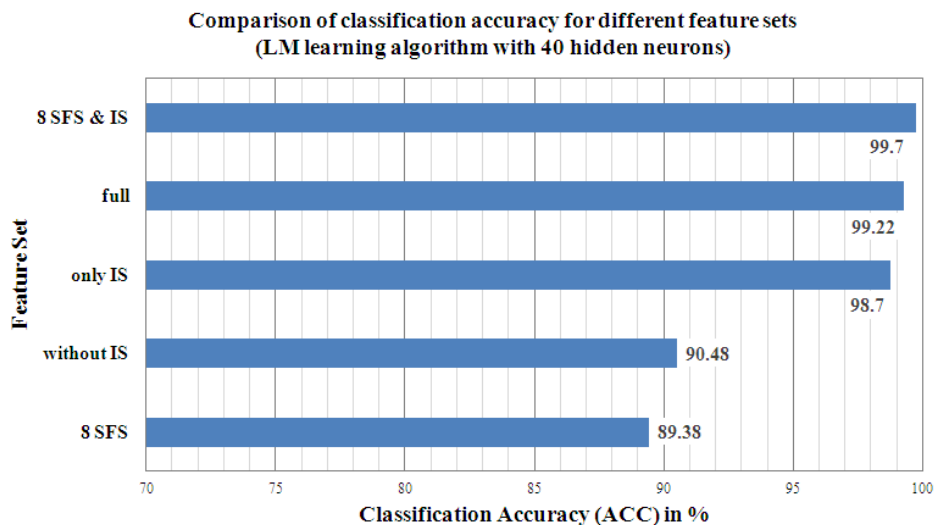


**Figure 7.7:** Comparison of classification accuracy of selected features - Drowsiness level classification accuracy (ACC) with dependency on selected features.

features. Afterwards, the *full* feature set as well as *8 SFS & IS* were applied in the H-SVM classification approach as described in Section 6.4.2. Each feature set was

**Table 7.3:** Overview of the feature sets used in the experiments

Sensor Feat.	Full	8SFS	IS	w/o IS	8SFS & IS	Description
Kinect	1-3	1-3	-	1-3	1-3	Head pos. in x,y and z
	4-6	-	-	4-6	-	Head orientation in x,y and z
	7,8	-	-	7-8	-	Translat. and rot. head velocity
	9	9	-	9	9	Eyebrow position
	10-11	10	-	10-11	10	Eyelid closing freq. and duration
Steering Angle	12-13	-	-	12-13	-	Steering activity
	14	-	-	14	-	Standard deviation of steering activity
	15	15	-	15	15	Percentage of minimum steering activity
	16	-	-	16	-	Mean of magnitude
	17	-	-	17	-	Steering speed
	18	-	-	18	-	Center of FFT-band
Pulse Sensor	18-19	18-19	-	18-19	18-19	HF/LF ratio of pulse frequency
IS	21-22	-	21-22	-	21-22	Mean and std. of magnitude
	23	-	23	-	23	Coeff. a (slope) of lin. fit (mag.)
	24	-	24	-	24	Coeff. a of exp. fit (mag.)
	25-27	-	25-27	-	25-27	Coeff. a, b and c of poly. fit (mag.)
	28	-	28	-	28	Coeff. a (slope) of lin. fit (pha.)
	29-31	-	29-31	-	29-31	Coeff. a, b and c of poly. fit (pha.)

## 7.4 Data Evaluation and System Validation

**Table 7.4:** Classification results

Feature Set	LM Algorithm in %	Flat SVM in %	H-SVM in %
8 SFS & IS (50%:50%)	99.70	99.79 (97.21)	99.58
8 SFS	89.38	78.28	-
w/o IS	90.48	93.19	-
IS	98.70	99.16	-
Full	99.22	98.22	99.66

**Table 7.5:** Flat SVM parameters generated from automated parameter search function

Parameter	Feature Set				
	8 SFS & IS (50%)	8 SFS	w/o IS	IS	Full
$C$	512 (32)	512	8	512	128
$\gamma$	8 (8)	8	8	8	2
No. of SVs	690 (674)	1124	1895	455	947

divided to training set and testing set by using the holdout random sampling method with 80% : 20% ratio for the flat SVM and more stringent 50%:50% ratio for the H-SVM as well as for a second reference run with flat SVM given in parentheses in Table 7.4. The parameter  $C$  and  $\gamma$  of all employed SVMs were optimized from the automated parameters search function with the searching range of 1 – 512 for  $C$  and 0 – 8.00 for  $\gamma$ . The obtained parameter values of flat SVM and H-SVM are summarized in Table. 7.5 and 7.6 respectively. The conducted experiments confirmed the superiority of the SVM in both flat and hierarchical approach.

To compare to the more lenient investigations of the previous work, first flat experiment was conducted with a larger training set. In the second, more extensive experiment, a substantially smaller training set was employed, which gives absolutely seen slightly smaller recognition rates of 99.66%, but the system solution will have much higher general validity and the promise to perform better for newly acquired "life" data. AFS application compacted the solution for a more lean system, but it has to be revisited, as the full set of features gives slightly better performances, than the selection adopted from the prior work with only 99.58%. The comparison between the feature map plot of the full feature data and the hierarchical data (global class-P vector) is visualized in Fig. 7.8.

## 7. EXPERIMENTAL WORK

---

**Table 7.6:** H-SVM parameters generated from automated parameter search function

Feature Set	Parameter	Sensor Channel				
		Kinect	Steering Angle	Pulse Rate	IS	Final
Full	$C$	128	32	512	512	512
	$\gamma$	8	8	2	8	8
	No. of SVs	700	1004	854	356	52
8 SFS & IS	$C$	64	128	512	512	512
	$\gamma$	6	8	2	8	8
	No. of SVs	560	848	854	356	50

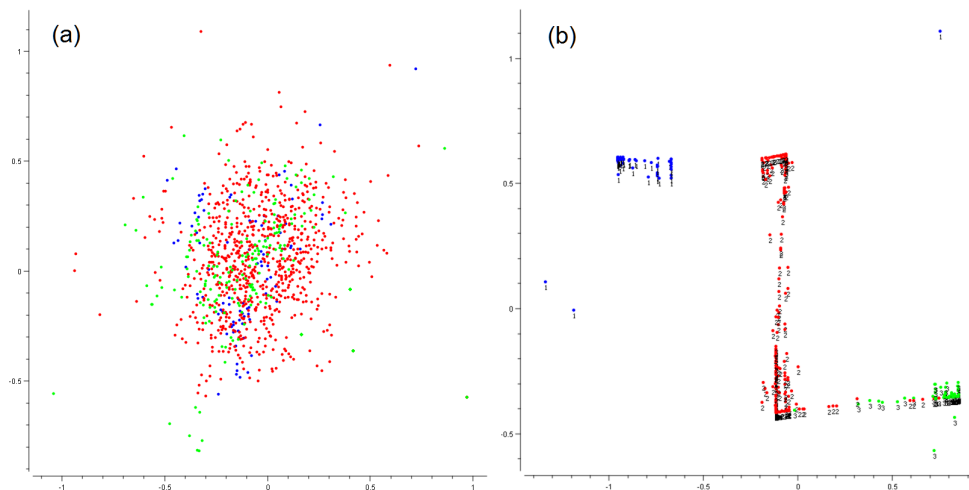


**Figure 7.8: Feature space** - (a) Flat SVM with full features; (b) the hierarchical data of the top-level SVM in H-SVM. It is clearly shown in (a) that the data possess a very high intrinsic dimensionality, which does not allow a mapping to 2D feature space with acceptable error.



## 7.5 Summary and Discussion

In this research work, the sequential feature selection algorithm is employed to refine the sensor feature set being used for classification. The feature selection can be further optimized with sophisticated heuristics, e.g., genetic algorithm (GA) and particle swarm optimization (PSO).

A more comprehensive sensitivity analysis on SVM parameters:  $C$  and  $\gamma$ , which impact the generation of optimum SVM model, is required, especially when the SVM training data changes in the sensor scope and data volume.

DeCaDrive is feeded with real-time sensor inputs including depth and color image sequences in video frame rate, steering angle, pulse rate, and skin impedance with much higher sampling rate. However, the Kinect frame rate is not constant, and varies in time due to the lighting condition and object tracking status. The sensitivities of different sensors are balanced through the alignment of sampling rates. In this case the sampling rate of the Kinect sensor is regarded as baseline for alignment.

Despite the response time, or say, the prediction time of DeCaDrive can fit the real-time requirements of ADAS, it is difficult to use the current system to detect microsleeps that can be as dangerous as the drowsy states. The visual clues of microsleeps such as slow eyelid-closure and head nodding [PIBW14] are not measured and evaluated in DeCaDrive, thus the current system should be further enhanced in this regard. In addition, microsleeps can hardly be identified through IS-sensor measures or pulse rate sensor features in the current system setup due to the lack of EEG measures for correlation studies.

Another issue is the ground truth definition of driver's drowsy states. The current approach is based on subjective ratings, either self-rating, or rating by independent observer/assessor. Thus, it requires human intervention, and may suffer from biased ratings or even rating failures. The EEG-based methods as discussed in Section 6.5 can be used along with other means to improve the accuracy of the ground truth definition of drowsy states.

## 7. EXPERIMENTAL WORK

---

## Chapter 8

# Conclusion and Future Work

### 8.1 Conclusion

Driving safety is one of the key requirements for the solutions of human mobility. Active safety related driver assistance systems have paved the way to mainstream automotive applications. To date, objectively and reliably detecting the fatigue/drowsiness of driver still remains as a challenge. Non-intrusive, accurate and robust driver drowsiness detection is one of the final goals of advanced driver assistance. DeCaDrive, a novel system approach to driver drowsiness detection based on emerging IR depth sensing and embedded impedance spectroscopy, multi-sensor data fusion and soft-computing algorithms, is presented in the thesis. Promising validation results up to 99.66% classification accuracy were achieved for driver drowsiness detection with on-line fresh acquired data. The DeCaDrive system was demonstrated on IAA Nutzfahrzeuge 2014 in Hannover.

One of the open issues in the DeCaDrive system modeling is the definition of ground truth of probands actual alertness or drowsiness, which still has been heuristically determined. In the future, EEG-based methods that are widely used in sleep research, can be adapted and utilized with endeavor to gain a better, somehow non-invasive, determination of the ground truth. Another issue is a potential person dependency in the classification system due to the limited number and phenotypes of the probands, which will be overcome by enlarging the database in the next steps. The robustness of DeCaDrive can be further examined and improved with more statistics and with data from real driving scenarios.

### 8.2 Contributions of the Thesis

One major contribution of the thesis is the investigation and exploitation of 3D embedded vision technologies, in particular depth cameras, in the field of human-vehicle interactions. Based on novel IR depth sensing and other promising sensor techniques (e.g. IS-sensor), as well as sensor data fusion approaches, a multi-sensor intelligent assistant system for driver status monitoring and intention prediction, is carried out. A new 3D impedance spectrogram is introduced to facilitate impedance response analysis in both time and frequency domains. Fusion of heterogeneous sensory sources aiming at more robust drowsiness detection has been explored. Powerful methods of computational intelligence, i.e., hierarchical SVMs for decision-making and automation capabilities have been employed for optimum parameter search as well as sensor feature determination. Finally, the system is transferred to a new open-access multi-platform environment enabling its cross-platform functionality.

Furthermore, a holistic design methodology for ADAS encompassing both driver- and vehicle-based approaches to driver assistance is discussed in the thesis as well. The proposed system concept and architecture are not only applicable for passenger cars, but in particular are useful for commercial vehicles, as well as for the use in monitoring of operators of heavy, dangerous, and/or expensive agricultural/industrial/aerospace machinery.

Despite the trend that future automotive electronics advances towards fully autonomous driving, systems such as DeCaDrive belong to the fundamental components of human-vehicle interactions in active safety context, thus can contribute to human centered smart and safe mobility.

### 8.3 Future Work

In addition to fatigue/drowsiness detection, the sensing capability of DeCaDrive can be enhanced with more comprehensive driver status detection in complex driving scenarios. For instance, inspired by study in [UCPZ13] driving impairment such as inebriation can be investigated by employing the enhanced capability of DeCaDrive in bioelectrical impedance analysis with tetrapolar electrode method. The correlation study of bioelectrical impedance and human emotional state can be carried out thereafter. A new generation of human-vehicle interface can be built upon DeCaDrive to stretch

out to new dimensions including 3D vision based gesture control, bioinformation based interactions, etc.

Some future development considerations of DeCaDrive has been addressed in Section 6.5 already with respect to possible transfer to industry/market. With regard to a SoC-based realization of DeCaDrive, it needs to be packaged in a miniature enclosure and must deliver maximum computation performance, while dissipating minimum heat in order to operate at the extreme temperatures (note:  $-40^{\circ}C$  to  $125^{\circ}C$  is the temperature range of automotive-grade IC devices). Integration and miniaturization of embedded sensors with wireless technology can facilitate the overall system design.

Seeing increasing demand on Automotive Safety Integrity Level (ASIL) of E/E systems in automobile, and inspired by a case study of airbag system, the presented DeCaDrive system can be extended to further increase the driver/occupant safety in terms of vehicle interior monitoring. In the environment of airbag and safety control units, the position of the occupants' head at the time of the impact is of particular interest, as well as tracking the orientation and position of the occupants' extremities and torsos. Based on this information, more intelligent decisions can be made to minimize the effects or severity of injuries for the occupants. A DeCaDrive based platform features driver/occupant state monitoring, thus, can enable the in-vehicle safety system to run more sophisticated algorithms, make smarter decisions, and perform safety measures in a better way.

## 8. CONCLUSION AND FUTURE WORK

---

# Bibliography

- [ABTT10] A. AMDITIS, M. BIMPAS, G. THOMAIDIS, M. TSOGAS, M. NETTO, S. MAMMAR, A. BEUTNER, N. MÖHLER, T. WIRTHGEN, S. ZIPSER, A. ETEMAD, M. DA LIO, AND R. CICILLONI. **A Situation-Adaptive Lane-Keeping Support System: Overview of the SAFELANE Approach.** *IEEE Transactions on Intelligent Transportation Systems.*, **11**(3):617–629, 2010. 14
- [AES91] AES. **Guidelines for Standard Electrode Position Nomenclature.** *J Clin Neurophysiol.*, 1991. 78
- [AGK03] D. ABRAHAMS AND R. W. GROSSE-KUNSTLEVE. **Building Hybrid Systems with Boost Python.** *C/C++ Users Journal*, **21**:29–36, 2003. 119
- [Ahl01] J. AHLBERG. **CANDIDE-3 – An Updated Parameterized Face.** Technical Report Report No. LiTH-ISY-R-2326, Dept. of Electrical Engineering, Linköping University, Sweden, 2001. 61
- [AM13] BELHASSEN AKROUT AND WALID MAHDI. *Multimedia and Ubiquitous Engineering*, chapter Vision Based Approach for Driver Drowsiness Detection Based on 3D Head Orientation, pages 43–50. Springer Netherlands, 2013. 61
- [ARTTS08] ARTTS. **ARTTS 3D-TOF Database**, [http://www.artts.eu/3d\\_tof\\_db.html](http://www.artts.eu/3d_tof_db.html), last visited: **05.10.2015**, 2008. 59
- [ASM11] A. ALBERS, E. SADOWSKI, AND L. MARXEN. *The Future of Design Methodology*, chapter 17 A New Perspective on Product Engineering Overcoming Sequential Process Models, pages 199–210. Springer Science & Business Media, 2011. 91
- [AUTOSAR] AUTOSAR. **AUTOSAR**, <http://www.autosar.org>, last visited: **01.12.2015**. 92, 93
- [AW92] E. ADELSON AND J. WANG. **Single Lens Stereo with Plenoptic Camera.** *IEEE Transactions on Pattern Analysis and Machine Intelligence*, **14**(2):99–106, February 1992. 25
- [BASELABS] BASELABS. **BASELABS**, <https://www.baselabs.de/sensor-data-fusion>, last visited: **20.12.2015**. 94
- [BBS11] B. BHOWMICK, S. BHADRA, AND A. SINHARAY. **Stereo Vision Based Pedestrians Detection and Distance Measurement for Automotive Application.** In *2nd International Conference on Intelligent Systems, Modelling and Simulation (ISMS)*, 2011. 20

## BIBLIOGRAPHY

---

- [BG10] BERNARD J. BAARS AND NICOLE M. GAGE. *Cognition, Brain, and Consciousness: Introduction to Cognitive Neuroscience*. Academic Press, 2010. 79, 80, 159
- [BJ88] P.J. BESL AND R.C. JAIN. **Segmentation Through Variable-Order Surface Fitting**. In *IEEE Trans. PAMI*, **10**, page 167, 1988. 59
- [BK08] GARY BRADSKI AND ADRIAN KAEHLER. *Learning OpenCV: Computer Vision with the OpenCV Library*, chapter 12 Projection and 3D Vision, pages 405–458. O’Reilly Media, 2008. 19, 20
- [BMBF3DKM] BMBF3DKM. **Micro-3D-camera project on BMBF website**, <http://www.photonikforschung.de/service/aktuellnachrichten/detailseite/archive/2012/08/03/article/neuartige-3d-kamera>, last visited: 20.08.2015. 34, 35
- [BNS06] L. M. BERGASA, J. NUEVO, M. Á. SOTELO, R. BAREA, AND M. E. L. GUILLÉN. **Real-Time System for Monitoring Driver Vigilance**. *IEEE Transactions on Intelligent Transportation Systems*, **7**(1):63–77, 2006. 13
- [BOSCH] BOSCH. **Bosch BMX055**, [https://www.bosch-sensortec.com/bst/products/all\\_products/bmx055](https://www.bosch-sensortec.com/bst/products/all_products/bmx055), last visited: 01.06.2016. 69
- [BPPW99] L. BIEL, O. PETERSSON, L. PHILIPSON, AND P. WIDE. **ECG Analysis: a New Approach in Human Identification**. In *Proceedings of the 16th IEEE Instrumentation and Measurement Technology Conference*, 1999. 85
- [BSH12] D. S. BOWMAN, W. A. SCHAUDT, AND R. J. HANOWSKI. *Handbook of Intelligent Vehicles*, chapter 34 - Advances in Drowsy Driver Assistance Systems Through Data Fusion, pages 895–912. Springer-Verlag London, 2012. 2, 3, 14
- [BT13] THOMAS BÖLKE. *Erweiterung eines multisensorischen Systems zur Fahrerzustands und absichtserkennung durch Impedanzspektroskopie*. Master’s thesis, ISE, TU Kaiserslautern, 2013. Betreuer: Dipl.-Ing. Li Li, Prof. Dr. Andreas König. 75
- [BTPR08] L.N. BOYLE, J. TIPPIN, A. PAUL, AND M. RIZZO. **Driver Performance in the Moments Surrounding a Microsleep**. *Transportation Research. Part F: Traffic Psychology and Behaviour*, **11**(2):126–136, 2008. 79
- [BVW91] K.A. BROOKHUIS, G. DE VRIES, AND D. DE WARD. **The Effects of Mobile Telephoning on Driving Performance**. *Accident Analysis and Prevention*, **23**(4):309–316, 1991. 71
- [Canesta] CANESTA. **Canesta DP200**, <http://www.roeder-johnson.com/RJDocs/CAAsdk0804.html>, last visited: 17.05.2015. 29, 66
- [CBH09] J.M. CLANTON, D.M. BEVLY, AND A.S. HODEL. **A Low-Cost Solution for an Integrated Multisensor Lane Departure Warning System**. *IEEE Transactions on Intelligent Transportation Systems*, **10**(1):47–59, 2009. 14
- [CCG04] M. CRAWFORD YANGCHI CHEN AND J. GHOSH. **Integrating Support Vector Machines in a Hierarchical Output Space Decomposition Framework**. In *Geoscience and Remote Sensing Symposium*, **2**, pages 949–952, 2004. 99



- [CFKE07] J. CLASSEN, J. FREY, B. KUHLMANN, AND P. ERNST. *Advanced Microsystems for Automotive Applications 2007*, chapter MEMS Gyroscopes for Automotive Applications, pages 291–306. Springer Berlin Heidelberg, 2007. 69
- [CKS98] D. CASPI, N. KIRYATI, AND J. SHAMIR. **Range Imaging with Adaptive Color Structured Light**. *IEEE Transactions on Pattern Analysis and Machine Intelligence*, **20**(5):470–480, 1998. 24
- [CS01] Koby CRAMMER AND YORAM SINGER. **On the Algorithmic Implementation of Multi-class Kernel-Based Vector Machines**. *Journal of Machine Learning Research*, pages 265–292, 2001. 99
- [CYTS10] ZHIMIN CAO, QI YIN, XIAOOU TANG, AND JIAN SUN. **Face Recognition with Learning-based Descriptor**. In *IEEE Conference on Computer Vision and Pattern Recognition*, 2010. 55
- [Daimler] DAIMLER. **Daimler AG**, <http://www.daimler.com>, last visited: **02.04.2015**. 2
- [DCEG13] J. DEMŠAR, T. CURK, A. ERJAVEC, Č. GORUP, T. HOČEVAR, M. MILUTINOVIČ, M. MOŽINA, M. POLAJNAR, M. TOPLAK, A. STARIČ, M. ŠTAJDOHAR, L. UMEK, L. ŽAGAR, J. ŽBONTAR, M. ŽITNIK, AND B. ZUPAN. **Orange: Data Mining Toolbox in Python**. *Journal of Machine Learning Research*, **14**:2349–2353, 2013. 106
- [DH06] A. V. DESAI AND M. A. HAQUE. **Vigilance Monitoring for Operator Safety: A Simulation Study on Highway Driving**. *Journal of Safety Research*, **37**:139–147, 2006. 13
- [DHUM11] YANCHAO DONG, ZHENCHENG HU, K. UCHIMURA, AND N. MURAYAMA. **Driver Inattention Monitoring System for Intelligent Vehicles: A Review**. *IEEE Transactions on Intelligent Transportation Systems*, **12**(2):596–614, 2011. 14
- [DM04] A. DELORME AND S. MAKEIG. **EEGLAB: an open source toolbox for analysis of single-trial EEG dynamics including independent component analysis**. *Journal of Neuroscience Methods*, **134**:9–21, 2004. 82
- [Drowsy14] DROWSYDRIVING.ORG. **Facts and Stats**, <http://drowsydriving.org/about/facts-and-stats>, last visited: **13.04.2014**. 2
- [Dus10] TOBIAS DÜSER. *X-in-the-Loop: ein durchgängiges Validierungsframework für die Fahrzeugentwicklung am Beispiel von Antriebsstrangfunktionen und Fahrassistenzsystemen*. Dissertation, Band 47. PhD thesis, Forschungsberichte des IPEK Institut für Produktentwicklung, Karlsruher Institut für Technologie (KIT), Karlsruhe, 2010. 91
- [EA05] C. EVERS AND K. AUERBACH. **Verhaltensbezogene Ursachen schwerer Lkw-Unfälle, BAST-Bericht M 174**. Technical report, 2005. 2
- [ECGPPG] ECGPPG. **ECG and PPG records**, <http://www.signalprocessingsociety.org/spcup2015>, last visited: **01.06.2016**. 84

## BIBLIOGRAPHY

---

- [EH98] ERIK HOLLNAGEL. *Co-operation in process management - Cognition and information technology*, chapter 4 - Context, Cognition, and Control, pages 27–52. London: Taylor & Francis, 1998. 9
- [EHFk09] M. ELSABROUTY, A. HAMDY, A. FAWKY, AND S. KHALIL. **Drowsy Driver Assistant System**. In *IEEE Int. Symposium on SPIT*, pages 176–180, 2007. 2
- [EJO05] J. ENGSTRÓM, E. JOHANSSON, AND J. ÓSTLUND. **Effects of Visual and Cognitive Load in Real and Simulated Motorway Driving**. *Transportation Research Part F*, 8:97–120, 2005. 71
- [Elk05] OMAR ELKHALILI. *Entwicklung von optischen 3D CMOS-Bildsensoren auf der Basis der Pulslaufzeitmessung*. PhD thesis, University of Duisburg-Essen, 2005. 30
- [EPOC] EPOC. **Emotiv EPOC**, <https://emotiv.com/store/epoc-detail/>, last visited: 02.10.2015. 81, 82
- [ESST01] ESST. **International Classification of Sleep Disorders Diagnostic and Coding Manual**, <http://www.esst.org/adds/ICSD.pdf>, page 343, 2001. 15
- [ETaster] ETASTER. **The E-Taster Assistance System with Lab-on-Spoon and Lab-on-Fork as "Electronic Tongues"**, [http://www.eit.uni-kl.de/koenig/gemeinsame\\_seiten/projects/E-Taster.html](http://www.eit.uni-kl.de/koenig/gemeinsame_seiten/projects/E-Taster.html), last visited: 10.09.2015. 87
- [EtasXiL] ETAS. **The XiL approach**, [http://www.etas.com/en/products/applications\\_virtualization\\_xil\\_approach.php](http://www.etas.com/en/products/applications_virtualization_xil_approach.php), last visited: 01.06.2016. 92
- [FaceTracking] FACETRACKING. **Face Tracking SDK in Kinect for Windows SDK**, <https://msdn.microsoft.com/en-us/library/jj130970.aspx>, last visited: 08.10.2015. 61, 113
- [FAT11] S. FOIX, G. ALENYA, AND C. TORRAS. **Lock-in Time-of-Flight (ToF) Cameras: A Survey**. *IEEE Sensors Journal*, 11:1–11, 2011. 30
- [FK89] R. FORCHHEIMER AND T. KRONANDER. **Image Coding - from Waveforms to Animation**. *IEEE Trans. on ASSP*, 37(12), 1989. 60
- [Ford] FORD. **Ford Motor Company**, <http://www.ford.com>, last visited: 02.04.2015. 2
- [Fotonic] FOTONIC. **Fotonic**, <http://www.fotonic.com>, last visited: 17.05.2015. 66
- [FZC09] R. FENG, G. ZHANG, AND B. CHENG. **An On-Board System for Detecting Driver Drowsiness Based on Multi-Sensor Data Fusion Using Dempster-Shafer Theory**. In *ICNSC*, pages 897–902, 2009. 14
- [GB94] J.W. GARDNER AND P.N. BARTLETT. **A Brief History of Electronic Noses**. *Sens. Actuat. B: Chem.*, 18:211–220, 1994. 85

- [GBB10] I. GARCIA, S. BRONTE, L. M. BERGASA, N. HERNANDEZ, B. DELGADO, AND M. SEVILLANO. **Vision-Based Drowsiness Detector for a Realistic Driving Simulator.** In *13th International IEEE Conference on Intelligent Transportation Systems (ITSC)*, pages 887–894, 2010. 13
- [Google] GOOGLE. **Google Driverless Car**, <https://www.google.com/selfdrivingcar/>, last visited: 10.04.2015. 1, 28
- [Gua12] ANDER GUARDE. **Kinect Based Eye Tracking for Driver Drowsiness Detection.** In: **Studienarbeit. Supervised by Dipl.-Ing. Li Li, Prof. Dr. Andreas Knig.** Technical report, Institute of Integrated Sensor Systems (ISE), TU Kaiserslautern, 2012. 113
- [GYB04] S. B. GOKTURK, H. YALCIN, AND C. BAMJI. **A Time-Of-Flight Depth Sensor System Description, Issues and Solutions.** In *IEEE Computer Society Conference on Computer Vision and Pattern Recognition Workshops (CVPRW04)*, page 35, 2004. 29, 30
- [Hay99a] SIMON HAYKIN. *Neural Networks - A Comprehensive Foundation*, chapter 5.11 Comparison of RBF Networks and Multilayer Perceptrons, pages 315–316. Pearson Education, 1999. 98
- [Hay99b] SIMON HAYKIN. *Neural Networks - A Comprehensive Foundation*, chapter 5.5 Regularization Theory, pages 289–299. Pearson Education, 1999. 98
- [HBMB07] M. HAKER, M. BÖHME, T. MARTINETZ, AND E. BARTH. **Geometric Invariants for Facial Feature Tracking with 3D TOF Cameras.** In *ISSCS*, pages 1–4, 2007. 59
- [HERZ05] MANFRED HERZ. **Optoelectronic Sensor and Device for 3D Distance Measurement**, April 2005. 32, 35
- [HMS69] E. C. HOFFER, C. K. MEADOR, AND D. C. SIMPSON. **Correlation of Whole-Body Impedance with Total Body Water Volume.** *Journal of Applied Physiology*, **27**(4):531–534, 1969. 74
- [HNL03] E. HOLLNAGEL, A. NÅBO, AND I.V. LAU. **A Systematic Model for Driver-in-Control.** In *The Second International Driving Symposium on Human Factors in Driver Assessment, Training and Vehicle Design. Park City Utah, July 21-24.*, 2003. 10
- [Hol98] ERIK HOLLNAGEL. *Co-operation in process management - Cognition and information technology*, chapter 4 - Context, Cognition, and Control, pages 27–52. London: Taylor & Francis, 1998. 9
- [Hol10] BARRY HOLLEMBEAK. *Today's Technician: Advanced Automotive Electronic Systems, Classroom Manual*, chapter 7 - Electronic Stability and Rollover Mitigation System, pages 225–228. Cengage Learning, 2010. 68
- [Hoo15] GREEN HILLS SOFTWARE PETER HOOGENBOOM. **Top 5 System Software Considerations for Next-Generation ADAS.** *EE Times Europe Automotive*, 5 2015. 92, 94
- [HS88] C. HARRIS AND M. STEPHENS. **A combined corner and edge detector.** In *Proc. 4th Alvey Vision Conference*, pages 147–151, 1988. 57

## BIBLIOGRAPHY

---

- [HW05] E. HOLLNAGEL AND D.D. WOODS. *Joint Cognitive Systems: Foundations of Cognitive Systems Engineering*. Boca Raton, FL: CRC Press / Taylor & Francis, 2005. 9, 10, 12, 159
- [HYHF09] PEI-YUNG HSIAO, CHUN-WEI YEH, SHIH-SHINH HUANG, AND LI-CHEN FU. **A Portable Vision-Based Real-Time Lane Departure Warning System: Day and Night**. *IEEE Transactions on Vehicular Technology*, **58**(4):2089–2094, 2009. 14
- [iC-Haus] IC HAUS. **iC-Haus GmbH**, <https://www.ichaus.de>, last visited: 17.05.2015. 66
- [IK11] K. ISWANDY AND A. KÖNIG. **Automated Design of Dependable Intelligent Sensory Systems with Self-x Properties**. In *In Proc. of the 15th Ann. Conf. on Knowledge-Based and Intelligent Information & Engineering Systems (KES 2011), Kaiserlautern, Sept. 12-14, Springer, LNAI 6881, Part. II, pp. 333-342*, 2011. 92
- [InvenSense] INVENSENSE. **InvenSense 9-Axis product**, <http://www.invensense.com/products/motion-tracking/9-axis>, last visited: 01.06.2016. 69
- [ISE3DKM] ISE3DKM. **3DKM project in the Institute of Integrated Sensor Systems (ISE)**, [http://www.eit.uni-kl.de/koenig/gemeinsame\\_seiten/projects/3DKM.html](http://www.eit.uni-kl.de/koenig/gemeinsame_seiten/projects/3DKM.html), last visited: 20.08.2015. 34
- [ISO26262] ISO26262. **ISO 26262 Road vehicles Functional safety at ISO Online Browsing Platform (OBP)**, <https://www.iso.org/obp/ui/>, last visited: 10.05.2015. 3, 15
- [Ivo03] A. IVORRA. **Bioimpedance Monitoring for physicians: an overview**. Technical report, Centre Nacional de Microelectrònica Biomedical Applications Group, 2003. 109
- [JLL06] Q. JI, P. LAN, AND C. LOONEY. **A Probabilistic Framework for Modeling and Real-Time Monitoring Human Fatigue**. *IEEE Trans. on Systems, Man and Cybernetics*, **36**(5):862–875, Sep. 2006. 99
- [JMHL00] T.P. JUNG, S. MAKEIG, C. HUMPHRIES, T.W. LEE, M.J. MCKEOWN, V. IRAGUI, AND T.J. SEJNOWSKI. **Removing Electroencephalographic Artifacts by Blind Source Separation**. *Psychophysiology*, **37**:163–78, 2000. 82
- [KinectV1] KINECTV1. **Microsoft Kinect V1**, <https://www.microsoft.com/en-us/kinectforwindows>, last visited: 02.04.2012. 53, 66
- [KinectV2] KINECTV2. **Microsoft Kinect V2**, <https://developer.microsoft.com/en-us/windows/kinect/hardware>, last visited: 16.04.2016. 66
- [Kot07] S. B. KOTSIANTIS. **Supervised Machine Learning: A Review of Classification Techniques**. *Informatika*, **31**:249–268, 2007. 97, 99
- [KSB13] A. KONDYLI, V. SISOPIKU, AND A. BARMPOUTIS. **A 3D Experimental Framework for Exploring Drivers' Body Activity Using Infrared Depth Sensors**. In *International Conference on Connected Vehicles and Expo (ICCVE)*, 2013. 56

- [KZ89] R. KORIES AND G. ZIMMERMANN. **Eine Familie von nichtlinearen Operatoren zur robusten Auswertung von Bildfolgen.** In *Ausgewählte Verfahren der Mustererkennung und Bildverarbeitung*, pages 96–119, 1989. 57
- [LabOnSpoon] LABONSPOON. **Lab-on-Spoon - Multi-Sensorial 3D-Integrated Measurement System for Smart-Kitchen and AAL Applications**, [http://www.eit.uni-kl.de/koenig/gemeinsame\\_seiten/projects/LabonSpoon.html](http://www.eit.uni-kl.de/koenig/gemeinsame_seiten/projects/LabonSpoon.html), last visited: 22.09.2013. 87
- [LBK13] LI LI, THOMAS BÖLKE, AND ANDREAS KÖNIG. **Can Impedance Spectroscopy Serve in an Embedded Multi-Sensor System to Improve Driver Drowsiness Detection?** In *Int. Workshop on Impedance Spectroscopy*, 2013. 15, 107, 110, 116
- [LHL08] MARTIN LIGGINS II, DAVID HALL, AND JAMES LLINAS. *Handbook of Multisensor Data Fusion: Theory and Practice, Second Edition*, chapter 1.6 Data Fusion Process Model, pages 8–9. CRC Press, 2008. 96
- [LLF94] H. LI, A. LUNDMARK, AND R. FORCHHEIMER. **Image Sequence Coding at Very Low Bitrates: A Review.** *IEEE Trans. on Image Processing*, **3**(5):589–609, 1994. 60
- [LRF93] H. LI, P. ROIVAINEN, AND R. FORCHHEIMER. **3-D Motion Estimation in Model-Based Facial Image Coding.** *IEEE Trans. on PAMI*, **15**(6):545–555, 1993. 60
- [LTK14] LI LI, K. THONGPULL, AND A. KÖNIG. **Optimizing the Design of a Multi-Sensor System for On-Line Driver State and Drowsiness Detection.** In *AHMT 2014 XXVIII. Messtechnisches Symposium des Arbeitskreises der Hochschullehrer fr Messtechnik*, 2014. 107, 108, 120
- [LWK12] LI LI, K. WERBER, C. F. CALVILLO, K. D. DINH, A. GUARDE, AND A. KÖNIG. **Multi-Sensor Soft-Computing System for Driver Drowsiness Detection.** In *The 17th Online World Conference on Soft Computing in Industrial Applications (WSC17)*, 2012. 56, 73, 104, 120, 126
- [LXK11] LI LI, YANHAO XU, AND ANDREAS KÖNIG. **Robust Depth Camera Based Eye Localization for Human-Machine Interactions.** In *15th International Conference on Knowledge-Based and Intelligent Information and Engineering Systems*, **6881**, page 424435, 2011. 56, 57, 58, 59, 60, 103
- [LXK12] LI LI, YANHAO XU, AND ANDREAS KÖNIG. **Robust Depth Camera Based Multi-User Eye Tracking for Autostereoscopic Displays.** In *9th International Conference on Sensors, Circuits & Instrumentation Systems (SCI)*, 2012. 18, 55, 56, 60, 103
- [Lytro] LYTRO. **Lytro Specifications: A Deeper Look Inside**, <http://lightfield-forum.com/2012/11/lytro-specifications-a-deeper-look-inside/>, last visited: 20.08.2015. 25
- [MCT06] J. MCCALL AND M. TRIVEDI. **Video-Based Lane Estimation and Tracking for Driver Assistance: Survey, System and Evaluation.** *IEEE Transactions on Intelligent Transportation Systems*, **7**(1):20–37, March 2006. 3, 14

## BIBLIOGRAPHY

---

- [Men88] Y. MENDELSON. **Noninvasive Pulse Oximetry Utilizing Skin Reflectance Photo-plethysmography**. *IEEE Transactions on Biomedical Engineering*, **35(10)**:798–805, 1988. 84
- [MESA] MESA. **MESA Imaging**, <http://www.mesa-imaging.ch>, last visited: 17.05.2015. 29, 66
- [MICRONAS] MICRONAS. **Micronas gas sensors**, <https://www.micronas.com/en/products/gas-sensors>, last visited: 01.06.2016. 86
- [MindWave] MINDWAVE. **NeuroSky MindWave**, <http://neurosky.com/biosensors/eeg-sensor/biosensors/>, last visited: 02.10.2015. 81
- [MM05] MICHAEL C. H. MCKUBRE AND DIGBY D. MACDONALD. *Impedance Spectroscopy, Theory Experiment and Applications (Second Edition)*, chapter 3 Measuring Techniques and Data Analysis. John Wiley & Sons, Inc., Hoboken, New Jersey, 2005. 74, 75, 76
- [MM93] MARTIN F. MØLLER. **A Scaled Conjugate Gradient Algorithm for Fast Supervised Learning**. *Neural Networks*, **6(4)**:525–533, 1993. 118, 129
- [MMRT01] K. MULLER, S. MIKA, G. RATSCH, K. TSUDA, AND B. SCHOLKOPF. **An Introduction to Kernel-Based Learning Algorithms**. *IEEE Transactions on Neural Networks*, **12**:181–201, 2001. 106
- [Mor77] JORGE J. MORÉ. **The Levenberg-Marquardt algorithm: Implementation and Theory**. In *Numerical Analysis*, 1977. 118, 129
- [MPEG4] MPEG4. **International Standard on Coding of Audio-Visual Objects, Part 2 (Visual), ISO-14496-2, 1999**. 61
- [Mur12a] KEVIN P. MURPHY. *Machine Learning: A probabilistic Perspective*, chapter 1.2 Supervised learning, page 3. The MIT Press, 2012. 97
- [Mur12b] KEVIN P. MURPHY. *Machine Learning: A probabilistic Perspective*, chapter 14.5 Support vector machines (SVMs), pages 498–499. The MIT Press, 2012. 99
- [MYBQ12] R. MOSS, P. YUAN, X. BAI, E. QUESADA, AND R. SUDHARSANAN. **Low-Cost Compact MEMS Scanning LADAR System for Robotic Applications**. In *Proceeding of SPIE*, **8379**, 2012. 26, 27
- [MZ00] Y. MATSUMOTO AND A. ZELINSKY. **An Algorithm for Real-Time Stereo Vision Implementation of Head Pose and Gaze Direction Measurement**. In *4th IEEE International Conference on Automatic Face and Gesture Recognition*, pages 499–504, 2000. 115
- [Nei76] ULRIC NEISSER. *Cognition and Reality: Principles and Implications of Cognitive Psychology*. New York: W.H. Freeman and Company, 1976. 9
- [NG05] R. NG, M. LEVOY, M. BREDIF, G. DUVAL, M. HOROWITZ, AND P. HANRAHAN. **Light Field Photography with a Hand-Held Plenoptic Camera**. Technical report, Stanford University Computer Science Tech Report CSTR 2005-02, April 2005. 25

- [NHTSA] NHTSA. **NHTSA Announces Final Rule Requiring Rear Visibility Technology, Press Releases**, <http://www.nhtsa.gov/About+NHTSA/Press+Releases/2014/NHTSA+Announces+Final+Rule+Requiring+Rear+Visibility+Technology>, last visited: 21.09.2014. 14
- [Nik14] ZORAN NIKOLIĆ. *Advances in Embedded Computer Vision*, chapter 3 - Embedded Vision in Advanced Driver Assistance Systems, pages 45–69. Springer International Publishing, 2014. 20, 21
- [NMEV94] A. NAJMI, A. MAHRANE, D. ESTEVE, AND G. VIALARET. **A Scanning Lidar System for Obstacle Avoidance in Automotive Field**. In *Proceedings of the Third IEEE Conference on Control Applications*, 1994. 26
- [Nyb70] J. NYBOER. *Electrical Impedance Plethysmography, 2nd edition*. Charles C. Thomas, 1970. 73
- [odos15] ODOS. **real.iZ VS-1000**, <http://www.odos-imaging.com/products/vs-1000/>, last visited: 17.05.2015. 29, 66
- [OpenKinect10] OPENKINECT. **OpenKinect**, <http://openkinect.org>, last visited: 09.06.2010. 55
- [OPTE05] J. ÖSTLUND, B. PETERS, B. THORSLUND, J. ENGSTRÖM, G. MARKKULA, A. KEINATH, D. HORST, S. JUCH, S. MATTES, AND U. FOEHL. **Driving Performance Assessment Methods and Metrics**. Technical report, AIDE - Adaptive Integrated Driver-vehicle InterfacE, IST-1-507674-IP, 2005. 10, 11
- [Optrima] OPRIMA. **Optrima**, <http://www.optrima.com>, last visited: 02.11.2012. 29, 66
- [OSST11] T. OGAWA, H. SAKAI, Y. SUZUKI, K. TAKAGI, AND K. MORIKAWA. **Pedestrian Detection and Tracking Using In-Vehicle Lidar for Automotive Application**. In *IEEE Intelligent Vehicles Symposium (IV)*, 2011. 27
- [Panasonic] PANASONIC. **D-IMager**, <http://www2.panasonic.biz/es/densetsu/device/3DImageSensor/en/>, last visited: 17.05.2015. 29, 66
- [PfalzMetall13] PFALZMETALL. **Zwei TU-Absolventen mit dem Preis der Stiftung PfalzMetall 2013 ausgezeichnet**. 120
- [PIBW14] G.R. POUDEL, C.R. INNES, P.J. BONES, R. WATTS, AND R.D. JONES. **Losing the Struggle to Stay Awake: Divergent Thalamic and Cortical Activity during Microsleeps**. *Human Brain Mapping*, **35**(1):257–269, 2014. 135
- [PMDnano15] PMDNANO. **PMD Technologies**, <http://www.pmdtec.com>, last visited: 17.05.2015. 29, 64, 66
- [PN12] C.D. PANTILIE AND S. NEDEVSCHI. **SORT-SGM: Subpixel Optimized Real-Time Semiglobal Matching for Intelligent Vehicles**. *IEEE Transactions on Vehicular Technology*, **61**(3):1032–1042, 2012. 20

## BIBLIOGRAPHY

---

- [PointGrey] POINTGREY. **Point Grey**, <http://www.ptgrey.com/bumblebee2-firewire-stereo-vision-camera-systems>, last visited: 17.05.2015. 66
- [PrimeSense] PRIMESENSE. **PrimeSense**, <http://www.primesense.com>, last visited: 02.04.2012. 53, 54
- [PS85] F. G. PEET AND T. S. SAHOTA. **Surface curvature as a measure of image texture**. *IEEE Transactions on Pattern Analysis and Machine Intelligence*, **PAMI-7**(6):734–738, 1985. 58
- [PW01] RAMON PALLÀS-ARENY AND JOHN G. WEBSTER. *Sensors and Signal Conditioning*, chapter 3.4 Wheatstone Bridge, pages 154–159. Wiley-Interscience, 2001. 76
- [Ryd87] M. RYDFALK. **CANDIDE, A Parameterized Face**. Technical Report Report No. LiTH-ISY-I-866, Dept. of Electrical Engineering, Linkping University, Sweden, 1987. 60
- [SB97] S. M. SMITH AND J. M. BRADY. **SUSAN—A New Approach to Low Level Image Processing**. In *International Journal of Computer Vision*, **23**, pages 45–78, 1997. 57
- [SBE98] E. SCHALLER, J.O. BOSSET, AND F. ESHER. **Electronic noses and their application to food**. *Lebensm.-Wiss. Ul.-Technol.*, **31**:305–316, 1998. 86
- [See97] W. VON SEELEN. **Elektronisches Auge OPEL, Multimodaler Sensor zur Fahrzeugführung: Teilprojekt: Architektur, Rundumsicht und Objekterkennung, Abschlußbericht zum 30. Juni 1997**. Technical report, Univ., Inst. für Neuroinformatik, 1997. 7
- [SFCS11] J. SHOTTON, A. FITZGIBBON, M. COOK, T. SHARP, M. FINOCCHIO, R. MOORE, A. KIPMAN, AND A. BLAKE. **Real-Time Human Pose Recognition in Parts from Single Depth Images**. In *CVPR, IEEE*, 2011. 60
- [SFSB08] F. SEOANE, J. FERREIRA, J. J. SANCHÉZ, AND R. BRAGÓS. **Analog Front-End Enables Electrical Impedance Spectroscopy System On-Chip for Biomedical Applications**. *Physiological Measurement*, **29**(6):267–278, 2008. 76, 77
- [SHLA14] N. SMOLYANSKIY, C. HUITEMA, L. LIANG, AND S.E. ANDERSON. **Real-Time 3D Face Tracking based on Active Appearance Model Constrained by Depth Data**. *Image and Vision Computing*, **32**(11):860869, 2014. 61
- [SHM00] RUDOLF SCHWARTE, GERD HÄUSLER, AND REINHARD W. MALZ. *Computer Vision and Applications*, chapter 7 - Three-Dimensional Imaging Techniques, pages 177–208. Elsevier Inc., 2000. 22
- [SICK] SICK. **SICK Laser Scanner**, <https://www.sick.com/de/en/product-portfolio/opto-electronic-protective-devices/safety-laser-scanners/c/g187225>, last visited: 20.05.2016. 27
- [SJBG03] A. SANTANA, B. JAMMES, S. BOVERIE, A. GIRALT, H. POULARD, AND J. THOMAS. **Driver Vigilance Monitoring - New Developments within the AWAKE Project**. In *IFAC Intelligent Components and Instruments for Control Applications*, 2003. 68



- [SJS08] N. SELVARAJ, A. JARYAL, J. SANTHOSH, K.K. DEEPAK, AND S. ANAND. **Assessment of Heart Rate Variability Derived from Finger-Tip Photoplethysmography as Compared to Electrocardiography.** *J Med Eng Technol.*, **32(6)**:479–84, 2008. 83
- [SP96] P. J. SHERMAN, M. ELLING, AND M. BREKKE. **The Potential of Steering Wheel Information to Detect Driver Drowsiness and Associated Lane Departure.** In: **Technical Report.** Technical report, Midwest Transportation Center, Iowa State University, 1996. 13, 73
- [SKSK99] J. SKRIBANOWITZ, T. KNOBLOCH, J. SCHREITER, AND A. KÖNIG. **VLSI Implementation of an Application-Specific Vision Chip for Overtake Monitoring, Real Time Eye Tracking, and Visual Inspection.** In *MicroNeuro 99*, pages 45–52, 1999. 7, 18
- [SRMC00] A. SAMMAN, L. RIMAI, J.R. MCBRIDE, R.O. CARTER, W.H. WEBER, C. GMACHL, F. CAPASSO, A.L. HUTCHINSON, D.L. SIVCO, AND A.Y. CHO. **Potential Use of Near, Mid and Far Infrared Laser Diodes in Automotive LIDAR Applications.** In *Vehicular Technology Conference, 2000. IEEE-VTS Fall VTC 2000*, 2000. 26
- [ST9D] STMICROELECTRONICS. **ST LSM9DS0**, <http://www.st.com/content/st.com/en/products/mems-and-sensors/inemo-inertial-modules/lsm9ds0.html>, last visited: **01.06.2016**. 69
- [StopSleep] STOPSLEEP. **StopSleep - Anti Sleep Alarm**, <http://www.stopsleep.de>, last visited: **02.05.2015**. 15
- [SY14] YE SUN AND XIONG BILL YU. **An Innovative Nonintrusive Driver Assistance System for Vital Signal Monitoring.** *IEEE Journal of Biomedical and Health Informatics*, **18(6)**:1932–1939, 2014. 13
- [TF05] Y. TAKEI AND Y. FURUKAWA. **Estimate of Driver’s Fatigue through Steering Motion.** In *IEEE International Conference on Systems, Man and Cybernetics*, **2**, pages 1765–1770, 2005. 13
- [Tho63] A. L. THOMASSET. **Bio-electric properties of tissues. Estimation by measurement of impedance of extracellular ionic strength and intracellular ionic strength in the clinic.** *Lyon Med.*, **209**:1325–1350, 1963. 73
- [TK14] K. THONGPULL AND A. KÖNIG. **Application-Specific partially Automated Design of Multi-Sensor Intelligent Lab-on-Spoon System.** In *AHMT 2014-XXVIII Messtechnisches Symposium des Arbeitskreises der Hochschullehrer für Messtechnik*, 2014. 119
- [tobiipro] TOBII. **Tobii Pro**, <http://www.tobiipro.com/product-listing/>, last visited: **15.10.2015**. 20
- [Tow01] NEIL TOWNSEND. **Pulse Oximetry.** *Medical Electronics*, pages 32–42, 2001. 84
- [Toyota] TOYOTA. **Toyota Motor Corporation**, <http://www.toyota.com>, last visited: **02.04.2015**. 2
- [TriDiCam] TRIDI CAM. **TriDiCam**, <http://www.tridicam.de/en.html>, last visited: **17.05.2015**. 29, 66

## BIBLIOGRAPHY

---

- [TVGS11] J. TAELEMAN, S. VANDEPUT, I. GLIGORLJEVIC, A. SPAEPEN, AND S. VAN HUFFEL. **Time-frequency Heart Rate Variability Characteristics of Young Adults during Physical, Mental and Combined Stress in Laboratory Environment.** In *Annual International Conference of the IEEE Engineering in Medicine and Biology Society*, 2011. 85
- [UCPZ13] M. ULBRICH, M. CZAPLIK, A. POHL, M. ZINK, AND S. LEONHARDT. **Estimation of Blood Alcohol Content with Bioimpedance Spectroscopy.** In *Int. Workshop on Impedance Spectroscopy*, 2013. 138
- [USTGAS] UST. **UST gas sensors**, <http://www.umweltsensortechnik.de/index3.htm>, last visited: **01.06.2016**. 86
- [vADASdeveloper] VECTOR. **Vector vADASdeveloper**, [http://vector.com/vi\\_vadasdeveloper\\_en.html](http://vector.com/vi_vadasdeveloper_en.html), last visited: **20.12.2015**. 94
- [Vap95] VLADIMIR NAUMOVICH VAPNIK. *The Nature of Statistical Learning Theory*. Springer, 1995. 98
- [VDPA12] CARMELO VELARDO, JEAN-LUC DUGELAY, MARCO PALEARI, AND PAOLO ARIANO. **Building the Space Scale or How to Weigh a Person with No Gravity.** In *IEEE 1st International Conference on Emerging Signal Processing Applications*, 2012. 63
- [Velodyne] VELODYNE. **Velodyne Lidar**, <http://velodynelidar.com/hdl-64e.html>, last visited: **20.05.2016**. 27, 28
- [Volvo] VOLVO. **Volvo Car Corporation**, <http://www.volvocars.com>, last visited: **02.04.2015**. 2
- [VW] VW. **Volkswagen AG**, <http://www.volkswagen.com>, last visited: **02.04.2015**. 2
- [WB09] ALPHUS D. WILSON AND MANUELA BAIETTO. **Applications and Advances in Electronic-Nose Technologies.** *Sensors*, **9**:5099–5148, 2009. 85, 86
- [Wer12] KLAUDIUS WERBER. *Untersuchung von Fahrerassistenzsystemen zur Fahrer- Zustands- und Absichtserkennung mit Multisensorik.* In: *Diplomarbeit*. Master's thesis, ISE, TU Kaiserslautern, 2012. Betreuer: Dipl.-Ing. Li Li, Prof. Dr. Andreas Knig. 105, 106, 115, 117, 120
- [WLAL11] M.-H. WANG, C.-S. LEE, G. ACAMPORA, AND V. LOIA. *ECG Signal Processing, Classification and Interpretation*, chapter 7 Electrocardiogram Application Based on Heart Rate Variability Ontology and Fuzzy Markup Language, pages 155–178. Springer, 2011. 83
- [WW99] J. WESTON AND C. WATKINS. **Support Vector Machines for Multiclass Pattern Recognition.** In *7th European Symposium on Artificial Neural Networks*, 1999. 99
- [YMT09] JI HYUN YANG, ZHI-HONG MAO, L. TIJERINA, T. PILUTTI, J. F. COUGHLIN, AND E. FERON. **Detection of Driver Fatigue Caused by Sleep Deprivation.** *IEEE Trans. on Systems, Man and Cybernetics*, **39**(4):694–705, July 2009. 99
- [Yu09] XUN YU. **Real-Time Nonintrusive Detection of Driver Drowsiness: Final Report.** Technical report, University of Minnesota, 2009. 13, 85

## BIBLIOGRAPHY

---

- [ZFK07] ZHENG LIU, D.S. FORSYTH, J.P. KOMOROWSKI, K. HANASAKI, AND T. KIRUBARAJAN. **Survey: State of the Art in NDE Data Fusion Techniques.** *IEEE Trans. on Instrumentation and Measurement*, **56**(6):2435–2451, 2007. 95, 96
- [ZVIEW] ZVIEW. **ZView for Windows**, <http://www.scribner.com>, last visited: 29.10.2015. 76
- [ZWB12] ZHEN ZHANG, YIFEI WANG, J. BRAND, AND N. DAHNOUN. **Real-Time Obstacle Detection Based on Stereo Vision for Automotive Applications.** In *5th European DSP Education and Research Conference*, 2012. 20

## BIBLIOGRAPHY

---

# List of Figures

2.1	COCOM . . . . .	9
2.2	ECOM . . . . .	10
2.3	ADAS in ECOM . . . . .	11
3.1	Stereo triangulation . . . . .	19
3.2	Stereo rectification . . . . .	20
3.3	ADAS stereo front view system . . . . .	21
3.4	Lightsheet triangulation . . . . .	22
3.5	Structured light . . . . .	23
3.6	Kinect . . . . .	24
3.7	Lytro light-field camera . . . . .	25
3.8	LIDAR imaging system . . . . .	27
3.9	Google self-driving car prototype with Velodyne HDL-64E LIDAR sensor	28
3.10	Commercial available ToF cameras and sensors . . . . .	29
3.11	Time-of-Flight: continuous wave modulation . . . . .	29
3.12	DriMix ToF pulse modulation . . . . .	32
3.13	DriMix system diagram . . . . .	33
3.14	DriMix control board (prototype) . . . . .	33
3.15	DriMix sensor components . . . . .	34
3.16	DriMix camera board . . . . .	34
3.17	DriMix Micro-3D-Camera and its application . . . . .	35
3.18	DriMix (drift-field-mixing) concept . . . . .	36
3.19	DriMix measurement (Case 1) . . . . .	38
3.20	DriMix measurement (multiple integration) . . . . .	40
3.21	DriMix measurement (Case 2) . . . . .	41

## LIST OF FIGURES

---

3.22	DriMix measurement (Case 3)	43
3.23	DriMix measurement (Case 4)	44
3.24	DriMix measurement (aliasing)	46
3.25	DriMix Evaluation (normalization)	47
3.26	DriMix Evaluation (distance calculation)	49
3.27	DriMix Evaluation (distance calculation with details)	50
3.28	DriMix measurement flow	51
3.29	DriMix host application	52
3.30	DriMix validation test	53
3.31	PrimeSensor	54
3.32	Kinect V1 sensor calibration	55
3.33	Eye localization (algorithm)	57
3.34	Eye template	58
3.35	Eye localization (feature map)	59
3.36	CANDIDE	61
4.1	Vehicle sensors to measure dynamic motions	68
4.2	General trend of steering angle	72
4.3	Bipolar and tetra-polar electrode methods	75
4.4	Impedance plane plot	75
4.5	Impedance plane 3D plot	76
4.6	Skin impedance measurement	77
4.7	Skin impedance response in time	77
4.8	The 10-20 system for EEG	78
4.9	Brain-computer interface	81
4.10	Emotiv TestBench	82
4.11	Pulox	83
4.12	ECG and PPG record comparison	84
5.1	Sensor signal processing pipeline mapped in COCOM	90
5.2	The proposed system concept	91
5.3	The XiL approach	92
5.4	AUTOSAR software architecture	93
5.5	ADAS on multicore system	94

---

## LIST OF FIGURES

5.6	Data fusion schemes . . . . .	96
5.7	Multilayer perceptrons and RBF . . . . .	98
5.8	SVM-based classification . . . . .	99
5.9	Holistic design of ADAS . . . . .	100
6.1	DeCaDrive system concept . . . . .	102
6.2	DeCaDrive (the first version) . . . . .	104
6.3	DeCaDrive (the first demo) . . . . .	105
6.4	DeCaDrive GUI of the first demo . . . . .	106
6.5	DeCaDrive with IS enhancement . . . . .	107
6.6	DeCaDrive (the final version) . . . . .	107
6.7	DeCaDrive host application GUI . . . . .	108
6.8	Embedded IS-sensor in DeCaDrive . . . . .	110
6.9	Kinect Face Tracking . . . . .	113
6.10	IS-sensor features . . . . .	116
6.11	DeCaDrive data flow . . . . .	117
6.12	Hierarchical classification in DeCaDrive . . . . .	120
7.1	DeCaDrive demonstrator . . . . .	125
7.2	Driving Simulator 2011 . . . . .	125
7.3	Ground truth and extracted features . . . . .	126
7.4	Alternative method for ground truth definition . . . . .	128
7.5	DeCaDrive evaluation with 3D impedance spectrogram . . . . .	129
7.6	Comparison of classification accuracy of algorithms . . . . .	131
7.7	Comparison of classification accuracy of selected features . . . . .	132
7.8	Feature space . . . . .	134

## LIST OF FIGURES

---



# List of Tables

1.1	Summary of ADAS systems featuring driver drowsiness detection . . . .	2
2.1	Summary of functional characteristics of different control types [HW05]	12
3.1	Depth measurement evaluation of a single DriMix sensor pixel . . . . .	51
3.2	Specifications of the State-of-the-Art Depth Cameras . . . . .	66
4.1	EEG signal frequencies and the associated functions [BG10] . . . . .	80
6.1	Summary of sensory components used in DeCaDrive . . . . .	112
6.2	List of features being computed from multiple sensor measurements . .	114
7.1	Confusion matrix of classification results based on scaled conjugate gradient algorithm (SCG) . . . . .	130
7.2	Confusion matrix of classification results based on Levenberg-Marquardt algorithm (LM) . . . . .	130
7.3	Overview of the feature sets used in the experiments . . . . .	132
7.4	Classification results . . . . .	133
7.5	Flat SVM parameters generated from automated parameter search function	133
7.6	H-SVM parameters generated from automated parameter search function	134

## LIST OF TABLES

---

# List of Symbols and Abbreviations

## Symbols

Symbol	Description
$\gamma$	Precision of RBF kernel, $\gamma = 1/(2\sigma^2)$
$\theta$	Steering angle
$\vartheta$	Threshold of steering-same-side angle
$\sigma$	Width of multivariate Gaussian function
$\mu_{k,T}$	The mean value of $\vec{D}_{k,T,orig}$
$\sigma_{k,T}$	The standard deviation of $\vec{D}_{k,T,orig}$
$\tau_d$	Time constant in RC circuit
$c$	Velocity of light
$C$	A regularization parameter of SVM
$C_g$	Geometrical capacitance in electrode system
$d$	Distance between photodetector and measuring object
$\mathcal{D}$	A labeled data set of input-output pairs
$\vec{D}_{k,T,norm}$	The normalized feature vector of test subject T of sensor feature k
$\vec{D}_{k,T,orig}$	The original feature vector
$f_{MOD}$	Frequency of modulation voltage (drift-voltage)
$G(x, x_i)$	Multivariate Gaussian function
$H$	Mean curvature for surface classification
$I(\omega)$	The measured frequency dependent current
$K$	Gaussian curvature for surface classification
$L$	A finite label set
$M$	A consolidated eye map
$M_{left}(x, y)$	A predefined left eye template
$M_{right}(x, y)$	A predefined right eye template

## LIST OF TABLES

---

Symbol	Description
$N$	Number of training examples
$R_b$	Bulk resistance in electrode system
$S(t)$	S-shaped sigmoid function
$T_{distance}$	Time-of-Flight for the pulsed laser traveling from light source to object
$T_{int.SA}$	Integration time of SA capacitor of DriMix sensor
$T_{int.SB}$	Integration time of SB capacitor of DriMix sensor
$T_{MOD}$	Period of modulation voltage (drift-voltage)
$T_{STARTADR}$	Time shift between emitted photocurrent and drift-voltage
$T_{travel}$	Time-of-Flight for the pulsed laser traveling from light source to photo detector
$T_{WIDTH}$	Pulse duration of emitted photocurrent (laser)
$U_{int.SA}$	Integrated voltage of SA capacitor of DriMix sensor
$U_{int.SB}$	Integrated voltage of SB capacitor of DriMix sensor
$U(\omega)$	The measured frequency dependent voltage
$x_i$	Data input of a classification system
$y_i$	Data output of a classification system
$Z_k$	Contact impedance of the joint current and voltage electrode on the measured skin surface
$Z_{TUS}$	Endogenous bioimpedance
$Z(\omega)$	The measured frequency dependent impedance

## Abbreviations

Abbreviation	Description
A-GPS	Assisted Global Positioning System
AAL	Ambient Assisted Living
AAM	Active Appearance Model
ABS	Anti-lock Braking System
ACC	(Classification) Accuracy
ACC	Adaptive Cruise Control
ADAS	Advanced Driver Assistance System
AFS	Automated Feature Selection
ANN	Artificial Neural Network
API	Application Programming Interface
ASIL	Automotive Safety Integrity Level
AUTOSAR	Automotive Open System Architecture
BAST	Federal Highway Research Institute
BCI	Brain-Computer Interface
BCM	Body Control Module
BMBF	German Federal Ministry of Education and Research
BN	Bayesian Networks
CAN	Controller Area Network
CCFET	Capacitive Coupled Field Effect Transistor
CDA	Canonical Discriminate Analysis
COCOM	Contextual Control Model
DeCaDrive	Depth-Camera-based Driver status monitoring
DGPS	Differential Global Positioning System
E/E System	Electric/Electronic System
ECG	Electrocardiography
ECOM	Extended Control Model
EDA	Electrodermal Activity
EEG	Electroencephalogram
EIS	Electrochemical Impedance Spectroscopy
EPS	Electric Power Steering
ESP	Electronic Stability Program
FDP	False Discovery Probability
FNR	False Negative Rate
FOV	Field Of View

## LIST OF TABLES

---

Abbreviation	Description
GA	Genetic Algorithm
GPS	Global Positioning System
GUI	Graphic User Interface
HBR	Heart Beat Rate
HiL	Hardware-in-the-Loop
HRV	Heart Rate Variability
HSVM	Hierarchical Support Vector Machine
HUD	Head-Up Display
IR	Infrared
IS	Impedance Spectroscopy
ISE	Institute of Integrated Sensor System at TU Kaiserslautern
ID	Intensity and Depth Image Output
ICA	Independent Component Analysis
IVIS	In-Vehicle Infotainment System
LDW	Lane Departure Warning
LIDAR	Laser Illuminated Detection and Ranging
LM	Levenberg-Marquardt algorithm
MDA	Multivariate Data Analyzes
MiL	Model-in-the-Loop
MLP	Multilayered Perceptrons
MEMS	Micro-Electro-Mechanical Systems
MSE	Mean Square Error
NHTSA	National Highway Traffic Safety Administration
NIR	Near Infrared
NUI	Natural User Interface
OTM	Overtake-Monitors
PCA	Principal Component Analysis
PERCLOS	Percent Eye Closure
PPG	Photoplethysmography
PPV	Positive Predictive Value
PSO	Particle Swarm Optimization
RBF	Radial Basis Function
REM	Rapid Eye Movement
RGBD	Color and Depth Image Output
ROI	Region of Interest
RTOS	Real-Time Operating System

---

## LIST OF TABLES

---

Abbreviation	Description
SAW	Surface Acoustic Wave
SCG	Scaled Conjugate Gradient algorithm
SENT	Single Edge Nibble Transmission
SFS	Sequential Feature Selection
SiL	Software-in-the-Loop
SPI	Serial Peripheral Interface
$SpO_2$	Blood Oxygen Saturation
SVM	Support Vector Machine
ToF	Time-of-Flight
TPMS	Tire Pressure Monitoring System
TPR	True Positive Rate
TUS	Tissue Under Study
UGV	Unmanned Ground Vehicle
UUT	Unit Under Test
V2X	Vehicle-to-Vehicle, Vehicle-to-Infrastructure Communications
VioLET	Video-based Lane Estimation and Tracking
XiL	X-in-the-Loop

---

## LIST OF TABLES

---



# Appendix

## Hardware Specifications

This section provides complementary information about specifications of system components.

- AD5933 Data Sheet: 1 MSPS, 12-Bit Impedance Converter, Network Analyzer  
Website: <http://www.analog.com/media/en/technical-documentation/data-sheets/AD5933.pdf>
- Arduino Mega 2560 microcontroller (ATmega2560) Data Sheet  
Website: <https://www.arduino.cc/en/Main/arduinoBoardMega2560>
- Depth Sensor Database\*
- DriMix Sensor TS006 Specification A0.6\*\*
- Kinect for Windows Sensor Components and Specifications  
Website: <https://developer.microsoft.com/en-us/windows/kinect/hardware>

Note\*: The information with regard to the depth sensor database could be potentially obtained from Institute of Integrated Sensor Systems (ISE) based on individual negotiations.

Note\*\*: Please contact iC-Haus GmbH for more details about the DriMix sensor.

## Source Code

The software components used in the research work that are available in public resource are summarized here.

## LIST OF TABLES

---

- Kinect for Windows software development kit (SDK v2.0).  
Website: <https://www.microsoft.com/en-us/download/details.aspx?id=44561>
- Orange - Data Mining Toolbox in Python.  
Website: <http://orange.biolab.si>

All C/C++/MATLAB/Python/Orange source code and libraries related to the development and evaluation of the DriMix sensor as well as the DeCaDrive system are proprietary information, hence can only be accessible in a research partnership with Institute of Integrated Sensor Systems (ISE), TU Kaiserslautern.

## Test Reports

The test reports for the validation of the DriMix camera system are generated in the 3DKM project at Institute of Integrated Sensor Systems (ISE), TU Kaiserslautern. The information with regard to the test reports could be potentially obtained from ISE based on individual negotiations.

# Lebenslauf

## Persönliche Daten

Name, Vorname:	Li, Li
Geburtsort:	Hubei, VR China
Nationalität:	chinesisch
Familienstand:	verheiratet

## Berufliche Erfahrung

05.2012 - heute	Entwicklungsingenieur bei Renesas Electronics Europe GmbH
02.2009 - 04.2012	Wissenschaftlicher Mitarbeiter (Doktorand) Lehrstuhl Integrierte Sensorsysteme, TU Kaiserslautern

## Studium und Ausbildung

04.2006 - 11.2008	TU Kaiserslautern, Rheinland-Pfalz, Deutschland Dipl.-Ing. in Informationstechnik mit Vertiefungsrichtung Digitaltechnik Diplomarbeit "Entwicklung eines Kommunikationsmoduls für elektronische Komponenten auf Basis eines FPGA's"
04.2004 - 03.2006	TU Kaiserslautern, Rheinland-Pfalz, Deutschland Vordiplom in Informationstechnik
09.2001 - 03.2004	Tongji Universität, Shanghai, VR China DSH (Deutsche Sprachprüfung für den Hochschulzugang) qualifiziert
09.1998 - 08.2001	Yiling-Mittelschule der Stadt Yichang der Provinz Hubei
09.1995 - 08.1998	Untere Yunchi-Mittelschule des Bezirks Xiaoting der Stadt Yichang